ABSTRACT

Title of Document: NANOGAP JUNCTIONS AND CARBON NANOTUBE NETWORKS FOR CHEMICAL SENSING AND MOLECULAR ELECTRONICS

Gokhan Esen, Doctor of Philosophy, 2006

Directed By: Associate Professor, Michael S. Fuhrer, Department of Physics

This thesis work may be divided into two parts. The first part (chapters 2-7) focuses on the fabrication of a particular test structure, the electromigration (EM) formed metal nanogap junction, for studying the conduction through single molecules and for hydrogen sensing. The second part (chapters 8 and 9) focuses on carbon nanotube networks as electronic devices for chemical sensing.

Chapters 2-4 discuss the formation of nanogap junctions in thin gold lines fabricated via feedback controlled electromigration. Using a feedback algorithm and experimenting on thin gold lines of different cross sections, I show that the feedback controls nanogap formation via controlling the temperature of the junction. Chapters 5 and 6 discuss the background and my experimental efforts towards fabricating superconducting electrodes for single molecule electronics research.

Chapter 7 discusses the application of the techniques of chapters 2-4 to form palladium nanogaps via electromigration. I show that such devices can be used as

hydrogen sensors, but suffer from slow response times (on the order of minutes). The results are discussed in the context of the in-plane stress buildup between the palladium metallization and the SiO_2 substrate.

The use of nanotube networks as chemical sensors is discussed in the second part of the thesis (chapters 8 and 9). I show measurements of the resistance and frequency-dependent (50 Hz - 20 KHz) gate capacitance of carbon nanotube thin film transistors (CNT-TFTs) as a function of DC gate bias in ultra-high vacuum as well as low-pressure gaseous environments of water, acetone, and argon. The results are analyzed by modeling the CNT-TFT as an RC transmission line. I show that changes in the measured capacitance as a function of gate bias and analyte pressure are consistent with changes in the capacitive part of the transmission line impedance due to changes in the CNT film resistivity alone, and that the electrostatic gate capacitance of the CNT film does not depend on gate voltage or chemical analyte adsorption to within the resolution of my measurements. However, the resistance of the CNT-TFT is enormously sensitive to small partial pressure ($< 10^{-6}$ Torr) of analytes, and the gate voltage dependence of the resistance changes upon analyte adsorption show analyte-dependent signatures.

NANOGAP JUNCTIONS AND CARBON NANOTUBE NETWORKS FOR CHEMICAL SENSING AND MOLECULAR ELECTRONICS

By

Gokhan Esen

Dissertation submitted to the Faculty of the Graduate School of the
University of Maryland, College Park, in partial fulfillment
of the requirements for the degree of
Doctor of Philosophy
2006

Advisory Committee:
Associate Professor Michael S. Fuhrer, Chair
Professor Ellen D. Williams
Assistant Professor Min Ouyang
Assistant Professor John Cumings
Professor Neil Goldsman

Acknowledgements

I would like to thank all the friends for helping me to complete this important milestone in my life. I especially would like to thank my PhD advisor, Professor Michael S. Fuhrer, for helping me to finish my study his lab both with his ideas and his friendship. If I was starting my PhD today, I would still join his group. In numerous times during my study when we talked about science and physics, I felt the curiosity and excitement he had for it. I will always remember him and his wife, Cynthia, as being nice and friendly people.

I would also like to thank the other members of my dissertation committee, namely Professor Ellen D. Williams, Min Ouyang, John Cumings and Neil Goldsman for honoring me by serving in my committee.

Through the time I spent in Michael's lab, I had the chance to meet and work with several students and postdoctoral associates: Todd H. Brintlinger, Tobias Dürkop, Yung-Fu Chen, Enrique Cobas, Adrian Southard, David Tobias, Daniel Lenski, Tareq Ghanem, SungJae Cho, Chaun Jang, Shudong Xiao, Alexander Manasson, Anthony Ayari, Byong M. Kim and Stephanie A. Getty. I want to thank them since they were able to put up with me in the lab. I would especially like to thank Stephanie for being a kind mentor. I learned a lot of laboratory skills from Todd, Tobias, Yung-Fu and Anthony as well. I would like to thank them for helping me in numerous issues. I wish success for the rest of the Fuhrer Group that are working on their dissertation, I am sure they will graduate with lots of experience and skills. I also would like to thank Masahiro Ishigami and Elba Gomar-Nadal. They

were good friends and talented scientists. I also would like to thank all the staff working in the department.

I made so many good friends in Maryland. I would like to thank all of them for helping me to deal with the problems and sharing happy moment with me. Among them, I especially want to thank Nazif Cihan Taş and Murat Ömür. During the time I spend in United States, they were like two brothers to me and I hope they will be in the rest of my life. Lastly, I would like to thank my family. Their constant support in my life helped me to deal with difficulties I faced and the ones that I faced during PhD was not an exception.

Table of Contents

List of Tables

List of Figures

Chapter 1: Introduction

Since the invention of the transistor [1], the miniaturization trend in semiconductor industry has provided us with faster and cheaper computers. But the present trend of miniaturization which is based on the scaling of the complementary metal-oxide-semiconductor (CMOS) process in silicon is close to its limits due to both the technical difficulties such as ultra-thin gate oxides, doping fluctuations, short channel effects and the cost of production [2]. Therefore the next step in miniaturization will require conceptually new device structures.

The idea that a single molecule can be used as an active electronic component was first introduced by Aviram and Ratner [3] and spurred research activity over the last couple decades. However, the fabrication of complete circuits out of molecules still remains challenging (if possible at all) and it will come only after a solid understanding of the conduction properties of individual molecules that can perform the basic functions such as rectification, amplification and storage.

Chapters 2-7 of this thesis will focus on the fabrication of a particular test structure, the electromigration (EM) formed metal nanogap junction, for studying the conduction through single molecules and for hydrogen sensing. Chapter 2 will give a general review of electromigration and points out several metallurgical factors that affects the type and rate of electromigration.

The EM-formed metal nanogap junction is one of a large number of test structures for single-molecule electronics currently under study, and Chapter 3 will discuss some of the various competing techniques and the advantages and disadvantages of the EM-formed nanogap junction for molecular electronics study.

Briefly, the major advantages of the EM-formed nanogap junction are the relative ease of fabrication and its thermal stability, allowing low-temperature measurements of metal-molecule-metal junctions. Chapter 3 will also review electron transport through a mesoscopic sample and previous efforts in this research area that are related to our experimental results.

Chapter 4 will discuss the experiments I did to understand the formation of nanogaps in thin gold lines via electromigration. The control of the final junction resistance through a feedback scheme is demonstrated. By studying feedback-controlled EM in wires of various dimensions, it is found that the feedback scheme operates via temperature control of the electromigrating junction.

Chapters 5 and 6 describe my experimental efforts and the difficulties I faced in attempting to fabricate superconducting contacts for measurement of superconductor-molecule-superconductor junctions.

In chapter 7, I describe our efforts for making a novel hydrogen sensor using EM-formed nanogaps formed in palladium nanowires. Palladium, having high hydrogen solubility, is used as transducer element for various hydrogen sensors and filters. I attempted, with mixed success, to fabricate nanogap junctions in palladium nanowires using electromigration and to use these nanogaps as hydrogen sensors by utilizing the hydrogen induced lattice expansion mechanism of palladium.

The last part of the thesis, chapters 8-9, describes experiments to determine the nature of chemical sensitivity in carbon nanotube thin-film transistors (TFTs). Chapter 8 will give a brief introduction to carbon nanotubes and nanotube thin-film transistors.

Chapter 9 describes the experiments I did to understand the working mechanism of carbon nanotube TFTs as chemicapacitative sensors. I carried out several experiments to understand the resistive and capacitive response of carbon nanotube TFTs in ultra high vacuum, ambient atmosphere and in the presence of several analytes. I discuss our results by modeling the nanotube network as a simple resistor-capacitor (RC) transmission line, and find that, within the errors of our experiment, the measured changes in capacitance may be explained by changes in RC-transmission-line impedance induced by changes in the sheet resistance of the nanotube film.

Chapter 2: Electromigration

2.1: Introduction

When a thin metal film is subject to high current densities over a period of time, impurity ions and/or atoms of the metal may move diffusively along or in opposite direction to the electron flow. This current induced diffusion is called electromigration.

In industry, electromigration is a menace and can be defined as the principle metallization wear out failure mode in integrated circuit interconnects [4]. Because of the small device sizes in integrated circuits, even a few milliamps of current would be enough to produce current densities that will cause considerable electromigration damage. As long as the interconnects are wide enough and/or electromigration activity is lessened by using capping layers such as TiN electromigration is not a vital problem, that is, electromigration does not significantly degrade the reliability of a device in a short period of time. But since scaling down of integrated circuits requires scaling down of interconnects as well, electromigration stands as a serious future problem for industry.

In scientific research, failure of a narrow metal wire due to electromigration has also been utilized extensively to prepare stable electrical contact pairs with nanometer separation after the technique was shown to be a practical test bed [5-7] for single molecule electrical experiments. These experiments rely on producing nanogaps that are a few nanometers across by using electromigration as an electromechanical etching process. Later these nanogaps can be used as electrode

pairs for single molecules which are either adsorbed on the surface before the electromigration is performed or after the electromigration process.

Electromigration takes place when the high current density produces a pressure on the conductor atoms forcing them to move. Metal thin films contain large number of facile grain boundary and interfacial diffusion pathways that allow significant mass transport at relatively low temperatures. When there is a net divergence or convergence of mass flux, two failure modes of electromigration are observed. The first is failure due to formation of a void which causes an open circuit failure; and the other is failure due to formation of a hillock, production of excess material, which may form a bridge to an adjacent track in integrated circuits and cause a short circuit. In less severe cases where there is no failure but considerable diffusion activity, an increase in the interconnect resistance can be observed.

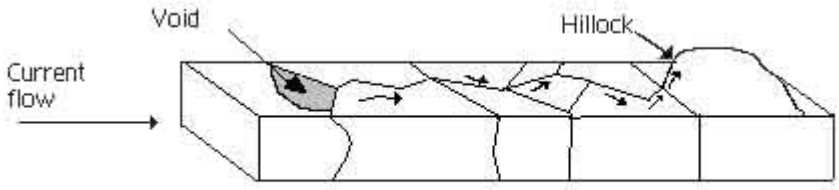

Figure 2-1. Void and hillock formation in a polycrystalline metal film. Adapted from reference [33]

In polycrystalline metallic interconnects; diffusion of atoms in the bulk, grain boundary diffusion, and diffusion of atoms at the surface are believed to be the

dominant physical mechanisms of electromigration. But how they cause electromigration in different metals and how important they are in different stages of electromigration is not well understood. Thus a clear understanding of the processes that play role at different stages of electromigration and their relative importance on one another is technologically very important.

Electromigration by its nature is a destructive phenomenon. Although it is possible to examine structures after the damage happens with scanning electron microscopy and/or transmission electron microscopy, with these techniques it is very hard to obtain information about the causes of the failure mechanisms. A good understanding of primary causes requires reasonable amount of data to be collected in the early stages of the process and/or while the failure due to electromigration occurs.

2.2: Microscopic Theories and Empirical Relations

Although electromigration can be stated simply as the migration of atoms in a preferred direction when current flows through a conductor, physical mechanisms that cause electromigration contain subtle issues such as the transport of electrons in the vicinity of a diffusing atom and how this transport produces a driving force that causes electromigration.

It is accepted that this force is in part due to the effect of bulk electric field inside the material on the bare valence of the migration ion (direct force) and in part due to momentum transfer of scattering of conduction electrons (wind force), but there is not a general agreement about their relative contribution to the net force. The difficulty arises because there is no clear understanding of the basic issues: how the

electric field is screened in the vicinity of migrating ion, what is the nature of inhomogeneities of current flow and electric field in the vicinity of migrating ion, and how they affect the migration process.

There are many theoretical models as well as empirical relations developed to explain observed electromigration failure. Below I explain some of the mainstream theoretical work in order to give the reader a general view of the subject and the solid state physics behind the electromigration phenomena so far.

2.2.1: Microscopic Theories

As stated above, the force causing the electromigration process can be divided into two components as shown in Equation 2-1.

$$\vec{F} = Ze\vec{E} + \vec{F}_{wind} = Z^{*}e\vec{E} \qquad \text{Equation 2-1}$$

Where Z is the bare valence of the migrating ion with respect to host lattice, $-e$ is the charge of the electron, $\vec{E}$ is the macroscopic electric field, and Z^{*} is the effective valence of the migrating ion and contains both the effect of bulk electric field on the ion and the dynamic coupling of the electrons. The primary goal in electromigration theory is to calculate the wind force and Z^{*}.

2.2.1.1: Ballistic Model

The first model trying to explain the wind force and deviation of Z^{*} from the bare valance, Z, was published by Fiks [8] and Huntington and Grone [9]

independently. In this model the origin of the wind force contribution to the total force was taken as the momentum transfer of scattering electrons from the migrating impurity ion. This force can be evaluated in the free electron model by using a shifted Fermi-Dirac distribution for describing how incoming and outgoing electronic states are distributed in $\vec{k}$ space and by using a generalized golden rule to evaluate transition probability per unit time. As a result of the calculation one can arrive at the final result that describes the wind force as

$$\vec{F}_{wind} = \frac{n\rho_i}{n_i \rho}(-e)\vec{E} \qquad \text{Equation 2-2}$$

where n and n_i are electron and impurity densities respectively, ρ is the total resistivity and ρ_i is the contribution of migrating impurities to the total resistivity. From the above formula, the wind force is proportional to, and in the opposite direction of, the electric field and, due to inverse proportionality with the total resistivity, it is expected to increase with decreasing temperature.

In this model Z^* can be written as $Z^* = Z - nl\sigma$ where *l* is the mean free path for electrons and includes all scattering effects, Z is the bare valence and σ is the cross section for scattering of electrons from the impurity.

Within different materials the number of electrons contained in the cylindrical volume $l\sigma$ might be larger or smaller than Z, and thus plays a dominant role in determining the relative importance of the direct force and wind force contributions. In simple metals where the free electron approximation is reasonable to use, the latter

contribution is dominant and the wind force is expected to be the more important factor.

Although the model is satisfactory in simple metals, a number of difficulties are involved in its generalization. In the Bloch theory of metals it is not an easy task to write a closed expression that describes momentum transfer per unit time. In addition it is not clear how momentum transfer is partitioned in more complicated scattering mechanisms that involve not only one ion but clusters of ions, and it is not understood what role the lattice plays in absorbing the momentum. There is also no discussion of the effect of screening on direct force.

2.2.1.2: Polarization Charge Models

An alternative model for calculating wind force was developed by Bosvieux and Friedel [10]. In their approach the effect of the scattering was to produce an inhomogeneity in the current flow. This inhomogeneity can be considered as a local charge polarization which gives rise to an electric field and it is this local field that produces the wind force. Since in a stationary situation the force exerted by the lattice defect on the electrons for maintaining this inhomogeneity is equal to the force exerted on the defect by the polarized charge distribution, calculation of the former force circumvents the conceptual difficulties encountered in the generalization of ballistic model. Within this approach the expression for wind force can be written as

$$\vec{F}_{wind} = -\int n(\vec{r}) \frac{\partial V_0}{\partial \vec{R}} d^3\vec{r} \qquad \text{Equation 2-3}$$

Here the electron density, $n(\vec{r})$, depends on both applied electric field and electric field produced by current induced polarization , V_0 is the interaction potential energy between the bare ion and electrons, $\vec{R}$ is the position of the impurity ion and the integration is over all space. Although this description of the wind force is exact, its calculation requires knowledge of the electron density, within the independent particle approximation we may write

$$n(\vec{r}) = \sum_{\vec{k}} f_{\vec{k}} \left|\Psi_{\vec{k}}(\vec{r})\right|^2 \qquad \text{Equation 2-4}$$

Where $f_{\vec{k}}$ is the shifted Fermi-Dirac distribution, $\Psi_{\vec{k}}$'s are scattering state wavefunctions and the sum is over all electronic states. $\Psi_{\vec{k}}(\vec{r})$ depends on both V_0 and the electrostatic potential energy due to $n(\vec{r})$, and is determined by self consistent calculations. Such self consistent calculations are used to calculate the wind force in metals.

Pseudopotential formalism has been used to calculate the wind force for impurities and vacancies [11] and to study the anisotropy in Z^* [12, 13]. Gupta [14, 15] calculated the wind force within the muffin tin potential formalism in noble and transition metals. Lodder [16] the KKR distorted-lattice approach to make calculations of wind force; later Van Ek [17] used this approach to calculate hydrogen electromigration in transition metals. In their 1962 paper [10] apart from the expression of wind force, Bosvieux and Friedel stated that the direct force on an impurity vanishes due to screening by conduction electrons. This began a debate, later

authors like Das and Peierls [18], Schaich [19] and Sorbello [20] gave arguments about the existence of the direct force.

2.2.1.3: Local Field

The form of the local electric field due to scattering from an ionic impurity was first studied by Landauer [21]. He found that charge distribution around the impurity gives a dipolar potential. This dipole field, called the residual resistivity dipole (RRD), is non- oscillatory and second order in potential. The RRD makes a significant contribution to the wind force expression of Bosvieux and Friedel when strong scattering is considered. Bosvieux and Friedel's calculation of the wind force uses the Born approximation and $n(\vec{r})$ is calculated to first order in potential, but as mentioned by Landauer [22], when scattering is strong corrections that are second order in potential should be taken into account in wind force calculations.

Landauer mentioned another effect of impurity scattering that contributes the direct force [22, 23]. In the presence of an attractive potential electron density in the immediate vicinity of impurity is increased (or reduced in the case of a repulsive potential). He mentioned that this effect might be seen as a local electric field in what he called the carrier density modulation (CDM) field. This field, for an attractive potential, is in the opposite direction from the applied bulk field so it gives an effective screening mechanism for the direct force. CDM effect is used by Das and Peierls [24] to write a formula for total force, $\vec{F} = -n_0(\Delta\rho/\rho)(-e)\vec{E}$, that Landauer called the Das-Peierls electromigration theorem [25]. Here $\Delta\rho$ shows the change in resistivity caused by a defect density of one per unit volume and n_0 is the electron

density of the pure metal. But their theorem does not give a correct explanation of experimental data, total force in their expression vanish as $\Delta\rho/\rho \to 0$ where experimentally it does not.

2.2.2: Empirical Relations

Although, as we have briefly discussed above, the theoretical discussion of the electromigration phenomena found considerable interest in solid state physics, experimental results are generally discussed by semi-empirical relations both due to the fact that it is very hard to quantify and calculate the force acting on the samples in real experimental situations and the experimental results seem to follow a semi-empirical formula first pointed out by Black [4]. Before starting to discuss the Black Equation and its relation to mechanical stress (especially in IC interconnects) it is fruitful to look at the diffusion mechanism in solids.

Diffusion of atoms in solids is generally associated with the defects or deviations from perfect crystalline structure. The diffusivity, D, follows more or less an Arrhenius type relation $D = D_0 e^{-\frac{E_a}{kT}}$. The diffusing atoms in the lattice must be in the immediate vicinity of a vacancy, grain boundary or surface which provides a pathway for atomic transport. Each type of crystal defect has an activation energy (E_a in above equation) that determines the ease by which the diffusion takes place. In general lattice vacancies require high activation energy for their formation. Comparatively, grain boundaries and interfaces have smaller activation energy and surfaces have the smallest and motion along them is the easiest. This order of

activation energies as well as their relative importance on one another in electromigration process is, of course, material dependent.

At constant temperature there is no preferential direction for atomic diffusion (this is an implication of Fick's First Law, see i.e.[26]), but lattice defects such as surfaces or grain boundaries break this symmetry by reducing the activation energy for motion along the defect. Still, along the defect, diffusion of an atom is random, say between forward and backward direction. However in the process of making an atomic jump while the atom is in a saddle point between energetically equally favorable locations, the momentum imparted by scattered electrons may promote diffusion in the direction of electron flow. Because of this property electromigration is many times defined as a current-biased diffusion process.

The electromigration process is often dominated with drift of atoms along a certain defect type in an applied field. This can be easily seen in couple of steps by using the Equation 2-1 for the total force acting on metal atoms and by using the Einstein relation to relate the mobility of atoms to diffusivity. With a simple derivation we can show that the relation for V_d , the drift velocity of atoms is

$$\vec{V}_d = \vec{j}\rho\frac{eZ^*}{kT}D_0 e^{-\frac{E_a}{kT}} \qquad \text{Equation 2-5}$$

The above equation shows that the drift velocity of the metal atoms is exponentially related to the activation energy and as long as the activation energies for different defect types are not very close to each other, the defect with smaller

activation energy will dominate the electromigration process and will be the determining factor in electromigration dynamics.

2.2.2.1: Black Equation

The discrepancy between the microscopic models of electromigration and the experimental results can easily be seen by taking a closer look at the form of the driving force in electromigration. If we use $\vec{j} = \frac{\vec{E}}{\rho}$ then one can write the driving force as

$$\vec{F} = Z^* e \rho \vec{j} \ . \qquad \text{Equation 2-6}$$

This equation would seem to predict that the failure should be dependent on applied current density, $\vec{j}$, and the lifetime should depend on the current density via $1/\vec{j}$. But the experimentally observed lifetimes in IC interconnects seem to obey a different semi-empirical relationship known as the Black Equation [4].

$$MTTF = Aj^{-n} e^{\frac{E_a}{kT}} \qquad \text{Equation 2-7}$$

In this formula MTTF (or t_{50}) is called the median time to failure and it describes the time for failure of 50% of a group of samples that prepared under identical conditions. "*A*" that appears in the formula is a sample-dependent constant, *j* is the

current density, n is a constant, E_a is the activation energy for the electromigration process, k is the Boltzman constant and T is the absolute temperature. The current density exponent, n, equals to 2 in Black's original formula, is empirically found between 1 and 7 [27].

In general, experiments for MTTF measurements are done under accelerated test conditions, namely under high current densities and temperatures. From the measured values of MTTF values the activation energy and the current density exponent may be determined. This is done by either holding temperature constant and changing the current density for measurement of n, or changing temperature while holding current density constant for measurement of activation energy.

One may qualitatively explain the physical origin of the parameters in this equation as follows. A depends on the conditions by which the interconnects are prepared because VLSI interconnects have polycrystalline structure and both orientation and the size distribution of the crystal boundaries affect the electromigration activity, structure of interconnects also affects the wide range of measured values of n. Interconnects show more electromigration activity at higher current densities and temperatures because motion along the defects become easier for electromigrating atoms.

As discussed in the following section, the disagreement between the theoretical understanding of the lifetimes and the experimentally observed behavior can be understood considering the stress buildup in electromigrating metal lines.

2.2.2.2: Effect of Stress Buildup in Electromigration

The inverse square dependence of the lifetime on current density can be resolved when one considers the gradient in the chemical potential, $\vec{\nabla}\mu$, as the real driving force for the diffusion of the metal atoms. Under these conditions one can write for the mass transport

$$\vec{J} = \frac{DC}{kT}\vec{\nabla}\mu \qquad \text{Equation 2-8}$$

where $\vec{J}$ is the mass transport, D is the diffusion coefficient and C is the concentration of diffusing atoms and kT is the thermal energy.

The most important extra contributions to the chemical potential gradient are the stress gradient and the concentration gradient of the vacancies. But at thermal equilibrium these two are not independent quantities, i.e. in passivated metal lines either via their natural oxide or via a refractory capping layer, an increased vacancy concentration will produce tensile stress. So it is enough to consider only one of these gradients. By introducing a concentration gradient term we write Equation 2-8 as

$$\vec{J} = D\left(\frac{Z^* e\rho\vec{j}}{kT}C - \frac{\partial C}{\partial x}\right) \qquad \text{Equation 2-9}$$

In configurations where there is a blocking boundary, i.e. with a vanishing mass flux where there is a diffusion barrier for the mass flux such as a contact to another

material, $J(0,t)=0$, and via the continuity equation, $\frac{\partial J}{\partial x}=\frac{dC}{dt}$, a solution is found [28] where the time to achieve a specific concentration is proportional to the inverse of square of the current density as in Black equation but with different temperature dependence in the pre-exponential factor i.e. $t_{50}=A\left(\frac{T}{j}\right)^2 e^{\frac{E_a}{kT}}$.

In passivated thin films, a large vacancy concentration cannot be supported. As electromigration progress, in one end of the conductor excess atoms accumulate and produce a compressive stress but in the other end of the conductor the vacancies do not exceed the thermal equilibrium value and simply annihilate in convenient sinks. But the vacancy annihilation in turn produces a reduction in the volume which can not be allowed in a passivated conductor and this volume change is transformed into a tensile stress buildup. So as current flows this stress buildup will increase and either will failure occur or the stress buildup will produce an equal and opposite force that will stop further electromigration activity. Given that the stress gradient represents a part in chemical potential one can rewrite Equation 2-9 as

$$\vec{J}=DC\left(\frac{Z^* e\rho\vec{j}}{kT}-\Omega\frac{\partial\vec{\sigma}}{\partial x}\right) \qquad \text{Equation 2-10}$$

where Ω is the activation volume and σ is the hydrostatic component of the mechanical stress. If the failure occurs when a critical stress is reached then time to reach that stress level can shown to be inversely proportional to the square of the current density [29]. So it is this opposite driving force that is responsible for the

failure described by the Black Equation. We can also see from Equation 2-10 that, at low enough current density, it is possible that stress gradient may exist in steady state without failure and the driving forces due to electromigration and the stress gradient may become equal when

$$\frac{\partial \sigma}{\partial x} = \frac{Z^* e \rho j}{\Omega} \qquad \text{Equation 2-11}$$

In this condition the electromigration will cease. This condition was experimentally observed initially by Ilan Blech [30-32]. By integrating Equation 2-11 over the stress profile one can easily derive the so called Blech length, length at which for a constant current density the electromigration activity will stop, and the Blech product $jl_{blech} \leq C_{blech}$ where C_{blech} is a material dependent constant. If the product of current and length in the conductor passes the value of C_{blech} then electromigration proceeds, if not than the electromigration does not take place.

2.2.2.3: Film Microstructure

Microstructure of polycrystalline thin films such as the grain size distribution has an important effect on electromigration activity and on main modes of electromigration. When Al and/or Al alloys such as Al/Cu or Al/Cu/Si are used in the IC interconnects, the main electromigration activity takes place in grain boundaries and/or in the bulk of the material. The reason is that, the oxide of the Al, Al_2O_3, forms a self limiting refractory shell which adheres extremely well to Al and makes an

excellent diffusion barrier. Therefore, the Al surface, when the oxide is present, is effectively shut off as a diffusion pathway. So even thought geometrically there is plenty of surface available, electromigration activity takes place mainly at grain boundaries and in some cases in the bulk of Al.

It is well known that IC interconnects become less reliable with smaller grain sizes [33]. If the grain size is small then there are many diffusive paths for electromigration activity and there might be continuous paths for diffusing atoms along the film. In interconnects where the width is very large compared to average grain size [a) in figure 2], mass flux is fairly uniform and there is not enough convergence or divergence of mass flux to produce electromigration failure. If the width of interconnect is decreased until it becomes comparable to the average grain size, electromigration activity increases. This increase continues until line width is approximately the same as the average grain size, it is this region [Figure 2-2 (b)] that shows a very high electromigration activity.

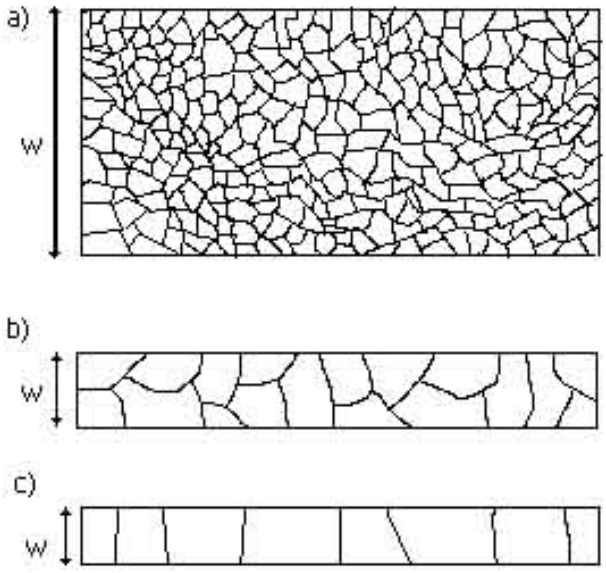

Figure 2-2. Change of the structure of polycrystalline interconnects as grain size/width ratio decreases (top view). a) Shows a polycrystalline film where width is much larger than average grain dimension. b) Shows a film where average grain dimension is approximately same size as width. c) Shows a metal film in bamboo structure. Adapted from reference [33].

In this regime both polygranular clusters that contain high diffusive pathways for mass flux and grains that span the width of the film coexist. As mass flows through the polygranular clusters it stops at these spanning grains which act as a diffusive barrier.

Then stress due to mass accumulation increases, grain boundaries where metal atoms accumulate show a high compressive stress and grain boundaries where metal atoms deplete shows a high tensile stress. These two points are generally the two ends of a polygranular cluster that is terminated by spanning grains. If the produced steady state stress is higher than some critical stress for deformation, electromigration failure occurs. This phenomenon can also be interpreted as a polygranular cluster that is

longer than Blech length, so mass transport takes place and results in electromigration failure.

With decreasing line widths more spanning grains that act as diffusion barriers, but the distance between them on average becomes shorter (or at least comparable to) the critical distance of the Blech length. So the stress that develops is smaller than the critical stress but big enough to induce a back flux that will stop electromigration activity, resulting in an increase in MTTF. If the width is small enough, then "bamboo" (or near bamboo) structures, where the width of the interconnect line is smaller than the average grain size, may develop [c) in figure 2]. In this case, grain boundary electromigration is no longer allowed and the only possible path for migrating atom is through the bulk of the grain. Thus it is very less likely that interconnect will fail due to electromigration. This produces a drastic increase in the MTTF.

2.3: Electromigration in Au

As we can understand from the discussion so far, electromigration studies in the literature mainly focused on the metals that are used in IC interconnects that is Al and/or Al alloys. The seemingly correct interpretation of experimental results depends on the consideration of stress buildup in samples which in turn depends on the fact that samples used in electromigration research are mainly (as a consequence of industrial drive) are made of Al and/or Al alloys which has a tough oxide on the surface and effectively shuts of the surface as a diffusion pathway. Even with

changing line widths of samples one can observe that the MTTF changes drastically indicating that main diffusion mechanism affects the electromigration dynamics.

Au, on the other hand, is the metal of choice in the fabrication of nanogaps for single molecule electronics because gold-thiol bonds are employed to attach the molecules under interest to the Au surface and Au being a noble metal does not form an oxide layer similar to aluminum when exposed to ambient conditions. Therefore, one might expect the electromigration dynamics to be different from the aluminum-based metallization. The above expectation is also supported by the fact that there is no reported Blech length for Au in the literature. So we conducted experiments (as explained in Chapter 4) to understand the electromigration dynamics in thin Au lines in the device geometry used in the single molecule electronics research to prepare nanogaps.

Chapter 3: Point Contacts and Nanogap Junctions

3.1: Introduction

Ohm's Law, $G = \sigma \frac{A}{L}$, describes the electrical resistance of everyday conductors such as a piece of copper wire. It tells us that the conductance, G (inverse of the resistance) is proportional to the cross sectional area of the conductor, A, and inversely proportional to its length, L. The constant of proportionality, σ, the conductivity, is a material property and is different for different conductors. However, as the size of objects approach the atomic scale, the material properties as we understand them in the macroscopic world start to break down; Ohm's law becomes invalid and even the concept of electrical conductance changes. The energy scales involved are high enough such that we can see visible effects of quantum nature of materials even at room temperature. In this very small scale, the definition and understanding of the electrical conductance is based on the idea that the conductance is equivalent to the transmission probability for incoming waves of electrons [21]. Although this idea originated initially from mesoscopic physics, it can be applied to almost all nanoscale objects such as nanotubes, single molecules, quantum point contacts of two dimensional electron gas (2DEG) and point contacts of metals.

In this chapter I will start with a review of the electrical transport through metallic point contacts and the experimental techniques to produce point contacts. Later I will discuss the idea behind the single molecule electronics and how the techniques used originally to fabricate point contacts of metals are used to prepare

nanogaps for testing electrical conductance of single molecules. This chapter provides a theoretical basis to discuss the results of the experiments we did to understand the electromigration properties of thin gold lines. It also provides a standpoint where we can relate our results with previous experimental results.

3.2: Conductance of point contacts of normal metals

In mesoscopic conductors we can divide the transport into two regimes depending on the relative sizes of the length of the conduction channel, L, and the elastic mean free path, ℓ_e. The elastic mean free path can be defined as the distance that an electron travels between two scattering events with impurities. We talk about the diffusive transport regime or the diffusive conduction when the electron makes many scattering events with the static impurities as it crosses the conduction channel (that is when $\ell_e \ll L$). Diffusive conduction, in analogy with statistical mechanics, can be described as a random walk problem with step size ℓ_e. On contrary, if the electron can travel the channel without any scattering (that is when $\ell_e \gg L$) than we talk about ballistic conduction or ballistic transport regime.

Another important length scale in mesoscopic systems to name is the phase coherence length, ℓ_ϕ. Over the phase coherence length an electron preserves its quantum coherence that is it "remembers" its past in the conductor. Phase coherence cannot be destroyed via scattering through static impurities but it may be destroyed via electron-electron scattering, electron-phonon scattering, or scattering through magnetic impurities with internal degrees of freedom. Generally in clean conductors

at low temperatures, the phase coherence length is an order of magnitude greater than the elastic mean free path.

Transport in everyday conductors is diffusive, but as the size of the conductor approaches the elastic mean free path or the phase coherence length, we can expect to describe the conductance different than as it is described via Ohm's law. We may also expect to see exotic effects due to quantum coherence.

The problem of such conductors was first considered by Sharvin [34]. He considered when the size of a metal contact is much smaller compared to the mean free path of the electrons such as a fine needle gently pressed into a conducting surface. In this case an approximate classical calculation can be made by treating the electrons arriving from each side as being in thermal equilibrium. The conductance will then be calculated in terms of the net number of electrons and the area of the contact. This so called Sharvin conductance, G_S, will then be given by

$$G_S = \frac{1}{4} v_F N_F e^2 A = \frac{2e^2}{h}\left(\frac{k_F}{2}\right)^2 A \qquad \text{Equation 3-1}$$

where h is the planks constant, k_F is the Fermi wave vector and A is the cross sectional area. Note that G_S does not depend on σ and ℓ_e but depends only on N_F and A. Power $(P = IV)$ is not dissipated in the contact but it is carried as the kinetic energy of the electrons passing through the contact and is dissipated in the leads.

The full quantum-mechanical description of conductance in mesoscopic devices where the phase coherence is maintained was first considered by Landauer [21]. To illustrate this one can assume an ideal one dimensional conductor where only

one channel (such a as a conduction subband) is occupied and contributing to the conductance (See figure 3-1).

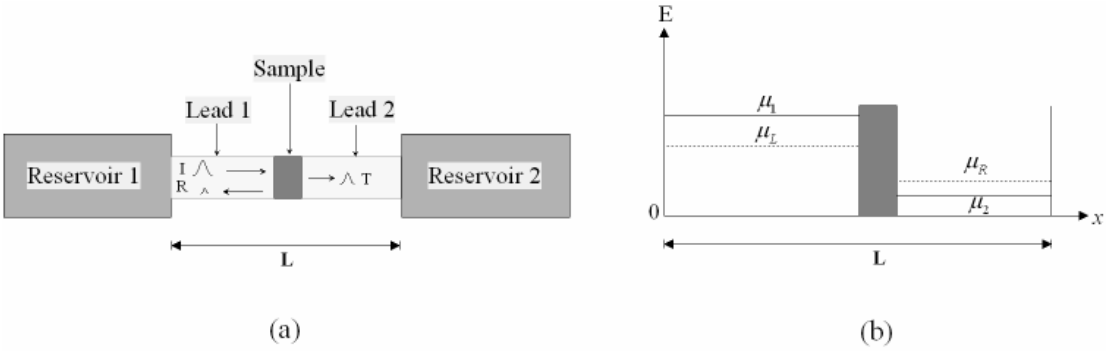

Figure 3-1. Conduction through a mesoscopic sample. (a) Shows the schematics of a mesoscopic sample in a channel of length L. Incident wave (I) is partially reflected through the sample (R) and partially transmitted (T). Leads 1 and 2 are connected to electron reservoirs where there is no phase coherence between particles. (b) Shows the energetics inside the channel. Due to the redistribution of charge, chemical potentials inside the channel are different from the chemical potential of the leads. Adapted from reference [35].

The right and the left electron reservoirs have their Fermi energies at μ_1 and μ_2 respectively. The chemical potentials in the leads are μ_L and μ_R due to the reduction of electron density in the left lead because of scattering and pile-up of the charge density at right due to transmitted electrons. The reservoirs randomize the phase of outgoing electrons so that there is no phase relation between particles in the contacts and the leads open up to the reservoirs adiabatically such that the outgoing electrons do not reflect back. In this case we can write the current as [35]

$$I = \frac{e}{\pi}\left[\int_0^{\mu_1} dE\left(\frac{dk}{dE}\right)v(k)\tau(E) - \int_0^{\mu_2} dE\left(\frac{dk'}{dE}\right)v(k')\tau(E)\right] = \frac{2e}{h}\int_{\mu_1}^{\mu_2} dE\tau(E)$$

Equation 3-2

where the integration is over the left and right going states (k and k' respectively), $v(k)$ is the velocity of an electron in state k and $\tau(E)$ is the energy dependent transmission probability. In the linear response regime (for small applied voltage), we may assume that $\tau(E)$ is energy independent ($\tau(E) = \tau$) and we can write the current as

$$I = \frac{2e}{h}(\mu_1 - \mu_2)$$ Equation 3-3

The voltage drop across the sample is $eV = (\mu_L - \mu_R)$ and is less than $(\mu_1 - \mu_2)$ due to the redistribution of charge. One can show that [35] in the four terminal configuration where the voltage drop is measured at a different set of leads $(\mu_1 - \mu_2) = \frac{\tau}{(1-\tau)}(\mu_L - \mu_R)$ and we can write conductance as

$$G = \left(\frac{2e^2}{h}\right)\frac{\tau}{(1-\tau)}$$ Equation 3-4

In the two terminal measurements $(\mu_1 - \mu_2) = (\mu_L - \mu_R)$ since the voltage and current are measured through the same set of contacts and we can write the conductance as

$$G = \frac{2e^2}{h}\tau \qquad \text{Equation 3-5}$$

The factor $\frac{2e^2}{h}$ is called as the quantum unit of conductance or simply quantum conductance, G_o, and can be defined as the maximum conductance the channel will have in the case of perfect transmission (i.e. $\tau = 1$).

One can generalize the above result into two probe multichannel configuration as

$$G = \frac{2e^2}{h}\sum_n \tau_n \qquad \text{Equation 3-6}$$

where the sum is over all the channels contributing to conductance. The stepwise change of conductance in mesoscopic devices first demonstrated in 2DEG devices [36, 37]. Along with the mesoscopic 2DEG devices one can apply Landauer formula (Equation 3-6) to atomic sized conductors as well. In 2DEG devices the splitting between the quantum channels is $\sim 1meV$. This means that, to observe quantum effects we need to cool down the devices to liquid helium temperatures. On contrary in few-atom metallic contacts we may estimate the mode splitting from the Fermi

wavelength, $\lambda_F \simeq 5A^0$, as $\frac{\pi^2\hbar^2}{2m{\lambda_F}^2} \sim 1eV$. This implies that we may observe the quantum effects even at room temperature. But we should keep in mind that as oppose to 2DEG devices where we can change the potential profile and the number of conduction channels inside the channel smoothly by adjusting the gate field, in metallic contacts where the limiting property is the inherent atomic granularity in reducing the contact size, we should not expect the conductance to reduce by the simple multiples of quantum conductance, G_o due to lack of perfect transmission.

3.3: Methods of Fabricating Point Contacts

Early experimental studies of ballistic contacts of metals are done with so called Spear-Anvil technique [38, 39]. The technique consisted of a type of differential screw mechanism to press a needle gently on a metallic surface. Using the technique it is possible to get contact sizes down to 10 nm (deduced from the resistance of contacts using Sharvin formula). But to study contacts in quantum regime where one needs to have contact sizes comparable to the Fermi wavelength one needs much more stable and precise control over the contact. Two techniques, namely the scanning tunneling microscope (STM) and the mechanically controllable break junction (MCBJ) gives such precise control, and therefore they are extensively used in the study of point contacts.

After its invention [40], STM was used extensively in the study of metallic point contacts (see i.e. [41] and the references therein) under variety of experimental conditions such as in ambient conditions, in vacuum, under cryogenic temperatures

etc. The inherent stability of the STM environment and ability to measure displacement of the STM tip from the surface let measuring of conductance vs. displacement measurements in variety of metals. In the research for metallic point contacts, even the direct observation of atomic chains of gold are made by fabricating an STM with the tip apex at the focal point of an High Resolution Transmission Electron Microscope (HRTEM) [42].

Along with the STM, probably the most extensively used method in the study of point contacts is the MCBJ technique [43]. The technique consists of fixing a metal wire under investigation on elastic substrate using some form of epoxy. Later by using a three point bending configuration where the substrate is pushed in the middle from below towards the counter supports which are at the two ends of the substrate and then by gradually increasing the bending of the substrate, it is possible to reach few-atom configuration. Mostly a notch in the wire is made before bending to assist the process of forming contacts. This method produces clean contacts under variety of experimental configurations such as UHV, ambient, cryogenics etc.

Both in STM and MCBJ experiments possible quantization effects are customarily investigated via constructing conductance histograms from large sets of data (i.e. on the order of ~ 10000 individual curves see i.e.[44]). The histograms are constructed under the assumption that during the contact breaking any effective contact size is equally probable. The investigation of gold nanocontacts with the histogram method shows a pronounced peak at $1G_o$ and smaller peaks at $2G_o$ and $3G_o$. The peak at $1G_o$ survives under most experimental conditions and is attributed to single chain of gold atoms [41].

3.4: Fabrication of Nanogaps for Single Molecule Electronics

Research activity on single molecule electronics was driven by both the scientific curiosity to understand how the conduction through single molecules take place and the high expected technological payoff by creating the smallest electronic devices in the history of electronics.

Investigation of the conduction properties of single molecules generally requires a metal-molecule-metal configuration where the choice of metal is often gold due to the facts that gold surface does not have a natural oxide layer and the molecules under investigation are readily bonded to gold via thiol bonds.

Electrodes for single molecules naturally have to be on order the size of the molecule where this requirement singles out conventional lithography methods for electrode fabrication such as electron beam and photolithography. Many groups have used the techniques borrowed from the point contact experiments to measure the conductance of single molecules [45-51]. Both STM and MCBJ give fine control over the electrode separation but they have their drawbacks. In STM it is not possible to fabricate a gate electrode that might change the electrostatic doping of the molecules and in MCBJ it is only recently shown [52] that it is possible to place a gate electrode, but this requires complicated fabrication steps and MCBJ show large drifts in changing thermal conditions. On the other hand in nanogaps fabricated via electromigration a gate electrode is easily incorporated under the gold line and the junctions are thermally stable. Therefore nanogaps fabricated by electromigration (although the electromigration dynamics are not well understood) have been used by many research groups for molecular-scale electrode fabrication.

In the next chapter we will explain our experimental studies of nanogap fabrication via electromigration in order to understand electromigration dynamics of thin gold lines connected the bulk electrodes and we will discuss our experimental results.

Chapter 4: Formation of Gold Nanogaps via Electromigration

4.1: Introduction

Gaps formed via electromigration have been used in single molecule electronics extensively by many groups to measure the conductance properties of single molecules. It has also been suggested [5, 6, 53] that the dominant failure mechanism in such electrically stressed nanowires is thermally assisted electromigration. As we have explained in section 2.2.2.1, the Black formula suggests that both current and local temperature (due to Joule heating) affects the electromigration process and they both change rapidly during the electromigration of short wire. Understanding the role of current and temperature is then would be critical to design circuits that will produce desired nanogap junctions controllably.

It has been recently shown by two groups [54, 55] that by employing a feedback loop it is possible to slow down the rate of electromigration and to produce nanogap junctions of a desired resistance (and presumably gap size) in a controllable manner. It was also proposed that the controllable electromigration occurs at constant applied power and it is triggered at a constant temperature. To understand the electromigration dynamics of Au lines and possibly to verify the above propositions, we implemented this technique and experimented on wires of varying cross sectional areas and varying lengths. We also tried to understand the role of the feedback loop in controlling nanogap formation that is via a suitable design of devices, whether one can produce small nanogaps by using a simple voltage ramp or not.

4.2: Device Fabrication and Measurement Setup

We have fabricated our devices by using electron beam lithography and metal deposition process as we describe below.

Electron beam lithography (EBL or e-beam lithography) can be defined as a specialized technique for creating extremely fine patterns that could not be possible to create otherwise by using optical lithography tools. EBL in brief consists of scanning a beam of electrons across a surface covered with a film of resist film that is sensitive to the exposure of electrons. Therefore by exposing the surface with a beam of electrons it is possible to deposit energy in the desired pattern in the resist film. Electron beam resists can be viewed as the reading and transfer media for e-beam lithography. The usual resists are polymers that are dissolved in a liquid solvent. The resist is dropped onto a substrate that is then spun at high rpm values (~ 4000-6000) to form a layer of coating. The rpm value of the spin determines the thickness of the coating. After baking out the casting solvent, exposure to electrons modifies the resist leaving it either more soluble (positive) or less soluble (negative) in a developer. The created pattern is then transferred to substrate either through an etch process (such as plasma or wet chemical) or through material deposition and liftoff. In material deposition and liftoff process, the material is evaporated (such as thermal evaporation or e-beam evaporation) or sputtered (such as SiO_2 or refractory metals) from a material source in a vacuum chamber onto the substrate and resist layer. Later the resist is lifted off (or washed away) in a solvent such as acetone. Mostly two layers of polymers (bilayer resist) used the bottom layer being more sensitive to electron beams

compared to top layer to generate an undercut resist profile that will aid the liftoff process by providing a clean separation of materials.

Commonly, to produce a slight undercut two layers of PMMA (Poly-methyl methacrylate) with different molecular weights (bottom layer being low molecular weight compared to top layer) is used. To produce a large undercut the bottom layer is spun from copolymer PMMA and top layer from PMMA. In the later case the resist after e-beam exposure developed in methyl isobutyl ketone: isopropanol (MIBK: IPA) solution where MIBK develops PMMA and IPA develops the copolymer PMMA. Therefore by using high ratio MIBK: IPA (such as 1:3 or more) or developing in IPA only after an initial MIBK: IPA development structures such as resist bridges of PMMA can be made. Figure 4.1 shows the above procedure schematically.

The recipe I used for electron beam lithography in device fabrication is as follows. I prepared my samples on SiO_2 (500nm)/Si substrates. I used bilayer resist where the bottom layer is spun from MMA at 4500 rpm for 45 seconds producing a 300 nm thick coating. After spinning the MMA I baked the chip on a hot plate for 15 minutes at 150 ^{0}C to evaporate the solvent (Chlorobenzine in this case). The top layer is spun from PMMA at 6000 rpm for 45 seconds producing 100 nm coating. I again bake the chip for 15 minutes at hot plate at $150\,^0C$. I then used the as-prepared chips in e-beam lithography. After metal deposition, lift-off of the resist and excess metal is performed by immersing the chip in acetone for 45 minutes to 2 hours depending on the resist thickness and the type of metallization.

The patterns to be exposed in EBL are designed with CAD software, and the Nanoscale Pattern Generation System (NPGS) is used to control the motion of electron beam in a Scanning Electron Microscope (SEM, FEI model XL-30).

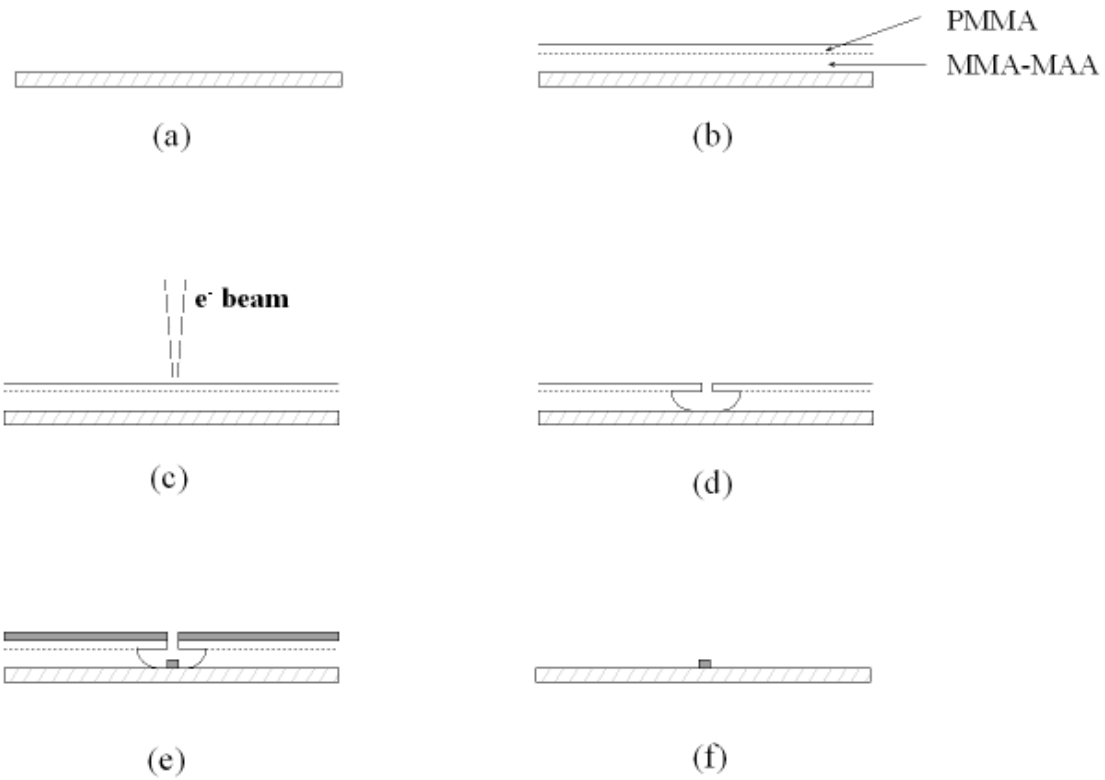

Figure 4-1. Schematic of the electron beam lithography technique. (a) Clean starting substrate. (b) Substrate is covered with bilayer resist. Bottom layer is spun from MMA-MAA and the top later from PMMA to produce a large undercut. (c) Exposure of resist to electron beam. (d) The exposed resist is developed in MIBK-IPA solution (e) Metal deposition on the created pattern. Metal is deposited to both the surface of the resist and the substrate through the window opened up in the resist after development. (f) After the liftoff, resist is washed off the surface and only the metal deposited on the substrate is left behind.

I prepared my devices in two steps of electron beam lithography. An SEM microscopy picture of a typical device is shown in figure 4-2. I first fabricated the thin gold lines with no adhesion layer. In the second electron beam lithography step the bulk of the electrodes and the contact pads are fabricated by depositing typically 5 nm chromium adhesion layer and 70 nm gold.

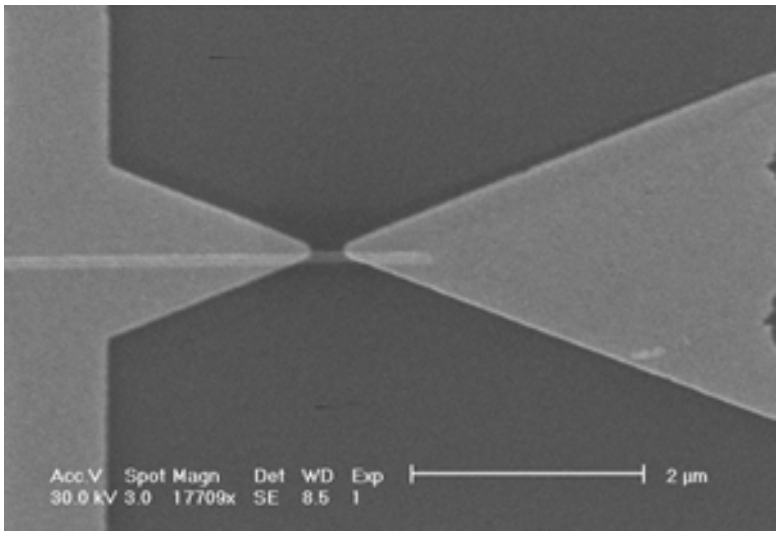

Figure 4-2. SEM Micrograph of a typical device used in controllable electromigration experiments.

After fabrication I cleaned the devices with oxygen plasma typically at 300 militorr oxygen pressure and 300 Watts for 15-30 seconds to remove the possible resist residues from the surface and to be sure that there are no organic contamination on the surface. I later fixed my chips on the chip carriers with General Electric (GE) varnish, and connected the electrical features on the chip to the leads on the carrier

using an ultrasonic wire bonder. I used a ^{4}He gas-flow cryostat (Desert Cryogenics) to take the measurements at temperature ranges from 1.2-325 K. The schematic of the measurement setup I used in my experiments is shown in Figure 4-3. I used a Keithley 2400 multimeter as voltage source and I measured the current by using an Ithaco 1211 current amplifier and an Agilent multimeter. The setup and the feedback (as explained in next section) are controlled via measurement programs written in LabVIEW language.

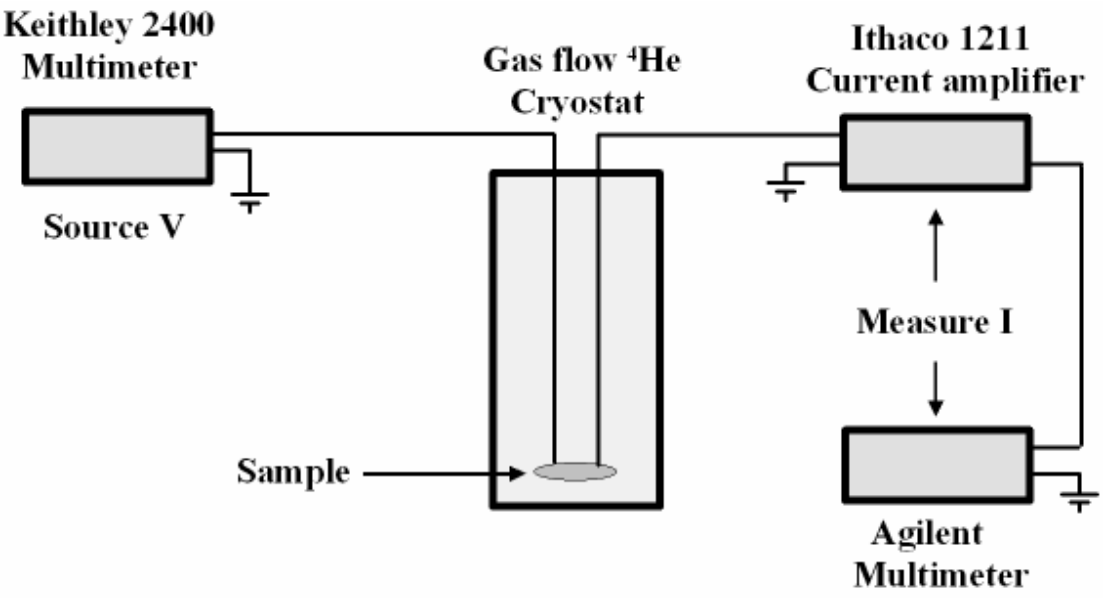

Figure 4-3. Measurement setup used in controllable electromigration. A Keithley 2400 Multimeter is used as a voltage source and devices are measured in a 4He gas flow cryostat. Current is measured using an Ithaco 1211 transimpedance amplifier and an Agilent Multimeter. The setup is computer controlled by measurement programs written in LabVIEW language.

4.3: Feedback Controlled Electromigration

To control the electromigration process, I used a feedback scheme similar to Ref. [54] consisting of the following steps: I first measure a reference conductance value at a voltage of 100 mV. I then increase the voltage until the conductance drops by a set fraction (typically 2-5 %) of the reference conductance value. The value of the fraction is chosen such that the change in conductance is due to electromigration as opposed to decrease of conductance due to bare joule heating. At this point, the voltage is ramped down by 50 to 100 mV (at a rate of 50 mV/s) and a new reference conductance value is measured. We repeat this process until the desired conductance value is reached. A typical I vs. V_{bias} curve of such feedback controlled electromigration is shown in figure 4-4. Note that the current as a function of bias voltage is a multivalued function.

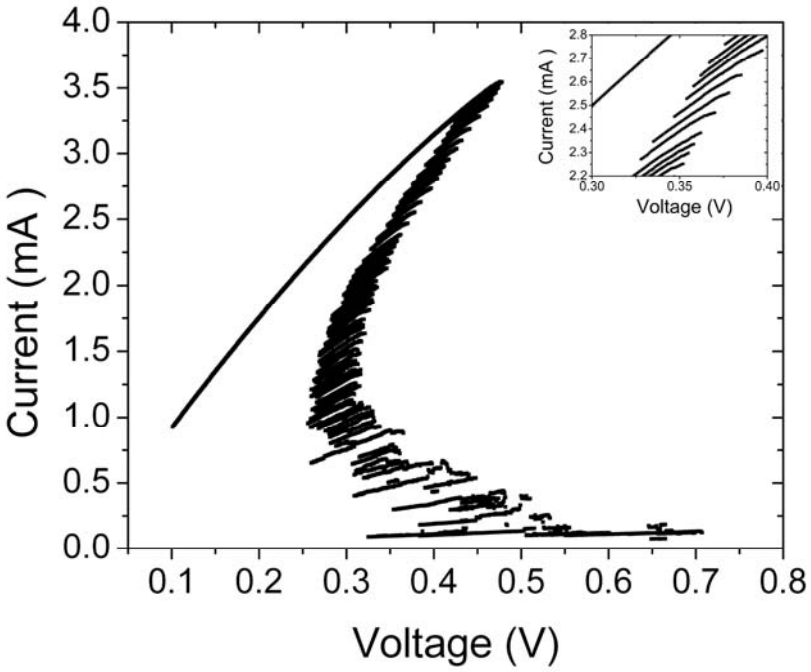

Figure 4-4. I vs. V_{bias} curve of a typical feedback controlled electromigration process. The inset shows the progression of the electromigration in fine details.

As we have explained in Chapter 2, considerable electromigration activity starts when atoms become mobile enough. If the local temperature increase of the electromigrating wire supplies this energy, one may expect the electromigration process to be highly temperature dependent and not to start before the wire becomes gets hot enough due to joule heating. For a uniform wire one expects the heating to start from the midsection, but for a non uniform wire it will start from the point where the scattering is concentrated. Figure 4-5 demonstrates the effect of temperature increase on electromigration of our samples. The data labeled A shows a smooth I vs. V_{bias} curve indicating that the electromigration has not begun in the gold wire.

Although we observe a resistance increase with increasing bias, we found that if we stop the voltage in bias in region A, this resistance increase is reversible. Such a reversible resistance increase shows that the gold wire heats up before electromigration begins. The data labeled B shows that after this initial heating, the gold wire begins to change resistance irreversibly due to electromigration. The data labeled C shows that one can stop and restart electromigration before the gold wire totally fails. $I - V_{\text{bias}}$ curves of two bias processes perfectly match each other indicating that in the second biasing process the gold wire first heats up to the temperature where significant electromigration takes place, and the electromigration restarts.

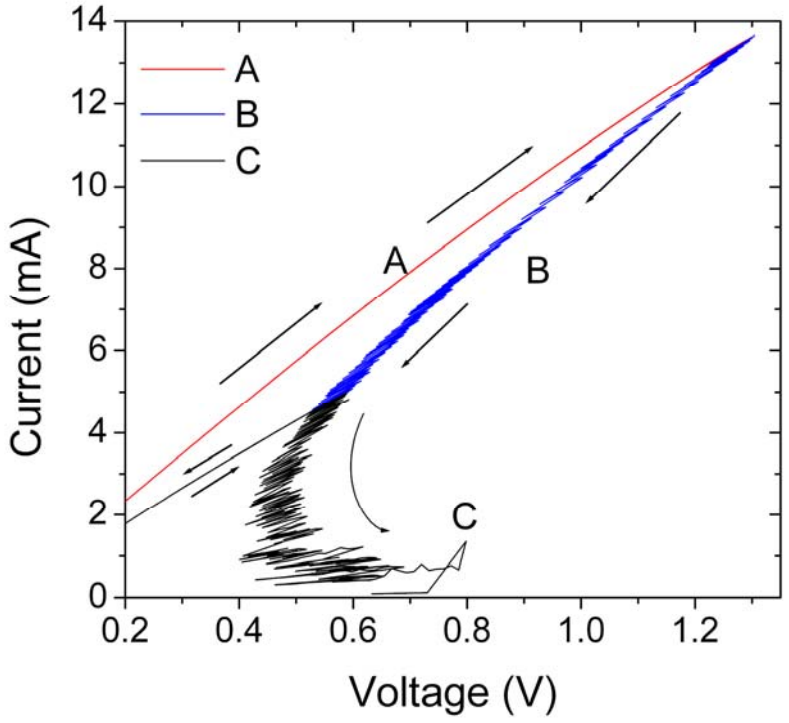

Figure 4-5. Current vs. bias voltage during the feedback-controlled electromigration of an Au wire at T=1.3 K. Part A is a smooth curve indicating than the EM has not begun whereas in part B the resistance of the line increases irreversibly due to EM. Both parts A and B are recorded in a single voltage biasing process, producing a final resistance of ~120 Ω. At this point the voltage was reduced to zero for some time. When the bias process was restarted in C, the wire resistance is the same, demonstrating that the EM process may be frozen by turning off the voltage.

In the analysis of my data, I will assume that the total resistance of the circuit R is the sum of two resistors R_L, the lead resistance (equals to the resistance measured at low voltage bias) and R_J, the resistance of the "junction", the weak spot formed in the wire by electromigration; i.e., $R_J = 0$ initially. I then can calculate the power dissipated in the junction as $P_J = I^2 R_J$.

Note that R_J includes a contribution from the resistance change of the leads upon heating, and the heating due to the resistance of the nanowire itself is ignored. Therefore, P_J is a rough estimate of the power that is heating the junction, but should be valid when R_J is significantly non-zero.

Figure 4-6 shows P_J versus $V_J = IR_J$, where the inset graph is the corresponding $I - V_{\text{bias}}$ curve of the data. After the junction resistance begins to increase due to electromigration [labeled as (a) in both the graph and the inset], the power dissipated in the junction reaches a relatively constant value. Constant power dissipation in the junction is observed until the resistance of the junction becomes on the order of several kiloohms. At the resistance values of several kiloohms, one should treat the junction as being in the Sharvin or mesoscopic limit and one should not expect all the energy of the electrons to be dissipated in the junction. Therefore our classical description of power dissipation becomes invalid.

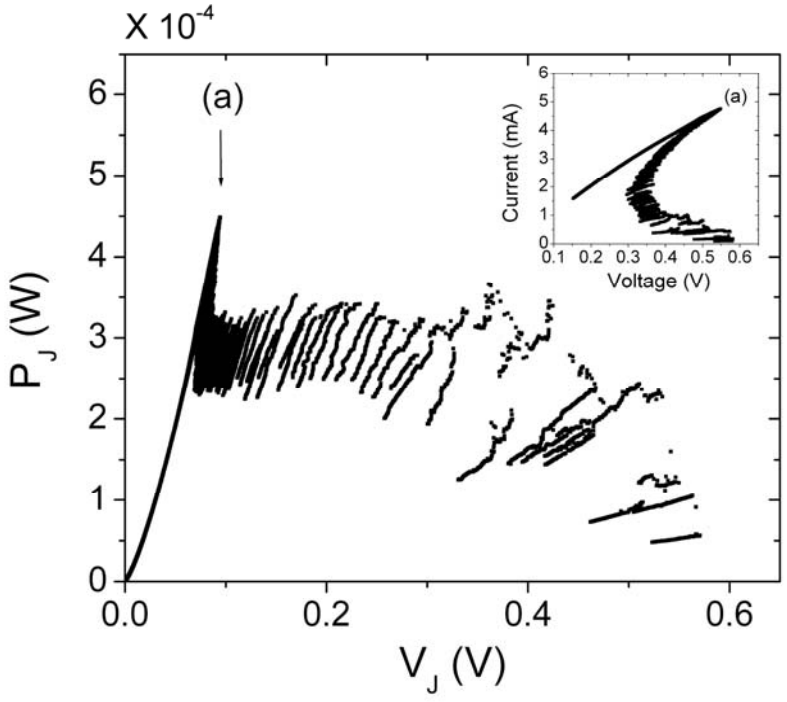

Figure 4-6. Power dissipated in the junction P_J vs. the voltage drop at the junction V_J (quantities defined in text). The irreversible change in resistance due to electromigration starts at the point labeled (a). Inset shows the corresponding current vs. bias voltage data. The starting nanowire has dimensions 830 nm long x 60 nm wide x 25 nm thick; the length and width of the nanowire is determined using SEM, and thickness by quartz crystal monitor during gold film deposition.

As we can see, temperature of the wire plays an important role in the electromigration process. By looking at the change of R_J as a function of the junction voltage we can get further insight on whether the electromigration process is primarily temperature or bias controlled. A primarily temperature-controlled electromigration should produce $R_J \sim V_J^2$ but a primarily bias-controlled junction should produce $R_J \sim V_J$. In figure 4-7 we plot the change of the junction resistance as a function of junction voltage during electromigration. The solid lines are guide to

eye and showing $R \sim V^2$ and the dashed lines are showing $R \sim V$ for comparison. Figure 4-7 indicates a primarily temperature controlled electromigration process.

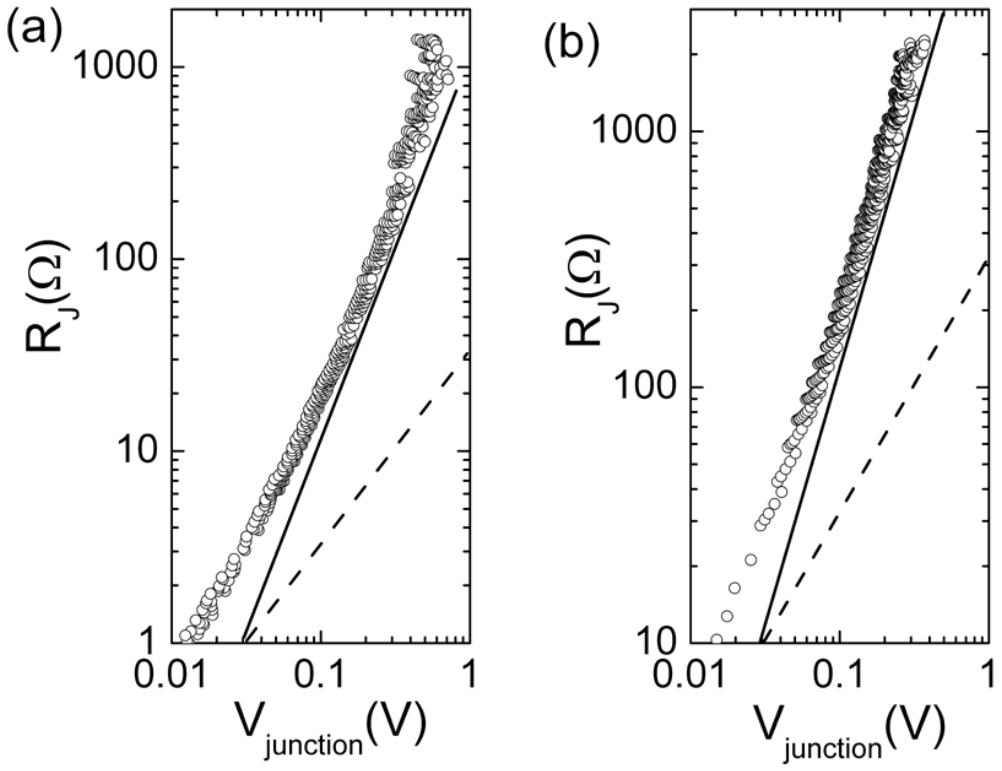

Figure 4-7. Evolution of junction resistance as a function of junction voltage. In both figure (a) and (b) the solid lines are guide to eye showing R ~ V^2 and the dashed lines are showing R~V.

If the junction temperature is the main factor in controlling the electromigration, one expects for better thermally coupled junctions more power to be dissipated at the junction. Since the thermal conductance of the wire is proportional to the cross-sectional area, the power required to maintain a given wire temperature

should also be proportional to the area. To test this point we fabricated wires with different cross sectional areas. Figure 4-8 shows that the power dissipated in the junction during electromigration is proportional to the nanowire area.

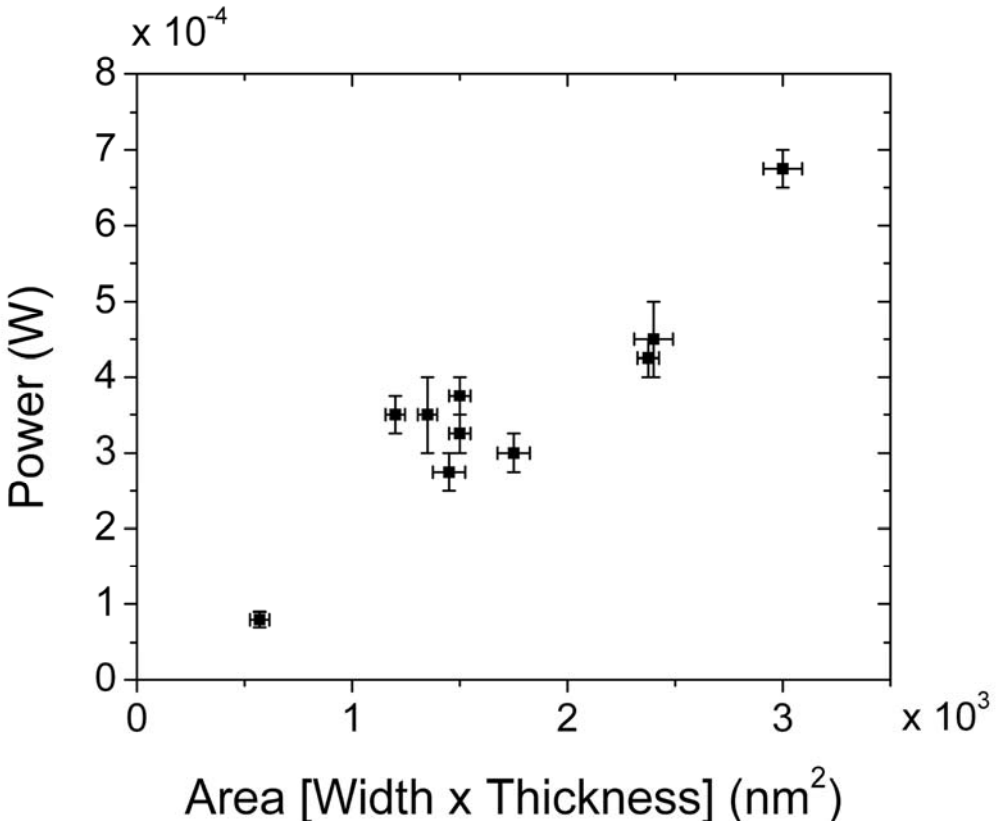

Figure 4-8. Power dissipated in the junction during electromigration vs. nanowire cross-sectional area. The power is the average power in the region of near-constant power seen in Figure 4-6.

Therefore, we conclude from figure 4-8 and the relatively constant power observed in figure 4-6 that the electromigration rate is dominated by temperature and the feedback scheme operates to control the wire temperature.

We estimate the temperature of the junction T_J during electromigration as follows. We neglect the heat conduction to SiO_2 substrate by considering the relative magnitude of the thermal conductivity of gold and SiO_2 and due to the thermal resistance between the gold line and SiO_2 substrate [56]. We also consider the contacts as infinite heat sinks at T = 1.5 K. The temperature at the midpoint of a wire with uniform power dissipation over its volume is given by $T_J = \frac{PL^2}{8V\kappa}$, where *P*, *V*, *L* and κ are, respectively , the total power generated in the nanowire, the volume and the length of the nanowire, and the thermal conductivity of gold [57]. For the nanowire in figure 4-6, the maximum power estimated as ~ 0.67 mW (including P_J at point [Fig. 4-6(a)] and the additional power generated due to the estimated resistance $11\,\Omega$ of the nanowire at $T = 1.5$ K. Using the thermal conductivity of gold as $\geq 320 W/mK$ (the room temperature value for bulk gold) we estimate $T_J \leq 145$ K. If we estimate that all the power is generated at the center of the nanowire and carried out to the leads by the nanowire, then $T_J = \frac{PL^2}{4V\kappa} \leq 290$ K; which is still low enough to allow the study of many molecular adsorbates without desorption or dissociation of the molecules. Note that if we include the power loss to the substrate as well, then this will lead us to a lower temperature value which will not change our main conclusion.

We will now discuss why the feedback process is feasible. The thermal time constant, which can be thought as the characteristic decay time of the temperature variations in a one dimensional heat conduction, [58] $\tau_{th} = \frac{L^2 \rho C_p}{\pi^2 \kappa}$, where C_p is the specific heat and ρ is the density, is less than 1 nanosecond in our nanowires; much

faster than our feedback circuit. This suggests that the electromigration process must occur very slowly. If this is the case, is feedback needed at all?

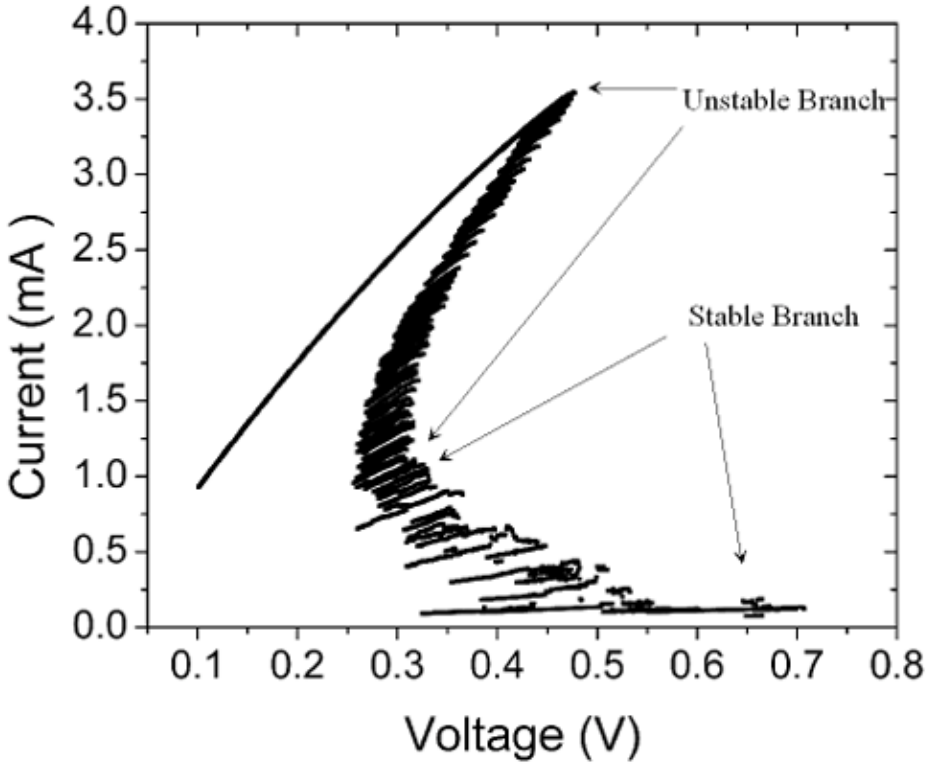

Figure 4-9. Stable and unstable regimes in controllable electromigration of a typical device.

Following the I-V_{bias} curve of a typical electromigration process, such as Figure 4-9, we can see that I, and hence R, is a multivalued function at a given V_{bias}. Assuming that the junction temperature is proportional to the power dissipated in the junction, that is $T_J \propto I^2 R_J$, we can write

$$T_j \propto \frac{R_j}{\left(R_j + R_L\right)^2}$$ Equation 4-1

The change of junction temperature with junction resistance is then given by

$$\frac{dT_j}{dR_j} \propto \left[\frac{1}{\left(R_j + R_L\right)^2} - \frac{2R_j}{\left(R_j + R_L\right)^3}\right]$$ Equation 4-2

From above formula we can see that once the electromigration starts the thermal runaway can be prevented if $\frac{dT_j}{dR_j} < 0$. We call this regime as the stable branch of the I-V_{bias} curve (see i.e. Figure 4-9) and it corresponds to the regime where the junction resistance is greater than the lead resistance, $R_J > R_L$. If the junction resistance is less than the lead resistance, that is $R_J < R_L$, than $\frac{dT_j}{dR_j} > 0$. We call this regime as the unstable branch in the I-V_{bias} curve. So when the junction is in the stable regime electromigration progress in a self limiting fashion and when the junction is in unstable regime electromigration increases the junction resistance and this will produce more heat and more increase in the junction resistance. So we may expect a transition from stable to unstable regime when we turn off the feedback as electromigration progress. Figure 4-10 illustrates this instability.

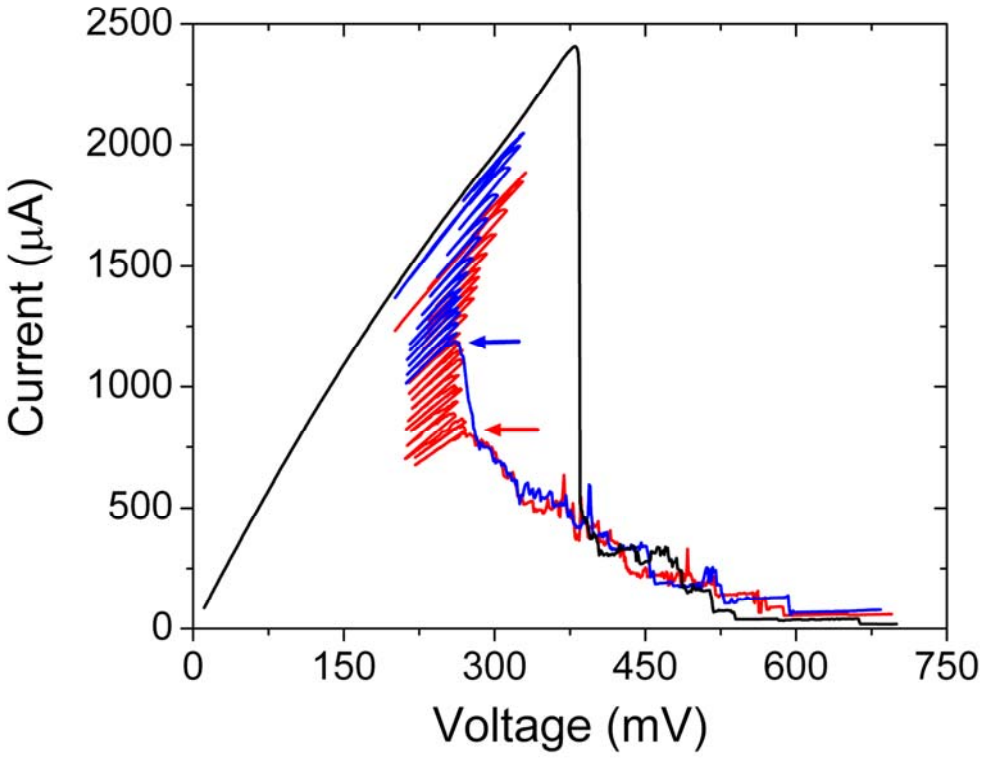

Figure 4-10. Current vs. bias voltage during the electromigration of three similar gold wires (600-700 nm long x 40 nm wide x 15 nm thick) at T=1.3 K. For the blue and red curves, the external feedback is turned off at the points marked by the blue and red arrows respectively. For the black curve, no external feedback was used.

In figure 4-10, we turned off the feedback at various points during the electromigration process and solely ramped the voltage upwards at a fixed rate. The red curve shows the feedback turned off while on the stable I-V_{bias} branch (positive $\frac{dV_{\text{bias}}}{dR}$); the current decreases smoothly with increasing voltage from this point. However, when the feedback is turned off on the unstable I-V_{bias} branch

(negative $\frac{dV_{\text{bias}}}{dR}$; blue and black curves), the current drops rapidly to the stable branch at the same V_{bias}. Thus the feedback scheme is only necessary to produce final resistances $R_J < R_L$; with suitable circuit design (minimization of R_L; i.e. short nanowires with highly conducting leads) small final R_J's may be produced using a simple voltage ramp.

Note that in some circuits [i.e. see figure 4-11 (a)] the stable I-V_{bias} branch does not extend beyond the unstable branch; in such cases a simple voltage ramp causes abrupt failure of the wire by melting (as observed via post-mortem SEM micrographs [i.e. see figure 4-11 (b)], resulting in large $(>10 \text{ nm})$ gaps.

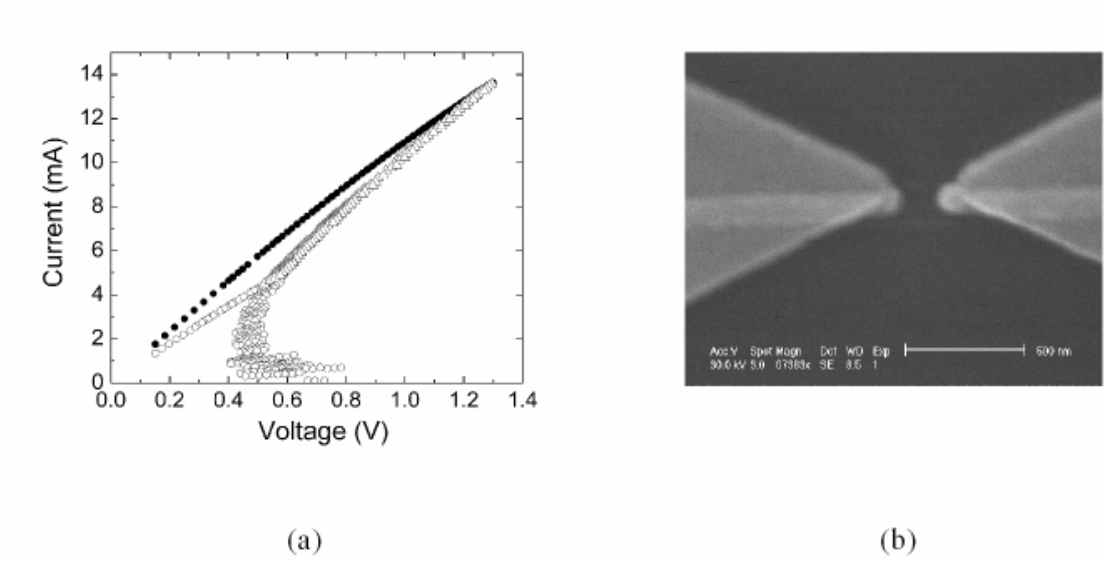

Figure 4-11. Electromigration of a device where stable branch does not extend beyond unstable branch. (a) Shows the I-Vbias curve a device where the stable branch does not extend the unstable branch. (b) Shows the post-mortem SEM micrograph of a device where simple voltage ramp results in a large gap via melting. The scale bar in (b) is 500 nm. Note that the controllable electromigration data in (a) and the SEM micrograph are taken from different devices,

In the last stages of the electromigration process the electromigrating junction starts to approach the mesoscopic limit. In this region we don't observe a smooth change of the conductance, but instead we observe change of conductance in discrete steps on the order of conductance quantum G_o. Figure 4-12 shows conductance change in units of conductance quantum vs. time in the last stages of controlled electromigration process.

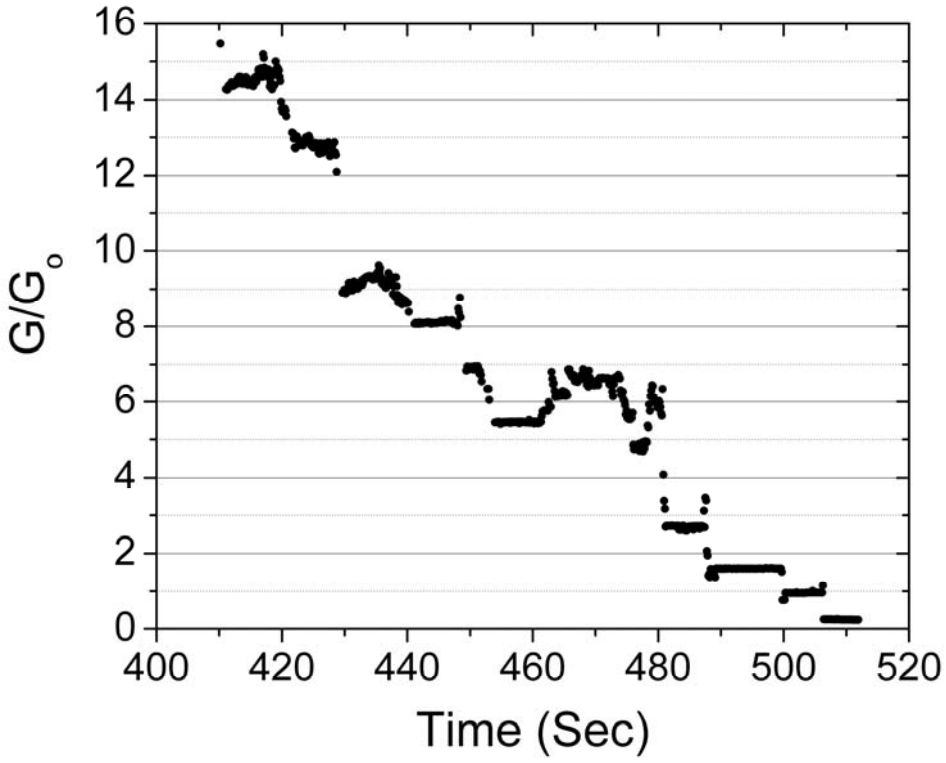

Figure 4-12. Conductance change in discrete steps of conductance quantum. The steps are on the order of, but not at exact multiples of Go indicating a mesoscopic junction.

In this regime, we often observed conductance plateaus on the order of but not at exact multiples of G_o. We ascribe the observed changes of conductance to changes in the atomic configuration of the contact. Although we don't observe strict quantization of conductance, the conductance is still determined by a limited number of modes where not all the modes are showing perfect transparency [41, 59]. The $1\,G_o$ level is an exception to this where formation of an atomic chain of Au atoms and single atom contacts are observed [42, 60]. Figure 4-13 shows $I - V_{bias}$ curve of a junction after

we stop electromigration at $\sim 1\,G_o$ and voltage bias up to failure. We ascribe the conductance plateau at $\sim 1\,G_o$ to a single atom contact due to both linear $I - V_{bias}$ curve and the high voltage value it sustains before failure.

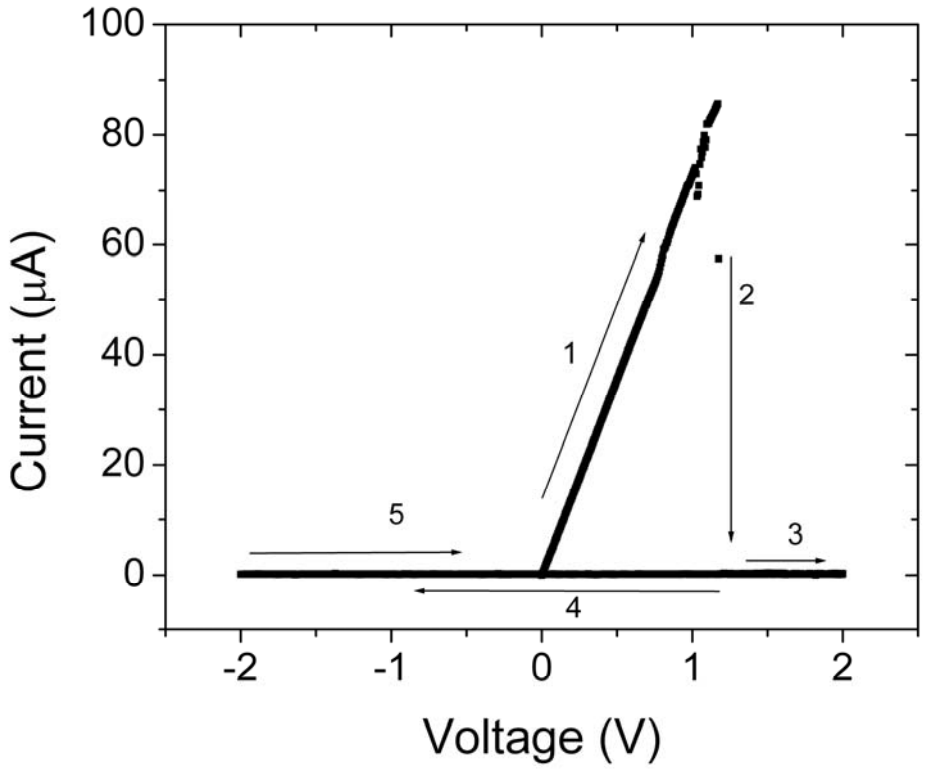

Figure 4-13. I-V_{bias} curve of a junction where the electromigration is stopped at 1Go. Both the linear I-V_{bias} curve and the high voltage value at failure indicates a single atom contact. Numbers on the figure shows the direction of voltage bias.

In junctions where we stopped electromigration when the final conductance is less than G_o, we often observed two types of highly conductive non-linear $I - V_{bias}$

curves as shown in figures 4-14 (a) and 4-14 (b). Figure 4-14 (a) shows a junction where we observed highly conductive nonlinear $I - V_{bias}$ curves indicating quantum mechanical tunneling through a thin potential barrier [61] and Figure 4-14 (b) shows $I - V_{bias}$ curves indicating transport through a Coulomb Blockaded junction as observed in similar experiments [62]

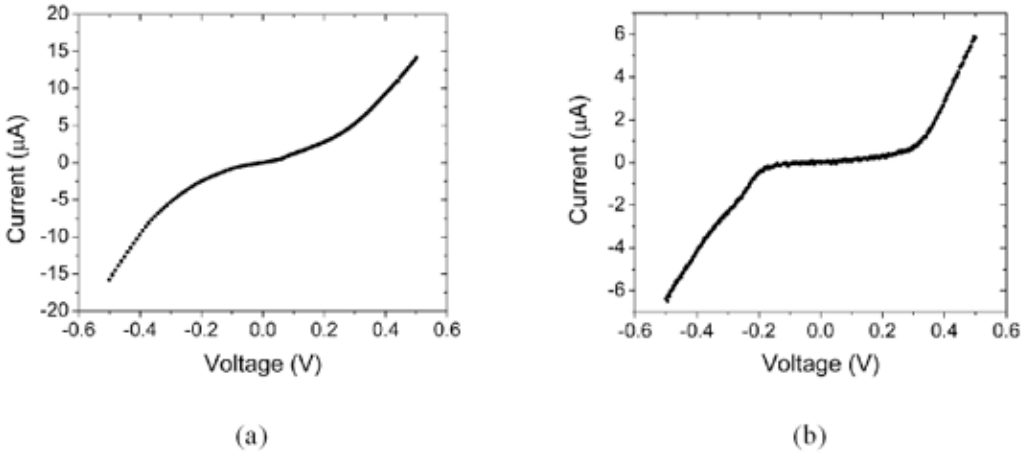

Figure 4-14. I-V_{bias} curves after junction formation. (a) Shows highly conductive nonlinear I-V_{bias} curve with positive curvature. (b) Shows an I-V_{bias} curve indicating Coulomb blockade.

4.4: Conclusion

In conclusion, we performed controllable electromigration on nanowires with different cross sections. We found that the average power dissipated in the junction during electromigration increases linearly with the area of the junction indicating temperature control of the process and confirming that the mechanism is thermally-assisted electromigration. Using the maximum power dissipated in a typical device, we estimate the junction temperature during electromigration performed at $T = 1.5K$ to be only a few hundred Kelvins. We also note that the role of the feedback process in controlling electromigration is to prevent thermal runaway in the region of positive $\frac{dT_j}{dR_j}$. This region can be reduced by reducing the series resistance in the circuit, allowing controlled electromigration with a simple voltage ramp.

Chapter 5: Mesoscopic SNS Josephson Junctions

5.1: Introduction

Systems such as ferromagnets or superconductors that may go through a phase transition from a disordered to an ordered phase show many exotic physical behaviors in the ordered phase which is absent in the disordered one. Such systems may be treated phenomenologically after defining an order parameter, F, which shows how the order in the system varies. In the disordered state the order parameter vanishes showing complete lack of order and in the ordered state it takes nonzero values. In the case of ferromagnets F can be taken as the magnetization and in the case of superconductors as the effective Cooper pair density (density of paired of electrons). Typically such order parameters are continuous functions in space and their variations occur smoothly within the scale of the coherence length of the system. Therefore by placing an ordered and a disordered system in contact with one another, one may induce the spread of order from the ordered system into the disordered one. In the case of superconductivity the spread of superconducting order into normal metals that are in electrical contact with superconductors is called the proximity effect as discovered by H. Meissner [63].

At low temperatures for most superconductors the coherence length is a few hundred nanometers, and devices with these length scales can routinely be fabricated with present day experimental techniques. Therefore one may use this effect to fabricate exotic mesoscopic devices where superconductivity is induced in metals, such as gold, which lack intrinsic superconductivity. Such superconducting gold

mesoscopic devices have been fabricated and tested [59] where superconductivity is induced in a mesoscopic gold point contact, and from the shape of current-voltage curves the number of conduction channels and their individual transmission probabilities can be determined.

As we have explained in Chapter 3, gold nanogap junctions (either prepared via electromigration or via experimental techniques that are commonly used in preparing point contacts) are used extensively as a test bed for single molecule electronics. In principle one may produce gold nanogap junctions that are proximity-effect-induced superconductors and use these junctions as test beds for single molecule electronics. Such superconductor-molecule-superconductor (SMS) junctions can then be used to study a number of fundamental properties of the conductance of single molecules, such as the number of conductance channels the molecule has, the individual transmission probabilities of each conduction channel, and whether the molecule will carry supercurrent or not.

Chapter 5 and 6 summarize our efforts to construct SMS junctions and explore these issues. In Chapter 5, I will review the transport properties of superconductor-normal metal-superconductor (SNS) mesoscopic junctions. I will then explain in Chapter 6 the experimental approaches I took in fabricating mesoscopic SNS junction devices that would be suitable to use as a test bed for fabricating single molecule SMS junctions. I will explain the experimental difficulties we faced in device fabrication, and conclude with a discussion of what might be done to improve our experimental efforts.

5.2: Basic Properties of Superconductors

Superconductivity, in its manifestation of perfect conductivity, was discovered at Leiden by H. Kamerlingh Onnes in 1911 [64]. He observed that when pure mercury is cooled it looses its electrical resistance at a critical temperature, T_c .Below T_c the superconducting state can be destroyed at a high enough magnetic field, H_c, where metal enters to normal state.

In addition to the perfect conductivity, the second seminal property of superconductors, namely the perfect diamagnetism, was discovered by W. Meissner and R. Ochsenfeld [65]. They observed that when placed into magnetic field, or when the system becomes superconducting in magnetic field, superconductors expel magnetic flux. It is understood later that magnetic flux is completely expelled below H_c in type I superconductors which are mainly the pure elementary superconductors such as tin and aluminum. Type II superconductors (many of which are alloys) on the other hand allow partial penetration of magnetic flux in flux lines or vortices for $H_{c1} < H < H_{c2}$.

Superconductors show an energy gap, Δ, in their quasiparticle excitation spectrum. Establishment of the existence of an energy gap was one of the key steps in the understanding of the superconductivity in classical superconductors. First experimental indication of this gap came from the peculiar jump of the specific heat at the transition temperature [66, 67]. Later much direct evidence came from the measurements of electromagnetic absorption using infrared light [68, 69] and electron tunneling experiments pioneered by I. Giaever [70]. Furthermore the infrared

measurements gave indications of pairing of quasiparticles and they turned out to be one of the early verifications of the microscopic theory of superconductivity.

In 1950, before the appearance of the microscopic theory of superconductivity (The BCS theory, due to Bardeen, Cooper, and Schrieffer [71]), V. L. Ginzburg and L. D. Landau gave a phenomenological description of the superconducting state that is based on the Landau's theory of phase transitions. [72] Being phenomenological, G-L theory is based upon the generally observable features of superconductivity. The theory introduces a complex pseudo-wavefunction $\psi(r)$ as an order parameter that describes the superconducting state, and $|\psi(r)|^2$ is taken as to represent the density of superfluid. One may then expand the free energy of the superconductor in terms of $|\psi(r)|^2$ and $|\nabla\psi(r)|^2$ with expansion coefficients α and β and arrive at two differential equations for $\Psi(r)$ and the supercurrent J_s .

$$\alpha\psi + \beta|\psi|^2\psi + \frac{1}{2m^*}\left(\frac{\hbar}{i}\vec{\nabla} - \frac{e^*}{c}\vec{A}\right)^2\psi = 0 \qquad \text{Equation 5-1}$$

$$\vec{J}_s = \frac{e^*\hbar}{2m^*i}\left(\psi^*\vec{\nabla}\psi - \psi\vec{\nabla}\psi^*\right) - \frac{e^{*2}}{m^*c}\psi^*\psi\vec{A} \qquad \text{Equation 5-2}$$

Where c is the speed of light, e^* is the effective electronic charge, $\hbar$ is Planck's constant, m^* the effective electronic mass, $\vec{A}$ the vector potential, $\vec{J}$ the supercurrent density. G-L theory introduces an important length scale called the Ginzburg-Landau

coherence length, ξ, given by $\xi^2_{GL}(T) = \frac{\hbar^2}{2m^* |\alpha(T)|}$. G-L coherence length is the characteristic distance over which the spatial changes on $\psi(r)$ may occur and the order parameter may vary. Ginzburg-Landau theory is very useful in describing the situations where there is spatial inhomogeneity and the order parameter varies, such as superconductors in a magnetic field or the penetration of order parameter into other metals as it occurs in some proximity effect configurations. But it concentrates only on the superconducting electrons rather than the excitations. Therefore to analyze mesoscopic Superconductor-Normal Metal-Superconductor (SNS) junctions one generally takes a different approach using the non-local form of BCS theory.

Before the analysis of mesoscopic SNS junctions in section 5.4, I will note main features of BCS theory since most of the main concepts like the existence of quasiparticle excitations, the energy gap etc are retained in non-local form of BCS theory as well. BCS theory was published in 1957 by Bardeen, Cooper and Schrieffer [71]. BCS theory is based on the idea that in superconductors, electrons near the Fermi level experiences a mutually attractive force and this attractive force gives rise to a new form of quantum state at temperatures below T_c. In this new quantum state, some portion of electrons near the Fermi level are bound together in pairs which are called Cooper pairs. In classical superconductors such as lead, tin and aluminum, the Cooper pairs' size, the coherence length, is several hundred nanometers, i.e. for aluminum the coherence length is approximately 1600 nm, for tin 230 nm and for lead 83 nm [73], and the Cooper pairs strongly overlap in space. The external center of motion of pairs is coupled together and each pair is in the same state. The paired

state, like the Fermi sea, still has excitations which are electron-like for momenta just outside the Fermi surface and hole-like for momenta just inside (In superconductivity, the hole state refers to an empty state below the Fermi level). These single particle excitations are still fermions, with a Fermi distribution at temperature T, but in some respects such as their dispersion relation, they differ from ordinary electron and hole excitations.

To break up a pair, one need to supply energy that amounts at least 2Δ and that produces two quasiparticle excitations in the superconductor, therefore the excitation energy, E_k, cannot be less than Δ.

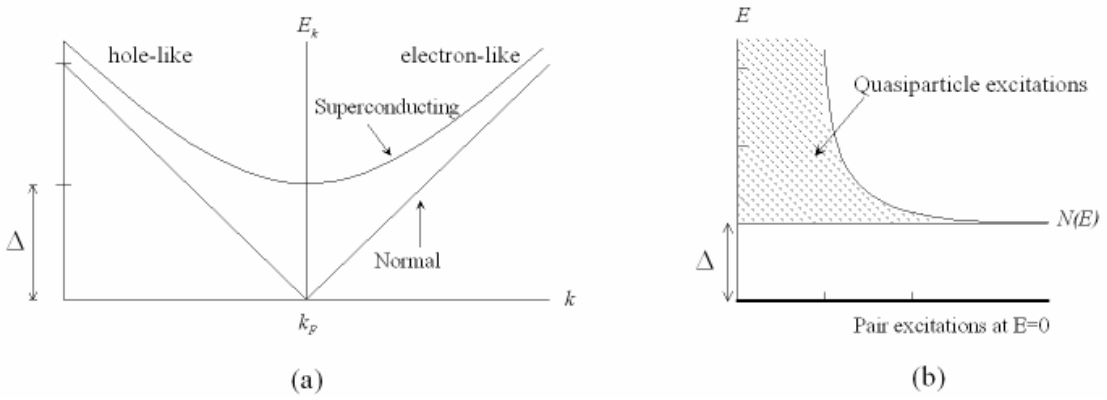

Figure 5-1. (a) Shows difference in the dispersion relation of normal and superconducting metals. (b) Shows the density of states of superconductor. There are no states for quasiparticles in the energy gap. Energy of Cooper pairs is measured from the chemical potential. Adapted from reference [73].

We may add electrons to the superconductor in two ways. One may add electrons as bound pairs with energy 2μ, or one may add a single electron by producing a quasielectron excitation. There exist no states for the quasielectron excitations for energies below the gap, so to add an electron to the superconducting system from outside, one need to supply it with energy at least the value of the gap.

Although the BCS theory revolutionized the understanding of the superconductivity, in its original form it can only handle translationally invariant superconductors containing excitations of definite momentum. Therefore to analyze the superconducting-normal metal-superconducting junctions in mesoscopic limit, the nonlocal form of the BCS theory is employed.

5.3: Josephson Effect and SNS Josephson Junctions

Josephson Effect was predicted theoretically by B.D. Josephson in 1962 [74]. Although his predictions were originally for tunnel junctions it turned out that they applied to a wider class of structures including SNS junctions.

Figure 5-2. An SNS junction. Two superconductors (SC_1 and SC_2) are weakly linked via normal metal.

The Josephson Effect is seen in two weakly interacting superconductors, that is two superconductors close enough that coherent Cooper pairs may travel between the two. The weak link that connects the two superconductors might be a tunnel barrier (like Nb-AlO_x-Nb), a superconducting constriction, or a normal metal. Current through the weak link is carried by coherent interaction of electrons which is tunneling for a tunnel barrier and coherent Andreev reflection at the two interfaces for an SNS junction. (We will explain the mechanism of Andreev Reflection on section 5.5). The resulting structure is called a Josephson Junction.

The Josephson Effect is one of the macroscopic quantum phenomena resulting from superconductivity. One can separate the effect in two parts called as DC and AC Josephson effect. The DC Josephson Effect states that two superconducting electrodes may contain a component of supercurrent which does not depend on the voltage across the electrodes, but rather the phase difference between the two superconductors. Experimentally this states that one can push current through the weak contact (up to a limit namely $-I_c \le I_s \le I_c$) without building up a voltage gradient. The critical current, I_c, depends on the geometry of contact, temperature, the material of the contact and other factors.

$$I_s = I_c \sin\left(\theta_1 - \theta_2\right) \qquad \text{Equation 5-3}$$

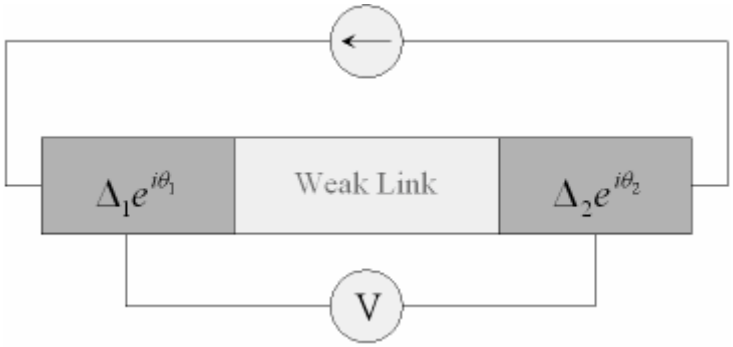

Figure 5-3. DC Josephson Effect.

AC Josephson Effect states that, if a constant voltage is applied between the two weakly contacted superconductors, then the phase difference evolves with time and produces an AC supercurrent.

$$\frac{d\left(\theta_1-\theta_2\right)}{dt}=\frac{2eV}{\hbar} \qquad \text{Equation 5-4}$$

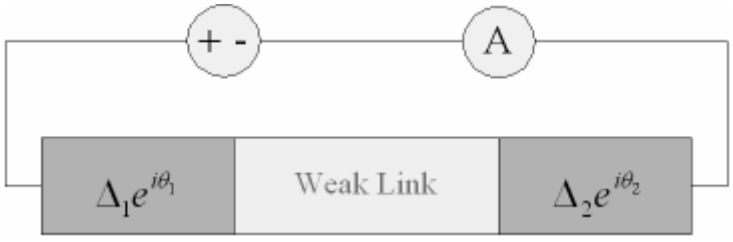

Figure 5-4. AC Josephson Effect

The supercurrent in SNS weak links flows along a conducting material. If we have an SNS sandwich junction (or similar constrictions), the supercurrent flows through this junction due to the proximity effect. In the normal metal there arises a nonzero order parameter, Δ, which exponentially decreases within the metal over a distance of the order of "normal coherence length" or "the decay length" ξ_n. ξ_n is given by $\xi_n = \xi_n^{\,0} = \dfrac{\hbar v_F}{2\pi k_B T}$ in the clean limit that is when the electronic mean free path, ℓ, is greater than $\xi_n^{\,0}$. In the dirty limit , $\ell \ll \xi_n^{\,0}$, where the electronic motion is diffusive, than ξ_n becomes $\left(\dfrac{1}{3}\xi_n^{\,0}\ell\right)$. On the other hand, the value of Δ in the superconductor becomes less than the equilibrium value in the superconductor over distances on the order of coherence length in the superconductor.

Transport properties of such junctions are well studied for various geometries and the temperature dependence of the critical current is calculated. The interested reader may see the review by K.K. Likharev [75]. For my purpose (to use such constrictions as test beds for single molecule electronics) I tried to build a mesoscopic SNS point contact junctions which I explain below.

5.4: Mesoscopic SNS Junctions

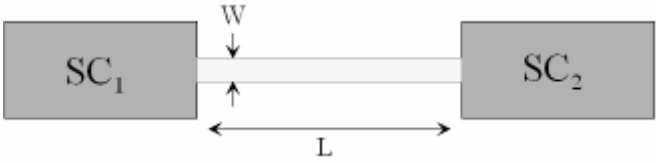

Figure 5-5. Mesoscopic SNS junction. Both the width and the length of the normal region are much smaller than the coherence length of superconductor.

Mesoscopic SNS junctions, as distinguished from other junctions such as SNS sandwich junctions, refer to the class of junctions where both the length of the junction, L, and the width of the junction, W, are much smaller than the coherence length of the superconductor i.e. $W, L \ll \xi_0$. A point contact or a microbridge between two superconductors belongs in general to this class of junctions. In the theoretical analysis of these junctions the suppression of the $\Delta(\vec{r})$ approaching the junction can be neglected and one generally uses a step function model:

$$\Delta(\vec{r}) = \begin{cases} \Delta_0 e^{i\theta_1/2} & \text{if } x < 0 \\ 0 & \text{if } 0 < x < L \\ \Delta_0 e^{-i\theta_2/2} & \text{if } x > L \end{cases} \qquad \text{Equation 5-5}$$

where ϕ is the phase difference between two superconducting electrodes (assumed as the same superconductor here) and x is the coordinate along the junction. The above condition holds when the width of the junction is small compared to the coherence length, since the non-uniformities in $\Delta(\vec{r})$ extend only to distances of order W from the junction. This is because of the geometrical dilution of the influence of the narrow junction in the wide superconductor. Since the non-uniformities on length scales $\ll \xi$ don't affect the quasiparticle dynamics these can be neglected and the step function model holds. In the literature above approximation is referred as "rigid boundary conditions" [75]. Experimentally, to satisfy the above requirement, one needs to prepare devices where the junction has size $W, L \sim 100$ nm

For supercurrent flow in the junction the electron flow through the junction should be phase coherent that is the electrons should move in the junction without any phase breaking scattering. Therefore experimentally one needs "clean" deposition of the metals containing no magnetic impurity which is the main phase breaking scattering mechanism at low temperatures.

In addition to above the interface between superconductor and the normal metal should be in good electrical contact. Experimentally this requires either to deposit both metals without breaking the vacuum, or if the fabrication requires two steps of lithography, to clean the surfaces via plasma etching or ion milling and without breaking the vacuum to deposit the second metal. I will point out these requirements in Chapter 6 again.

5.5: Transport Properties of Mesoscopic SNS junctions

I-V characteristics of superconducting point contacts with finite conductance in the normal state can be calculated by adopting a non-perturbative approach using the Bogolibov-de Gennes (BdeG) equations. BdeG equations describe the quasiparticle excitations (which consist of electron and hole like states) in non-uniform superconductors. BdeG equations could be written as [76]

$$\begin{aligned} Eu(\vec{r},E) &= \left[\frac{\hbar^2\vec{\nabla}^2}{2m} + U(\vec{r}) - E_F\right]u(\vec{r},E) + \Delta(\vec{r})\upsilon(\vec{r},E) \\ E\upsilon(\vec{r},E) &= \left[\frac{\hbar^2\vec{\nabla}^2}{2m} + U(\vec{r}) - E_F\right]\upsilon(\vec{r},E) + \Delta^*(\vec{r})u(\vec{r},E) \end{aligned} \qquad \text{Equation 5-6}$$

Here $U(\vec{r})$ and $\Delta(\vec{r})$ are the effective potentials which are determined self consistently, E is the excitation energy and $u(\vec{r},E)$ and $\upsilon(\vec{r},E)$ are the amplitudes of electron-like and hole-like states. When $\Delta(\vec{r}) = 0$ the two equations become uncoupled and we get the normal state excitations with no gap at Fermi level, when $\Delta(\vec{r})$ and the potential are translationally invariant that is $\Delta(\vec{r}) = \Delta_0$ and $U(\vec{r}) = U$, the solution can be made in terms of plane waves $u(\vec{r}) = u_{\vec{k}}e^{i\vec{k}.\vec{r}}$ and $\upsilon(\vec{r}) = \upsilon_{\vec{k}}e^{i\vec{k}.\vec{r}}$, and we recover the usual dispersion relations for the quasiparticle excitations in BCS theory i.e. $E_{\vec{k}} = \sqrt{\left(\varepsilon_{\vec{k}} - E_F\right)^2 + {\Delta_0}^2}$ where $\varepsilon_k = {(\hbar k)^2}/{2m}$. Inverting the dispersion relation, one can get $\hbar k^{\pm}$ in terms of the energy of the excitations (Equation 5-7) where excitations with k^+ are the quasielectrons and with k^- are the quasiholes.

$$\hbar k^{\pm} = \sqrt{2m\left[E_F \pm \sqrt{E^2 - \Delta^2}\right]} \qquad \text{Equation 5-7}$$

As we mentioned in section 5.3, Andreev reflection is the main mechanism for the current flow in an SNS junction by converting electron current in the normal metal to supercurrent in the superconductor. Andreev reflection can be understood using the BdeG equations as follows.

Assuming (for simplicity) a single channel connecting both superconductors along the coordinate x and also assuming rigid boundary conditions at the interface between superconductor and normal metal (as we have explained in section 5.4), the wavefunctions on both sides of the interface for an electron with energy E can be written as

$$\begin{aligned}
\psi(x,E) &= \begin{pmatrix}1\\0\end{pmatrix} e^{iq^+x} + r_{eh}\begin{pmatrix}0\\1\end{pmatrix} e^{iq^-x} + r_{ee}\begin{pmatrix}1\\0\end{pmatrix} e^{-iq^+x} \quad \text{for } x<0 \\
\psi(x,E) &= t_{ee}\begin{pmatrix}u(E)\\\upsilon(E)\end{pmatrix} e^{ik^+x} + t_{eh}\begin{pmatrix}\upsilon(E)\\u(E)\end{pmatrix} e^{-ik^-x} \quad \text{for } x<0
\end{aligned} \qquad \text{Equation 5-8}$$

Here $\hbar q^{\pm} = \sqrt{2m(E_F \pm E)}$ are the momenta of electron and hole excitations in the normal metal and the two elements in the column vector represents the electron and hole components of the quasiparticle excitation in the superconductor. The coefficients $r_{eh}, r_{ee}, t_{ee}, t_{eh}$ represent the four processes that may occur to the incident electron in the interface, namely reflection of the incident electron as a hole,

reflection as an electron, transmission as an electron and transmission as a hole. They are determined from the boundary condition that both the electron wavefunction and its derivative should be continuous at the interface.

When there is no electrostatic potential mismatch between the normal metal and the superconductor, that is the case of a perfect interface, calculation leads to $r_{ee} = t_{eh} = 0$ and $r_{eh}(E) = \frac{\upsilon(E)}{u(E)}$ where r_{eh} is the probability amplitude for an electron to reflect as a hole or to make an Andreev reflection. In the case of a BCS superconductor, if the energy of the incident superconductor is less than the superconducting gap r_{eh} can be calculated as $r_{eh} = \exp\left[-i \arccos\left(E/\Delta\right)\right]$ and for energy values greater than the gap r_{eh} decays exponentially. So the electron incident from the normal side reflects as a hole and in the whole process two electrons are added from the normal metal to superconductor as a cooper pair. This is the basic mechanism for the conversion of normal current to supercurrent in the normal metal-superconductor interface as first pointed out by Andreev [77].

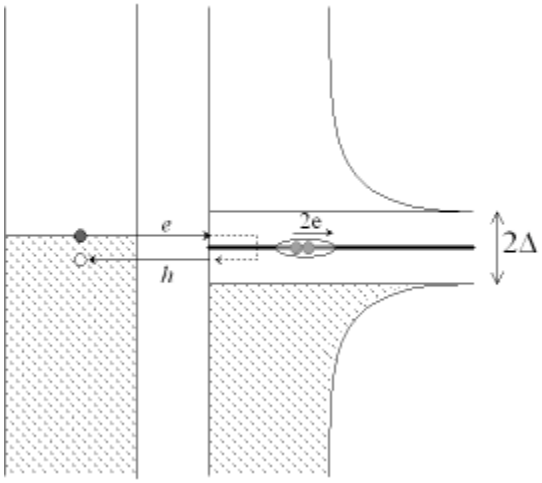

Figure 5-6. Andreev reflection of an electron as a hole from the superconductor-normal metal interface. As a result of the reflection, two electrons are transferred from the normal metal to the superconductor as a Cooper pair. Adapted from reference [41].

An imperfect interface can be analyzed by representing the electron potential in the interface with a delta function potential $U(x) = H\delta(x)$ [78]. For energy values $E < \Delta$, r_{eh} is calculated as $|r_{eh}|^2 = \dfrac{\Delta^2}{E^2 + (\Delta^2 - E^2)\left(1 + 2\left(\dfrac{k_F H}{2E_F}\right)\right)^2}$. Using r_{eh} then one can calculate the linear conductance of a normal-superconductor junction [79]. For a single conduction channel at zero temperature the conductance is given by $G_{NS} = \dfrac{4e^2}{h}|r_{eh}(0)|^2$, i.e. twice the value of the Landauer formula reflecting the fact that there are two electrons transmitted through the interface as a result of the Andreev reflection.

The above result can be generalized for the multi channel case [79] $G_{NS} = \frac{4e^2}{h} \sum_n \frac{\tau_n^{\,2}}{\left(2-\tau_n\right)^2}$ where τ_n is the transmission probability of the *n*th conduction channel. An important point about above result is that the normal conduction channels are not mixed with Andreev reflection process. That is, the electron incident to the interface in the *n*th conduction channel reflects back as a hole in the same channel. This property is very useful in determining the number of conductance modes participating in conduction.

Similar to tunneling junctions, mesoscopic SNS junctions can carry supercurrent. In the normal metal channel (of length *L*) between two superconducting electrodes, an electron with $E < \Delta$ will make an infinite series of Andreev reflections, reflecting back and forth as electron and hole at the interfaces. This resonance condition gives rise to the energy values $E = \Delta \cos\left\{\frac{\phi}{2} - \frac{k_F L}{2}\left(E \big/ E_F\right) - n\pi\right\}$ inside the channel, where ϕ is the phase difference between the electrodes. The solutions of above equation are the bound states inside the channel and they are known as Andreev-Kulik states [80].

In the short junction limit where $L \ll \xi_0$, there are only two states occurring in the energy values $E = \pm\Delta \cos\left\{\frac{\phi}{2}\right\}$ [81]. These two states are responsible for carrying the Josephson current in the SNS junction. The current for *N* conductance channels can be calculated as [79]

$$I(\phi) = \frac{Ne\Delta}{\hbar}\sin\left(\frac{\phi}{2}\right)\tanh\left(\frac{E}{2k_BT}\right)$$ Equation 5-9

The case of the arbitrary normal transmission, τ, can also be analyzed using BdeG equations. In this case in the short junction limit there are again two bound states at energy values $E = \pm\Delta\sqrt{1-\tau\sin^2\left(\frac{\phi}{2}\right)}$ and the supercurrent is given by [79, 82]

$$I(\phi) = \frac{e\tau\Delta}{2\hbar}\frac{\sin(\phi)}{\sqrt{1-\tau\sin^2\left(\frac{\phi}{2}\right)}}\tanh\left(\frac{E}{2k_BT}\right)$$ Equation 5-10

In voltage biased junctions the total current through the contact is [83, 84] $I(V,t) = \sum_n I_n(V)e^{in\omega_o t} = I_o + 2\sum_{m>0}\mathrm{Re}(I_m)\cos(m\omega_o t) - 2\sum_{m>0}\mathrm{Im}(I_m)\sin(m\omega_o t)$. Here the dc component of the current, I_o, is the experimentally more accessible part and the part of interest for determining the number of conductance channels.

In I-V curves of the junction, along with the supercurrent at zero voltage, for voltage biases less than $2\Delta/e$ one observes nonlinear behavior consisting of sharp current steps at voltage values $V = \frac{2\Delta}{ne}$. These current steps are called the subharmonic gap structure or subgap structure (SGS) [41, 85, 86]. In SGS, $n = 1$ corresponds to single quasiparticle transport between superconducting electrodes. The phenomenon of higher *n* values is called Multiple Andreev Reflections (MAR).

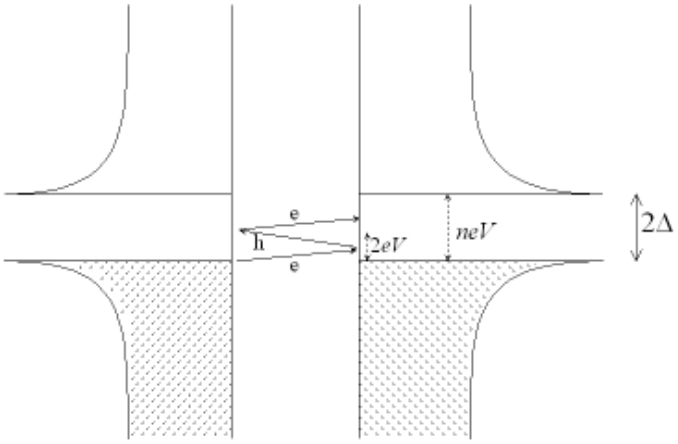

Figure 5-7. Multiple Andreev Reflection of quasiparticles. At each reflection electron (hole) reflects as a hole (electron) and each time the quasiparticle travels the normal region, it gains an energy amount eV. Adapted from reference [41].

For voltage values less than 2Δ, a quasiparticle can contribute to current via making multiple Andreev reflections between the superconducting electrodes to reach the states above the gap value by gaining energy amount eV each time it crosses the normal region. For $n=2$ we observe current increase at the threshold $eV=\Delta$, showing that the electron (hole) travels the normal region from one SC electrode, gains energy by eV, it Andreev reflects back as a hole (electron) travels the normal region again and gains another eV and scatters to a state at $2eV$. Similarly we observe another current increase at threshold $\frac{2\Delta}{3}$ via two Andreev Reflections and so on for higher orders. The magnitude of the current depends on the number of reflections as well since each time the quasiparticle travels the normal channel it is

more probable that it will scatter in the channel and not contribute to current. Current increase due to n^{th} current step can be calculated at low transmission [87] $\delta I_o^{(n)} = \frac{e\Delta\tau^n}{\hbar}\left(\frac{2n}{4^{2n-1}}\right)\left(\frac{n^n}{n!}\right)^2$. For higher transmission values close to one the SGS structure starts to wash out.

For N independent channels the total current can be written as a sum of individual channels $I(V) = \sum_{i=1}^{N} i(V, \tau_i)$ (since the Andreev reflection does not mix the channels). The above result is very important because the analysis of the subgap structure permits one to obtain information about the conductance modes. Although one can be sure that there is more than one channel contributing to the conductance for $G \geq G_o$, we cannot be sure about how many modes are contributing for the case $G \leq G_o$. It is a possibility that several poorly transmitted channels may add to give a total transmission less than one. By fitting to experimental data, the number of conductance channels as well as their transmission probabilities can be obtained. The above property of mesoscopic superconducting junctions can be used in molecular electronics by measuring conductance properties of individual molecules in between superconducting leads so that the number of conducting channels i.e. how many molecules are participating in conduction as well as their transmission probabilities can be measured.

Chapter 6: Preparing Mesoscopic SNS Junctions as Electrodes

6.1: Introduction

Single Molecule Electronics research concentrates largely on the possibility of using single molecules as active electronics components such as a rectifier, diode or a transistor. Such drive mainly comes from the expected end of the silicon era in electronics. Achieving this goal requires understanding their electronic properties and finding ways to stably anchor them to the interconnecting leads. Many research groups have made an effort to understand the conductance properties of single molecules both due to the above industrial drive and also just due to the intellectual curiosity to understand the physics and chemistry of molecular conduction. The experiments are done mostly via producing a nanogap either via an STM, via using a MCBJ or via electromigration. But in many of these experiments it is not possible to be sure how many molecules are conducting and how many channels per molecule are participating in the conduction. There are also questions that arise from the academic curiosity such as whether a molecule will be able to carry supercurrent or not, or if it does whether this current can be understood with known theories.

To possibly answer these questions, I tried to fabricate a mesoscopic SNS junction where the mesoscopic normal constriction is made out of gold (both due to easy electromigration and due to the fact that most molecules tested are anchored to gold via sulfur bonds). Our aim was, after being sure that we can induce superconductivity in the normal layer, to use the junction produced in the normal

constriction (via electromigration) as a test bed for molecules. In this chapter I will explain the experimental approaches I took for fabrication and the difficulties I faced, and I will conclude with what might be done to improve our experimental efforts.

6.2: Device Fabrication and Difficulties Faced

6.2.1: Thin Au lines and Nb contacts

As I have explained in section 5-4, to build a mesoscopic SNS junction one needs to prepare the normal constriction of the device on the order of 100 nanometers. To fabricate devices in such small dimensions, EBL is commonly used (see i.e. section 4-2). I first attempted to fabricate our devices using two steps of EBL where in the first step I fabricated the gold lines, a wheel-shaped test pattern (used to diagnose problems in EBL), and alignment markers, typically with 20 nm of gold metallization with no sticking layer (See figure 6-1). In the second step I fabricated the leads and the contact pads using RF sputtering of Nb typically 70-80 nm of metallization.

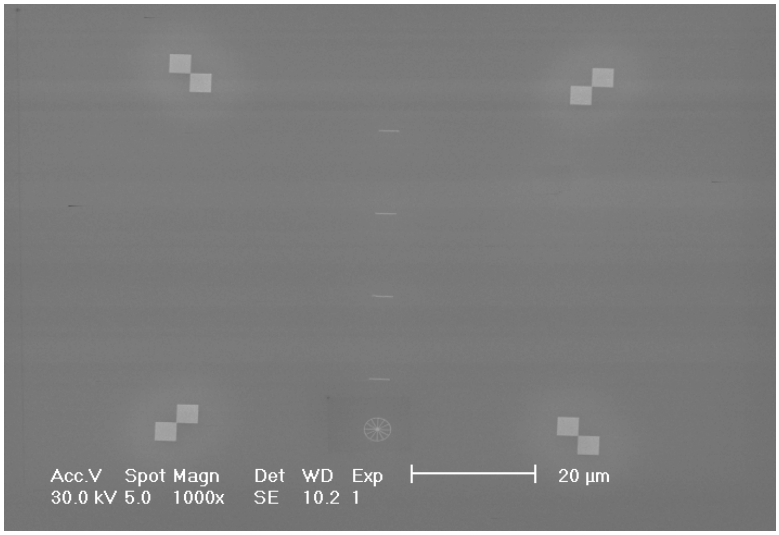

Figure 6-1. Metallization for thin gold lines. The alignment markers are prepared for the second step of lithography and the wheel pattern is for the check of astigmatism during lithography process.

It is well known that metal deposition using sputtering deposits more energy to the substrate compared to both electron beam deposition of metals and deposition via thermal evaporation. Although thermal evaporation is the most commonly used method of deposition of metals, it is extremely difficult to deposit refractory metals such as Nb via this method. Electron beam deposition can be used as well in some cases, but the most common approach (and the experimental capability that I had available) is to deposit Nb via sputtering. Unfortunately, in my samples sputtering resulted in melting of the thin gold lines I prepared in the first step of metallization.

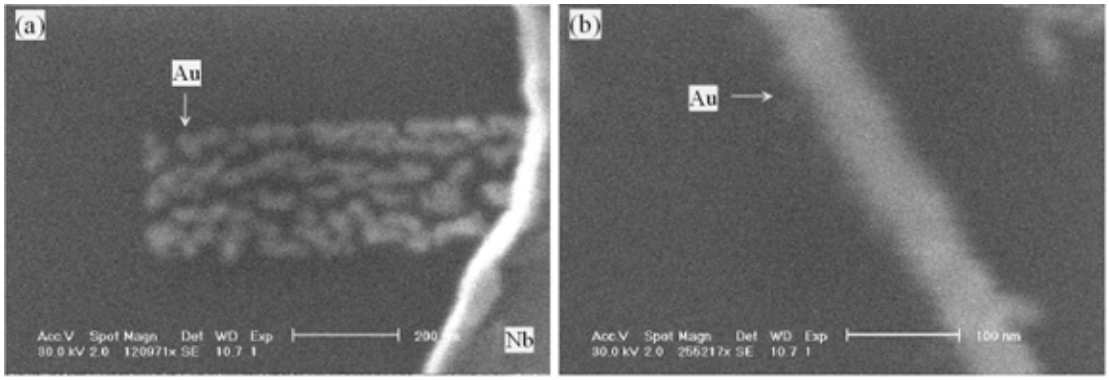

Figure 6-2. Melting of Au metallization due to Nb deposition (a) Shows the thin gold line after the deposition of Nb contacts (b) Shows a thin gold line from the wheel pattern where Nb deposition is made on a resist layer covering the gold line. Scale bar in (a) shows 200 nm length scale and in (b) shows 100 nm length scale.

Figure 6-2 (a) shows an SEM micrograph of a device after Nb deposition on the surface and 6-2 (b) shows an SEM micrograph of a line from the wheel pattern after Nb deposition where the unexposed resist shields the gold line from Nb metallization. From the SEM micrographs I conclude that there is local heating due to Nb deposition and this causes melting of gold lines. One solution to this problem might be to cool the sample before and during Nb deposition, such as using a cold finger. Unfortunately the deposition chamber I used was not built with such capability and it was not possible to make such an addition to the sample stage. Therefore I decided to use a wetting layer for making gold less mobile on the silicon dioxide surface. I knew that this approach would make preparing the nanogap junction via electromigration harder, but I still wanted to see whether it would stop the problem or not. The most widely used wetting layer for gold is chromium, but I rejected this due to its magnetic properties (which would be incompatible with superconductivity). I

instead used titanium (Ti) as a wetting layer for gold. Although this approach worked in some samples, it failed in the majority of cases where I still observed local melting of the gold lines. Figure 6-3 shows a sample in which this approach barely worked. I still wanted to test samples for which Nb deposition did not melt the gold to see whether superconductivity would be induced in them or not. I cooled my samples down to 1.2 K using a ^{4}He cryostat (monitoring resistance as I lowered the temperature) but I did not observe any clear effect of a superconducting transition in the gold constriction possibly due to electrically dirty contacts (as explained below) or due to magnetic impurities in the gold metallization (as explained in section 6.2.2).

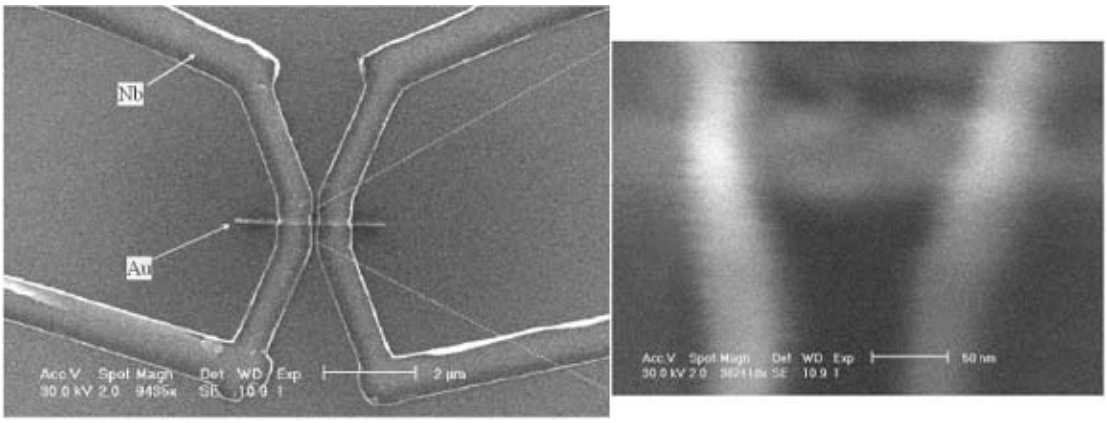

Figure 6-3. SEM micrograph of a sample with thin Au lines and Nb contacts.

As I have explained in Section 5-4, for superconductivity to be induced in normal metal the superconducting metal should be in good electrical contact with the normal

metal such that the incoming electrons are Andreev reflected. In metallization which requires two different steps of lithography this is typically achieved by cleaning the surface of first layer either with oxygen plasma or ion milling before the deposition of the second. The sputtering chamber I used did not have the capability for oxygen plasma or ion milling, so I was unable to perform any cleaning step before the second metallization. Thus I considered that electrically "dirty" contacts between the normal and the superconducting layers were the likely cause of the lack of observed supercurrent through the gold bridge. Therefore I decided to change our sample fabrication procedure and decided instead to use aluminum as the superconducting metal and to use a thermal deposition chamber which would allow both metallization to be performed in one process without breaking vacuum.

6.2.2: Shadow evaporation of gold and aluminum contacts

As a second method I tried to fabricate our samples using a "resist bridge" technique followed by evaporation of metals at different angles. First I "shadow evaporated" the gold (deposited it from two different angles to the bridge) and then without breaking the vacuum I deposited the aluminum layer at normal incidence to the sample i.e. See figure 6-4.

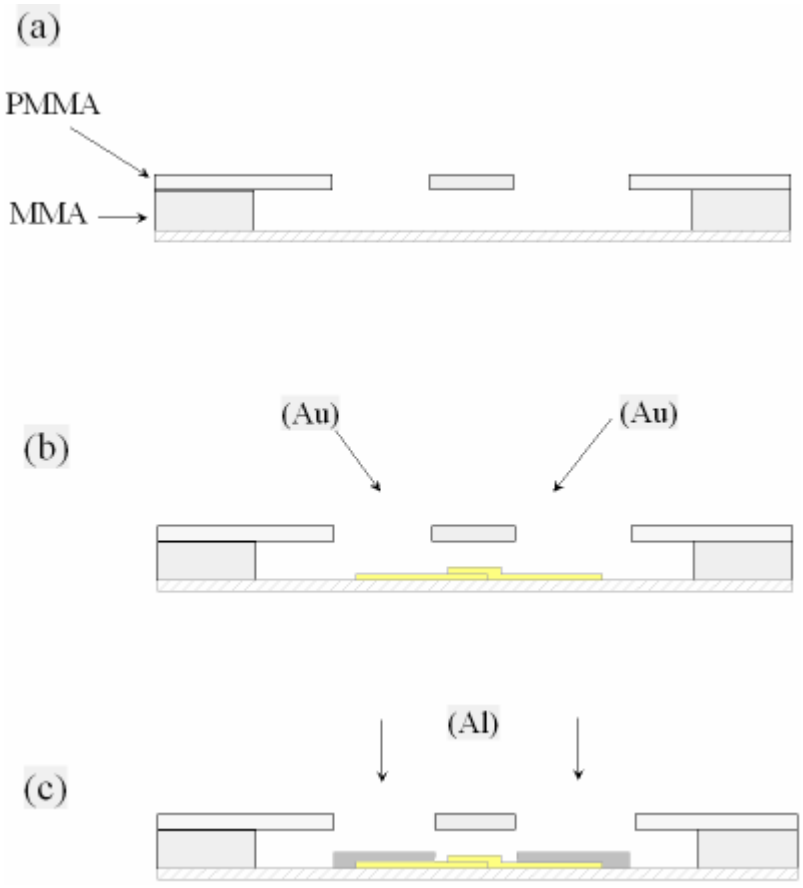

Figure 6-4. Shadow evaporation of gold and aluminum contacts. (a) Shows the resist bridge (side view) after development (b) Shows the shadow evaporation of gold from two different angles to the substrate (c) Shows the evaporation of aluminum from direct angle to the substrate.

As I have explained in section 3-2 one can produce resist bridges out of a bilayer electron beam resist via selectively developing P(MMA-MAA) layer with Isopropanol (IPA) after an initial MIBK:IPA development. My idea was that by not breaking the vacuum between two metal depositions, I would get a "clean" electrical contact between the two metallization layers. I used a thermal deposition chamber (deposition chamber in the Center for Superconductivity Research) that has a sample stage where one can adjust the tilt angle. I first deposited two gold layers (typically 15

nm each) from two different angles (by tilting the sample stage) to form a continuous gold metallization and then I deposited aluminum (typically 70-80 nm) with sample being perpendicular to the source. Figure 6-5 shows an SEM micrograph of a device as prepared using this technique.

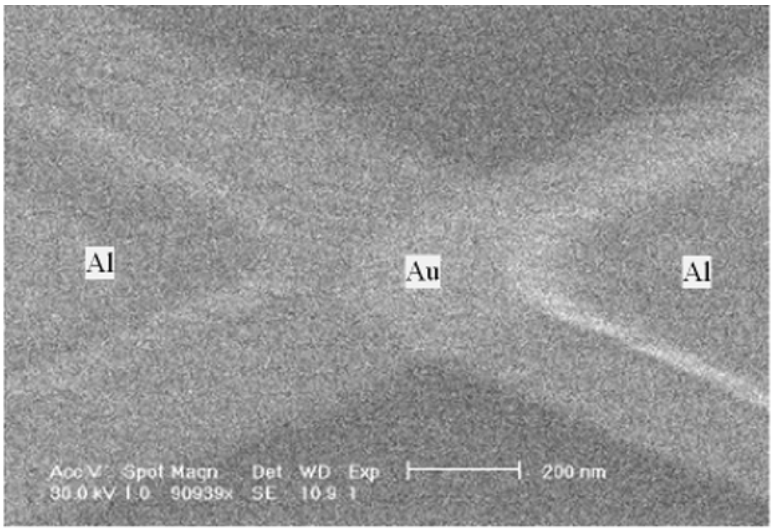

Figure 6-5. An Au-Al device fabricated via shadow deposition of gold using a resist bridge.

The device in Figure 6-5 would seem to satisfy all the requirements for observing supercurrent through the gold bridge. However, along with the clean contacts between two metals another requirement which needs to be satisfied is to be able to deposit the metals without having magnetic impurities. Magnetic impurities cause phase-breaking scattering and destroy the superconducting correlations in the normal layer. When I cooled my samples and measured their temperature-dependent

resistance, I observed the well-known Kondo effect, the signature of magnetic impurities in a non-magnetic host metal, in our gold metallization. Figure 6-6 shows the resistance vs. temperature curves (Obtained via a standard 4-probe current reversal technique) of the raw gold material used in deposition [Figure 6-6 (a)] and the metallization done in the deposition chamber [Figure 6-6 (b)].

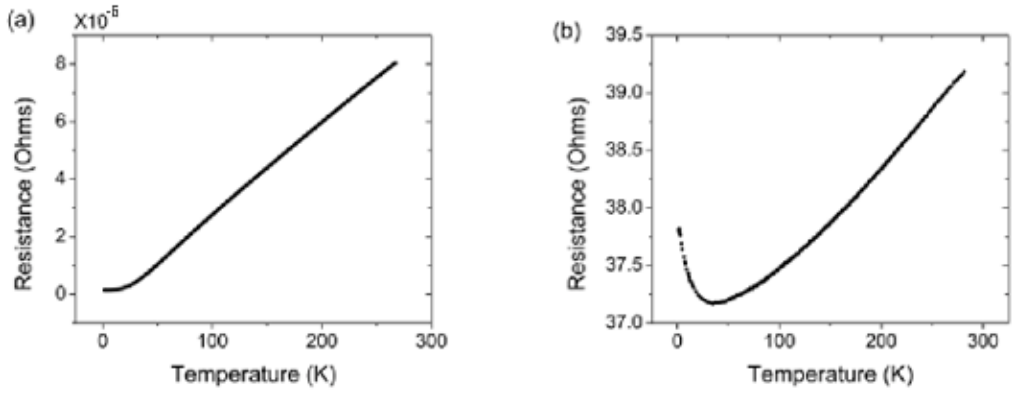

Figure 6-6. Kondo effect in Au deposition. (a) Resistance vs. temperature curve of the Au material used in metal evaporation (b) Resistance vs. temperature of the deposited material.

Here the increasing resistivity with decreasing temperature is due to the Kondo effect [88] and indicates the presence of magnetic impurities. The possible cause of this is the high contamination of the chamber with chromium which is used extensively in this chamber as a wetting layer for gold. I tried to clean the current leads to the evaporation sources, but this didn't solve the problem and I still observed the Kondo effect in my samples. Since there were no other chambers that I would be

able to use for this technique, I decided to change my sample fabrication approach again.

6.2.3: Electron beam deposited thin Au lines – Aluminum contacts

As a third approach, I decided to return to two steps of electron beam lithography where I first prepare thin gold lines via e-beam evaporation (which I tested and which showed no signature of the Kondo effect) and later prepare superconducting contacts out of aluminum in the second step where, before aluminum deposition, I clean the gold surface with ion milling. An SEM micrograph of a device prepared with such a technique is shown in Figure 6-7.

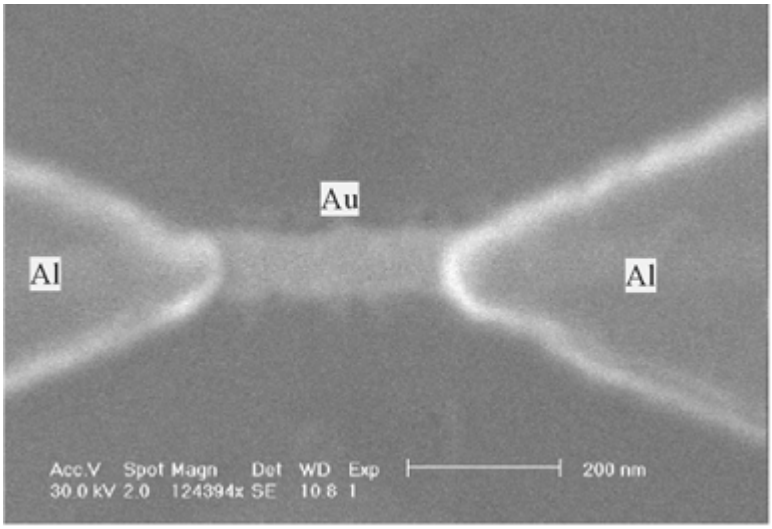

Figure 6-7. SEM micrograph of a device where the Au line is deposited via electron beam evaporation and superconducting Al contacts are deposited in second step metallization after cleaning the surface with ion beam milling

When I prepared the superconducting metallization out of aluminum which has relatively low temperature of superconducting transition (~1.2 K), I had to use our ^{3}He cryostat (Desert Cryogenics) which can achieve temperatures as low as 280 millikelvins. Preparing the sample for measurement in this instrument requires pumping the vacuum space ("can") down to low (~10^{-6} Torr) pressure to be sure that there is no leak into the vacuum space. This is done to be sure that there is no leak in the seal of the vacuum can since it is immersed into liquid ^{4}He which is superfluid and might easily leak into the can if there is a leak. Such a leak both stops reaching the base temperature and might be dangerous since, upon removal fro the bath, the trapped liquid ^{4}He would expand suddenly and cause the ejection of the can which could damage both the instrument and possibly the user. In my lab pumping is accomplished using a turbo pump assembly and generally by pumping on the vacuum can overnight.

When I prepared my samples for measurement in ^{3}He cryostat I first tested the electrical conduction of my devices before pumping the vacuum can. When I was sure that my devices were conducting, I electrically grounded the lines and connected the pump line [which is electrically isolated from the cryostat assembly during the pumping by using an insulating (plastic) vacuum connection]. After pumping overnight I tested my devices again, and if they were still conducting I immersed the cryostat into the ^{4}He bath to lower the temperature and start to take the measurements.

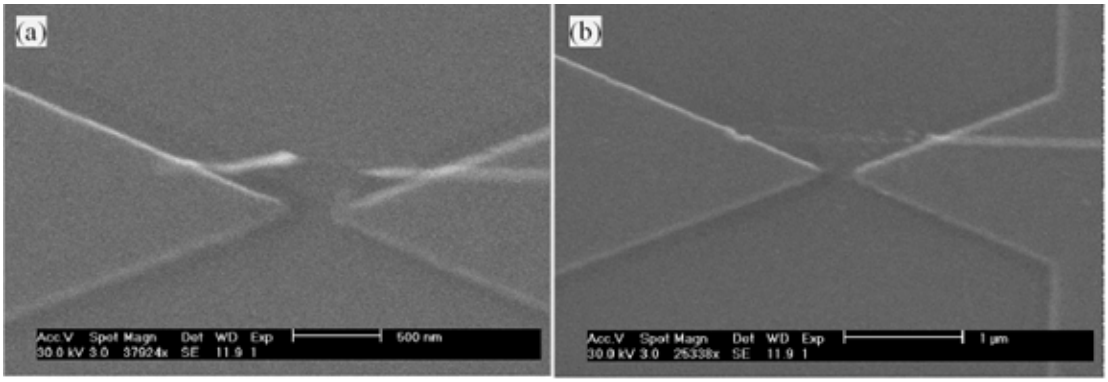

Figure 6-8. Post-Mortem SEM micrographs of two devices after pumping the vacuum space. Both devices were conducting before pumping the vacuum space. Scale bar in (a) shows 500 nm length scale and in (b) 1 micrometer length scale.

When I prepared my samples by this method for measurements, I observed that during the pumping on the can open circuits were produced via breaking the lines or by totally destroying them. [See i.e. post-mortem SEM micrographs Figure 6-8 (a) and 6-8 (b) taken after pumping].I concluded that this is because the gold lines are not adhering well to the SiO_2 surface and the mechanical vibration from turbo pump is causing the breaking of the lines. To overcome this I could have prepared gold lines by a nonmagnetic adhesion layer such as Ti, but this in turn would impede the electromigration of gold lines for preparing nanogap junctions so I rejected this approach. Cleaning the SiO_2 surface via oxygen plasma before gold deposition would be another possible solution, but I didn't have access to such an instrument. Another solution would be to identify the problem caused by the turbo pump (perhaps replacing by a diffusion pump or other quiet pumping system).

6.3: Conclusion

Although I put a considerable amount of effort into this project, I was unsuccessful in fabricating the samples that would be useful for my experiments. Most of my problems were due to not having access to the right sample fabrication instruments. For example, a thermal deposition chambers free of magnetic contamination, an electron beam deposition instrument with a tilting stage, or a deposition chamber with an oxygen plasma cleaning facility would have helped greatly. One can also perform this experiment using MCBJ technique or STM as well but this would require first developing expertise on those experimental techniques. Therefore I had to channel my experimental efforts to other questions/experiments in my field that might give more fruitful results.

Chapter 7: Palladium Nanojunctions as Hydrogen Sensors

7.1: Introduction

Hydrogen gas is widespread use in many industries such as chemical, metallurgical, and electronics. It is thought to be one of the clean energy sources for the future and is being used in hydrogen-powered vehicles. An important technological hurdle during production, storage, and transportation of hydrogen is that the leaks should be monitored continuously since when mixed with air above 4.65 % in volume, hydrogen gas becomes explosive [89]. Therefore it is clear that developing fast, highly sensitive hydrogen sensors is technologically very important.

It is well known that palladium has a high hydrogen solubility [90] and thus is a material of choice as the active element for hydrogen sensors or as a hydrogen filter. In the presence of hydrogen, palladium forms palladium hydride, PdH_x, $0<x<1$, where the content of the hydrogen dissolved in palladium depends both on the temperature and the partial pressure of hydrogen. Palladium hydride may be considered as an interstitial alloy where the octahedral sites of the face centered cubic metal lattice are occupied by hydrogen. The palladium-hydrogen system shows structural phase transition under increasing hydrogen content from the low concentration hydrogen-saturated phase called the α-phase, to the high concentration defective phase called the β-phase. Upon the phase transition to β-phase, the resistivity shows an increase by a factor of up to 1.8 at room temperature [90]. This resistivity increase is utilized in macroscopic palladium resistors as hydrogen sensors.

At room temperature, the transition from α to β phase occurs at 8 torr of hydrogen partial pressure (~ 1-2 % volumetric concentration of atmospheric pressure) [90] and the phase transition leads to a change in the lattice constant from 3.895 angstroms to (the maximal value for the α phase) to 4.025 angstroms (the minimal value for the β phase). This leads to an increase of ~ 3.5 % in lattice constant or 11 % increase in volume [91, 92].The swelling of the Pd lattice is utilized by researchers to prepare hydrogen sensors from electrodeposited palladium arrays [93] or palladium thin films near the percolation threshold [94, 95].

In my research, I tried to fabricate nanogaps in palladium nanowires using electromigration and use them as hydrogen sensors by utilizing the hydrogen induced lattice expansion of palladium to close the gap, i.e. my sensors would work as hydrogen-activated relays that would consume no power in the absence of hydrogen but would conduct when there is hydrogen present in the environment. My sensors were indeed sensitive to the presence of Hydrogen but unfortunately they showed slow response times due to in plane stress of the metal film on the substrate.

7.2: Device fabrication and Measurement setup

I prepared my devices using EBL (See i.e. section 4.2). I prepared two types of devices. In the first type, after a single step of EBL I deposited approximately 40 nm palladium at a rate of 0.4 Angstroms per second using a thermal deposition chamber, forming both the palladium nanowires and the rest of the device including the contact pads in the same thickness of metallization. In the second type of devices, I performed two lithography steps where in the first step I deposited Pd to form

nanowires of thickness 20 to 40 nm and in the second lithography step I deposited Cr/Au metallization typically 50-100 nm to form the contacts to the nanowires and the bonding pads. SEM micrographs of both types of devices are shown in Figure 7-1 and 7-2 below.

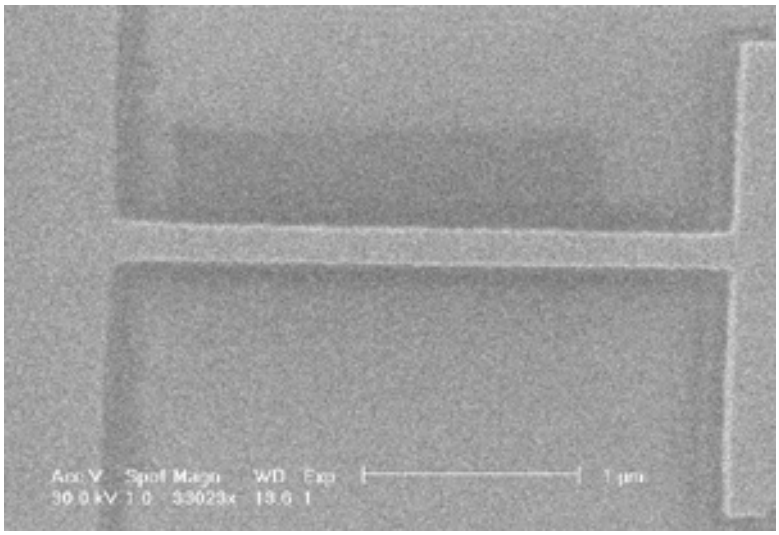

Figure 7-1. A palladium device (before electromigration) where the thin palladium line and the rest of the device have the same thickness of metallization. The scale bar in the figure is one micron.

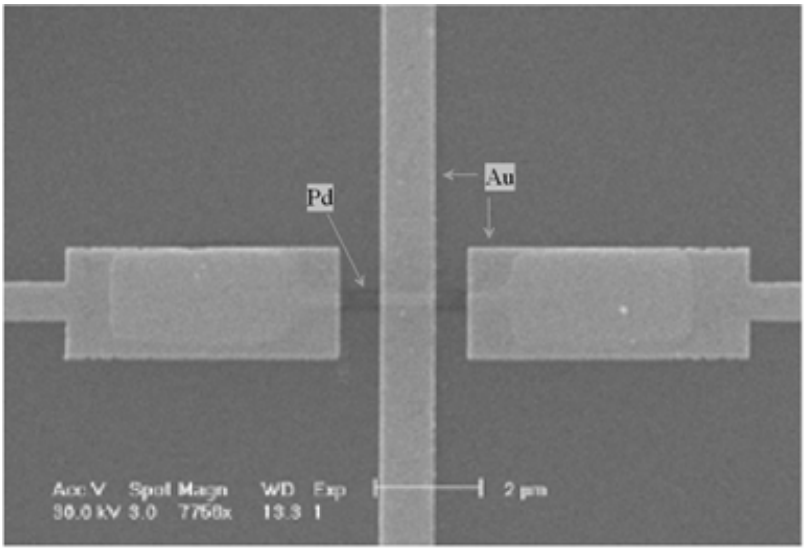

Figure 7-2. Palladium devices where the electromigrated thin line is palladium and the rest of the metallization in the device is Cr/Au. The device was fabricated in two steps of lithography. The palladium metallization in the figure is 20 nm and the Au metallization is 55 nm. The scale bar is two microns.

I measured the hydrogen sensing properties of the devices under different volume percentages of hydrogen in nitrogen using a custom-built measurement setup as shown in Figure 7-3 (a) and (b) below. I regulated the volume percentage of hydrogen in nitrogen gas by regulating their flow using two flow meters purchased from Omega Inc. Model FL-3861 ST is used for controlling the H_2 flow, and Model FL-3805 ST is used for controlling the N_2 flow. While keeping the nitrogen flow constant, I started and stopped hydrogen flow using an electrically controllable On/Off solenoid valve purchased from Teknocraft Inc. Figure 7-3 (b) shows the measurement box.

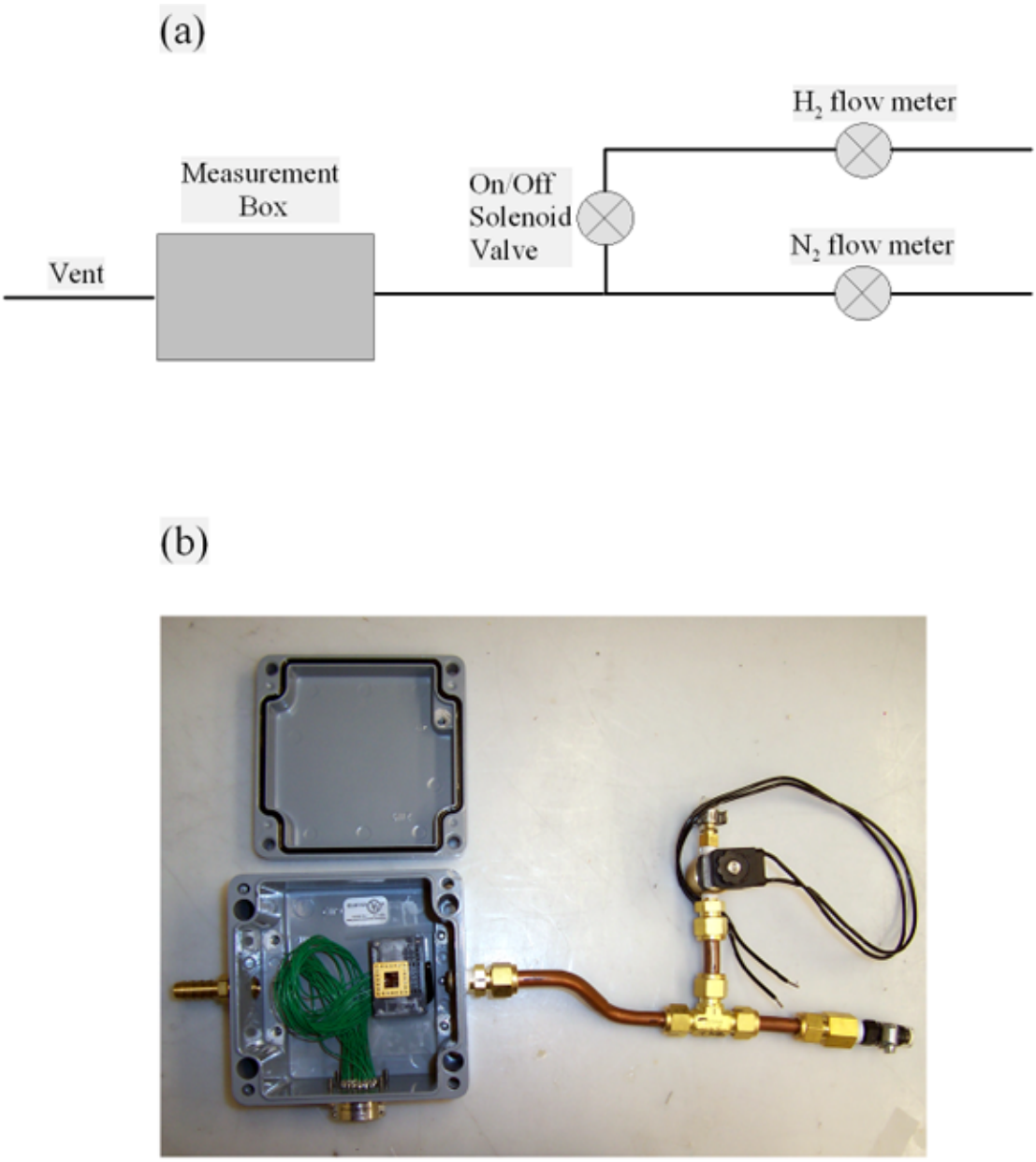

Figure 7-3. Measurement setup used in hydrogen sensor experiments. (a) shows the gas flow and mixing schematically before it flows into the box. (b) shows inside of the box and On/Off solenoid valve used to start and stop H2 flow. The dimensions of the box are 4.80 X 4.72 X 3.15 inches.

7.2: Results and Discussion

I will first discuss the electromigration characteristics of the devices and the nanogap formation via electromigration. I performed electromigration in a nitrogen environment at room temperature prior to sensing experiments. Electromigration was accomplished by increasing the voltage bias until the device failed and the current reduced to zero. In the devices where I had one layer of Pd metallization, I attempted electromigration using feedback, but I couldn't succeed in controlling the rate of electromigration. In this case, nanogaps in Pd lines were formed by abrupt failure of the lines. Figure 7-4 shows the nanogap formation after electromigration.

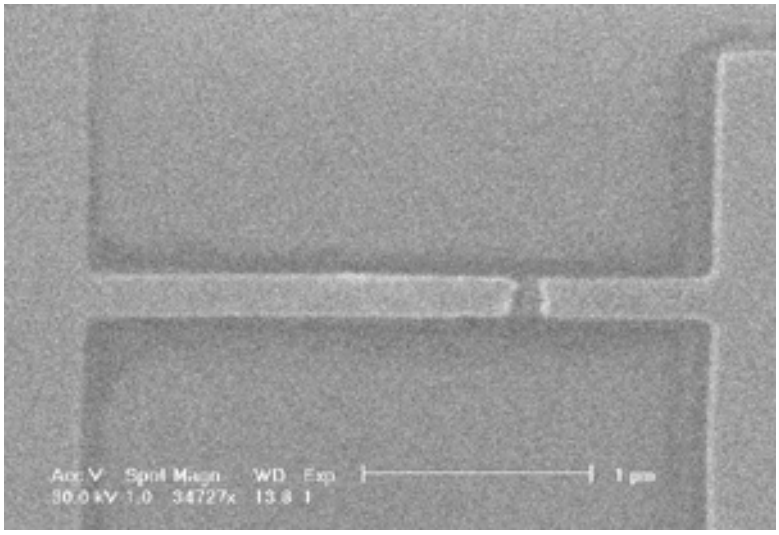

Figure 7-4. Nanogap formed via electromigration in a Pd device. The gap is several hundred nanometers wide and formed via electromigration after increasing the voltage bias until failure occurs. The scale bar in the figure shows one micron length scale.

In devices where I had two layers of metallization (The Pd nanowire and Au leads) I was able to control the rate of electromigration and perform electromigration controllably. Figure 7-5 shows post-mortem SEM images of nanogaps formed via controllable electromigration.

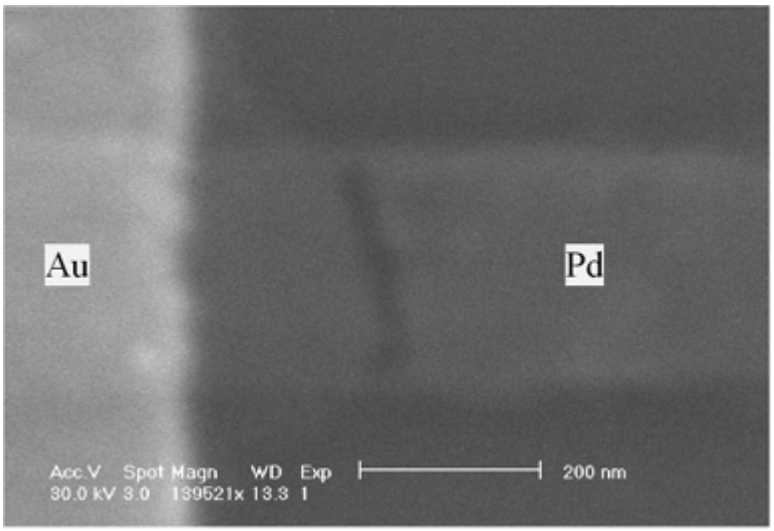

Figure 7-5. Nanogaps formed via electromigration in palladium devices with gold contacts. The nanogaps are formed via controllable electromigration. In the SEM micrograph the electromigration through the grain boundary and the void formation between grains is observed. The scale bar in the figure shows 200 nm length scale.

Below Figure 7.6 shows a typical I-V curve taken during the controllable electromigration of a Pd line with gold contacts.

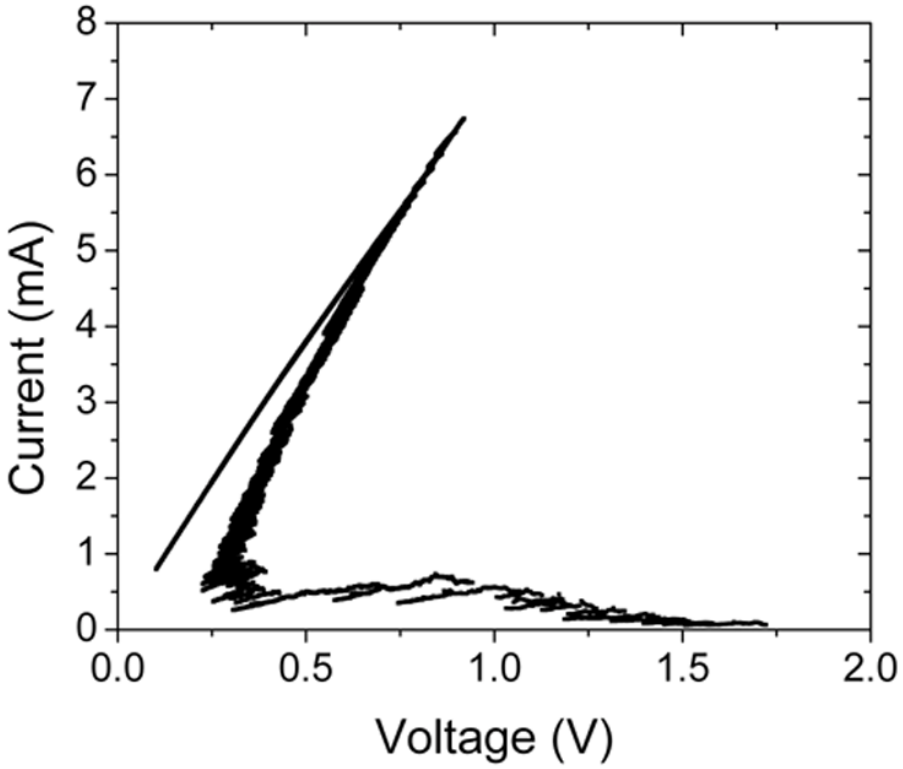

Figure 7-6. Controllable electromigration of a Pd device with gold contact. Data is taken at room temperature in nitrogen environment at room temperature.

The I-V curve of electromigration is similar to the gold lines indicating that power dissipated in the junction increases the local temperature until the electromigrating atoms acquires enough mobility. However, unlike the electromigration in gold, turning off the feedback loop during electromigration resulted in abrupt failure of the wire rather than a jump to the stable branch. Figure 7-7 shows the I-V curve of a sample at which the feedback is turned off during the electromigration.

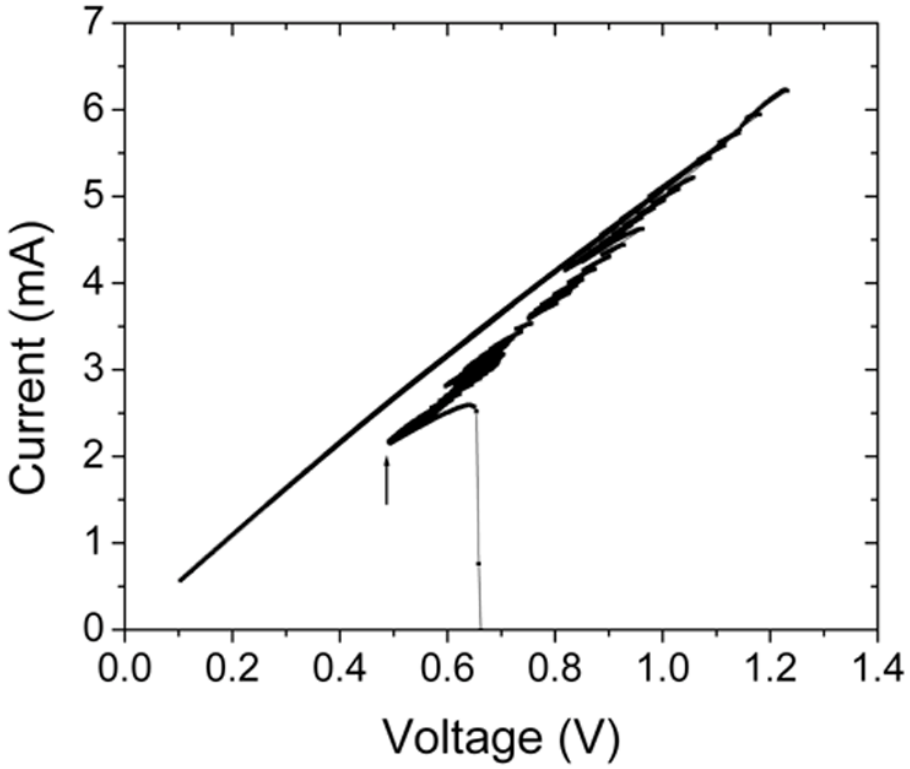

Figure 7-7. I-V curve of a palladium line where the feedback is turned off during the electromigration. The arrow shows the point of turning the feedback off. Unlike the electromigration in gold lines, electromigration does not evolve smoothly after turning off the feedback.

This is not unexpected considering that palladium has a surface oxide that blocks the surface electromigration, leaving the bulk and the grain boundaries as the possible pathways for the electromigration. Blocking the surface electromigration causes the stress buildup in the electromigrating line and abrupt failure instead of a smooth self limiting electromigration as observed in gold [See i.e. the discussion in sections 2.2.2.2 and 2.2.2.3 in Chapter 2]. Comparison of post mortem SEM pictures

of devices also shows the difference of electromigration in gold and palladium. Figure 7-8 shows an SEM micrograph of a gold sample electromigrated using a feedback loop. Comparing with figure 7-5, we may observe the neck formation in the gold sample, indicating that electromigration removes atoms from the surface form all sides and acts as an electromechanical etching process. But in figure 7-5 instead of a neck formation, we observe formation of a void after electromigration.

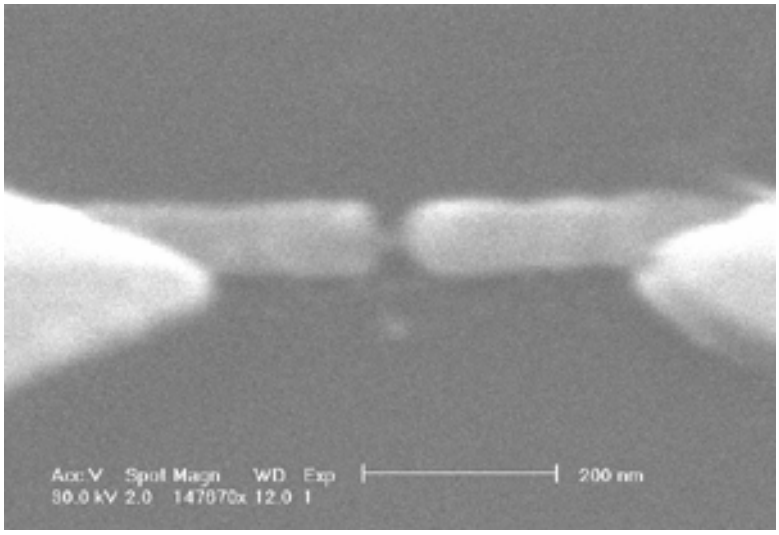

Figure 7-8. Formation of a neck in the junction after electromigration of a gold line. The scale bar in the figure shows 200 nm length scale.

We will now discuss the sensor responses of both types of devices. We first fabricated and measured the sensing response of first type of devices where we had only palladium metallization. Figure 7-9 (a) and (b) below shows the typical turn on responses we observed upon introduction of Hydrogen into the Nitrogen flow. Figure

7-10 (a) and (b) shows the typical turn off responses we observed upon turning off the Hydrogen flow.

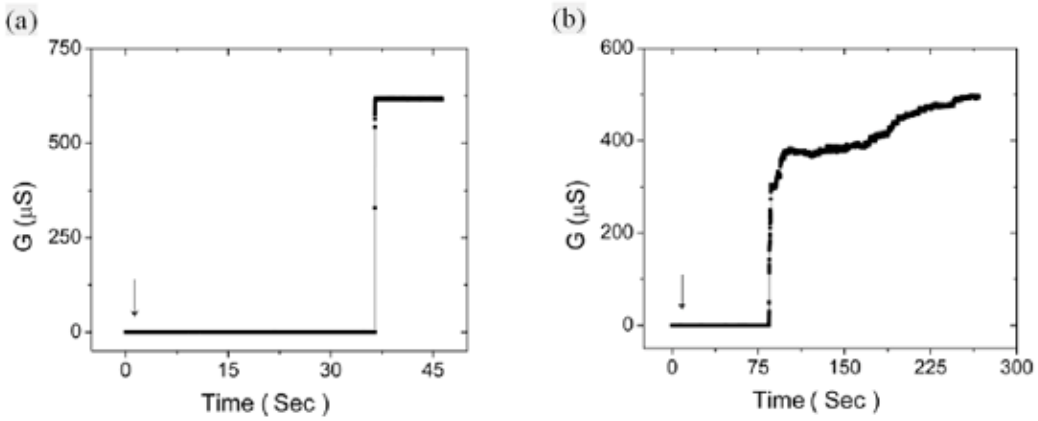

Figure 7-9. Typical turn-on behavior of sensor devices fabricated with only palladium metallization. (a) shows turn-on behavior for 5.8 % volume percentage of hydrogen in nitrogen and (b) shows the behavior for 3.9 % hydrogen. The arrows indicate when hydrogen is introduced into nitrogen flow.

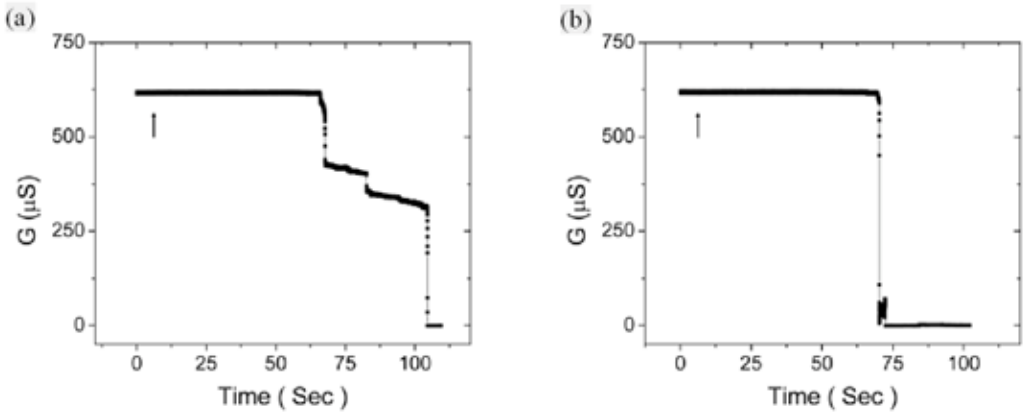

Figure 7-10. Typical turn off behaviors of devices fabricated with only palladium metallization. The arrows in the figures show when the hydrogen flow is turned off.

In our devices we have observed response times to the presence of hydrogen typically ranging from tens of seconds to hundreds of seconds. In general, the turn on response of our devices become relatively slower in lower concentrations of hydrogen compared to higher concentrations. We also observed higher conductance values and more stable contacts for higher concentrations of hydrogen. Similar slow response to hydrogen is observed previously in ultra thin palladium films [95-97]. It is known that for a thin film attached to a hard substrate the in-plane stress for expansion is on the order of several gigapascals [98, 99]. So when such structure is loaded with hydrogen, the lattice expansion is directed out of plane [100-102], but our devices rely on the in plane expansion of the nanogaps produced in palladium nanowires. We see the effect of high in-plane stress in turn off responses of our devices as well. Contact making and breaking in our devices occurred sometimes instantaneously and sometimes stepwise as shown in Figures 7-9 and 7-10 independent of the concentration of the

hydrogen used. We also observed both behaviors for the same concentration of hydrogen for different turn-on and turn-off cycles.

To overcome the above difficulties I tried to fabricate smaller gaps by using controllable electromigration and hence I fabricated the devices with palladium nanowire and gold contacts and bonding pads in order to reduce the series device resistance. In these devices I was able to fabricate nanogaps on the order of tens of nanometers. But their hydrogen response was worse than the first type of devices; the devices were not sensitive to presence of hydrogen for less than 5 % volume percentage and their response occurred more slowly. This indicates that the palladium contacts as well as the palladium nanowires in the first type of devices participated in overcoming high in-plane stress. We also tried to etch the SiO_2 from the sides of the nanowire for approximately 50 nanometers to reduce the effect of the substrate but this did not improve the hydrogen response of the devices.

7.4: Conclusion

In conclusion, I have fabricated hydrogen sensors out of palladium nanogaps fabricated via electromigration. For both turn-on and turn-off behavior, our sensors showed response times on the order of minutes. Such slow response is due to direct attachment of thin film to the hard substrate as was observed before for ultra thin palladium thin films used for hydrogen sensing. [95]. For substrates such as cyanoacrylate [93] response times as fast as 75 milliseconds were measured. It is also shown that [94] by using a self assembled monolayer as a lubrication layer the response times for ultra thin palladium films can be improved by several orders of magnitudes from minutes to tens of milliseconds. Unfortunately the fabrication process we used for device fabrication is not compatible with using such lubricant layers. Our results might be improved by fabricating nanowires without using a resist layer such as shadow masking, on a hard substrate covered with a lubrication layer such as siloxane.

Chapter 8: CNT Thin Films as Chemical Sensors- Fabrication and Measurement Technique

8.1: Introduction

Carbon CNTs (CNTs) were discovered in 1991 by S. Iijima while studying the fullerene production methods [103]. After their discovery, this new material has been studied intensively [104, 105] and has become the material of choice of many experimental groups due to its superior electrical [106-113], mechanical [114, 115] and chemical [116-118] properties. In many ways CNTs are unique materials. They are inherently one dimensional which makes them ideal for studying phenomena unique to one dimensional systems such as the Luttinger liquid ground state of conduction electrons [107, 119]. Another unique property CNTs possess is that all their atoms are on the surface and hence their conduction properties may be affected grossly by the chemical environment.

The structure of a CNT can be thought as a single two-dimensional sheet of graphite (termed graphene) seamlessly rolled up to form a tube. CNTs can be multi walled (MWNT) or single walled (SWNT) where the MWNT consist of several concentric shells of SWNT. SWNT can be metallic or semiconducting depending on their chirality as theoretically predicted [106, 108] and experimentally observed [109, 120].

Although individual CNTs can be either semiconducting or metallic, with the growth and separation methods known today, it is not possible to selectively grow only one kind (metallic or semiconducting) or successfully separate semiconducting

and metallic CNTs from each other after the growth. Therefore the experiments done on individual CNTs are made in general by first growing or depositing sparse density of CNTs on the substrate and later finding individual CNTs (mostly with the help of an alignment pattern) and connecting them with metallic contacts followed by identification as metal or semiconductor using their electrical characteristics such as their transconductance.

Therefore considerable attention has been given to the utilization of thin films of CNTs as electronic material in many applications such as thin film transistors on both hard and flexible substrates [121-123], diodes [124] or as transparent conductive coatings [125]. The CNT thin film consists of a random network of CNTs bound to a substrate, and films considerably thinner than a single monolayer are routinely studied. CNT thin films have the advantage that although the electronic properties of single CNT devices depend on the chirality and the diameter of each CNT and the conduction characteristics of each device is not exactly reproducible, in thin films the effects of individual variations are suppressed by the ensemble averaging over a large number of CNTs.

Thin films of SWNTs will be electrically continuous provided that the density of the CNTs in the film is high enough, i.e. above the percolation threshold. The percolation threshold is defined as the critical density above which there exists a continuous electrical path connecting arbitrarily distant points. In the case of CNT thin films it can be estimated as the density at which the average distance between the CNTs will be equal to their average length [123]. The electronic properties of the film then depend on the electronic properties of the individual CNTs in the film and the

degree of connectivity between the CNTs. This system can be seen as analogous to the two-dimensional random resistor networks studied in percolation theory. It is also pointed out[126] that above the percolation threshold the behavior of such a network can be understood as a consequence of the mathematical properties of the finite sized percolation of CNTs with variable intertube coupling.

Given that, in a SWNT, all the carbon atoms are on the surface, it is reasonable to explore the use of SWNTs as active transducer elements for chemical sensing applications. Both devices using isolated CNTs [116, 117] and thin films or bundles of CNTs [127-129] have been used for chemical sensing as chemiresistors via monitoring their resistance change upon exposure to analyte under test. The observed conductance change is attributed to the doping upon gas adsorption and/or increasing scattering on the CNT surface. Theoretical studies also predict significant changes in the conduction properties of CNTs upon gas adsorption [130, 131].

Another possible use of thin films of CNTs is to utilize them as electrodes for capacitative gas sensors [132-134]. In these works the CNT film is utilized as one plate of a parallel plate capacitor that where the gate layer (generally highly doped conductive silicon) is used as the other plate. The presence of the analyte is detected by monitoring the change of the capacitance between the gate and the CNT film. The change of the capacitance is attributed to the polarization of the adsorbed molecules on the CNT surface and the change in the quantum capacitance due to charge transfer from analyte to CNT network.

But little or no attention has been given so far to the fact that the CNTs will have a layer of water on their surface in ambient conditions and analysis in terms of

doping and charge transfer should take the water layer into account [135]. In addition, the CNT network will consists of interconnected CNTs each with capacitance to the gate and resistance that comes from scattering centers such as defects and/or CNT-CNT junctions. Such a network will have frequency-dependent capacitance (i.e. out-of-phase component of the impedance) that will be affected by the changing resistance of the CNT network.

To elucidate this point further, I have taken capacitance and conductance measurements of CNT networks at frequency range between 50 Hz to 20 KHz. The experiments were performed in ambient conditions, ultra-high vacuum (UHV), and under several analyte pressures up to 10^{-6} Torr. The results are described in Chapter 9.

8.2: Device fabrication and Measurement setup

8.2.1: CNT Synthesis

Although CNTs were discovered as products of arc discharge between two graphite rods [103], other methods such as laser ablation [136], the high-pressure carbon-monoxide (HIPCO) process [137, 138], and chemical vapor deposition (CVD) [139, 140] were soon discovered to synthesize CNT material.

I used the CVD method to prepare the CNT thin films. The growth of CNTs is catalyzed by iron nanoparticles [141] where the size of the catalyst determines the diameter of the resulting CNTs [142]. The recipe I followed for the CNT growth is adapted from reference [141, 143], and is as follows. I first dissolve ferric nitrate ($Fe(NO_3)_3$) in isopropyl alcohol (IPA). To ensure that the ($Fe(NO_3)_3$) salt is well

dissolved, I stir the solution using a magnetic stirrer bar for ~ 4-5 hours or overnight. Prior to CVD process, ($Fe(NO_3)_3$) salt is precipitated on the substrate by dipping it into the ($Fe(NO_3)_3$)-IPA solution for approximately 10 seconds and into hexanes for approximately 2 seconds.

The substrate is then placed into a quartz boat and then the boat is placed into a quartz tube in the center of the growth oven. (i.e. see the figure 8-1). Following this the gas lines are purged with argon and the oven is heated to 850 degrees. After the temperature is stabilized, the growth using the feedstock gases are flowed according to the recipe in table 8-1.

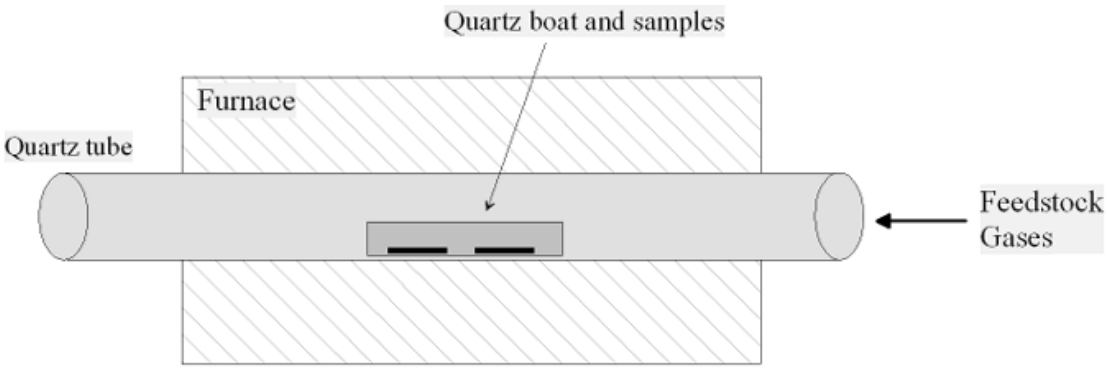

Figure 8-1. Schematic of CNT growth apparatus. Samples were placed in the middle of the quartz tube and feedstock gases are flowed while the oven was at 850 degrees for CVD growth of CNTs.

Action	Gas	Flow (sccm)	Temp (°C)	Time (minute)
Purge	Ar	730	RT	10
Heat	Ar	730	RT→600	10
Heat	Ar	730	600→750	5
Heat	Ar	730	750→800	5
Heat	Ar	730	800→825	5
Heat	Ar	730	825→850	10
Nanotube Growth	H_2	1900	850	10
	CH_4	1300		
	C_2H_4	86		
Cool Down	Ar	730	850→RT	~5 Hours

Table 8-1. CNT growth recipe

Figure 8-2 shows the SEM image of the CNTs [144] grown on 500 nm thick silicon dioxide substrate on degenerately doped silicon according to the recipe in table 8-1. To ensure that I get dense and well connected networks of CNTs above the percolation threshold, I used fairly high catalyst density of 200 μg/ml ferric nitrate solution in IPA.

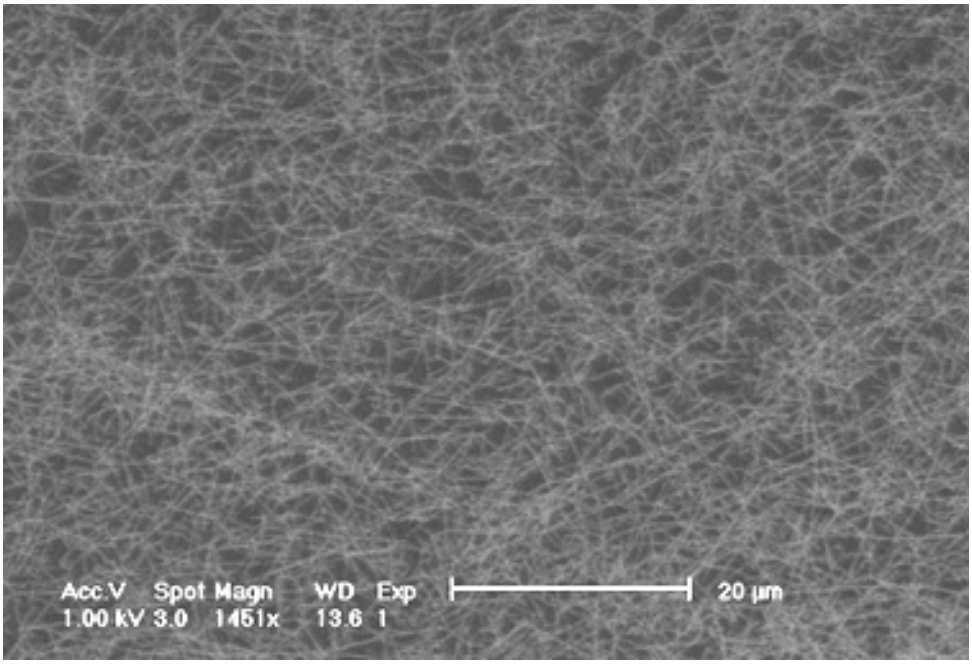

Figure 8-2. SEM micrograph of the thin film of CNT network material after CVD growth on Si/SiO_2 substrate. The CNTs are grown with relatively high catalyst density (200 microgram/ml) to ensure a well connected network.

8.2.2: Device Fabrication and Measurement Setup

After the CNT material on Si/SiO_2 substrate is grown, I prepared my devices with two steps of photolithography. The recipe I used in device fabrication is as follows. In the first step, I spun photoresist (S1813) on the sample for 45 seconds at 4500 rpm and baked it at hot plate for 60 seconds, producing approximately 1.4 micrometers thick resist layer. After exposure to ultraviolet light (CL2 for 15 seconds) and developing the resist layer (in CD-30 for 45 seconds following rinse with DI water and N_2 blow dry), I deposited the metal layer (5 nm Cr / 55 nm Au)

that produces the interdigitated electrode pairs for conductance measurements. In the second lithography step I covered with resist the region inside the interdigitated electrode pairs to form the device and removed the CNTs from the other areas on the surface by using oxygen plasma etch (50 second etch at 100 W power and 300 militorr oxygen pressure). Figure 8-3 shows the SEM micrograph of the completed device.

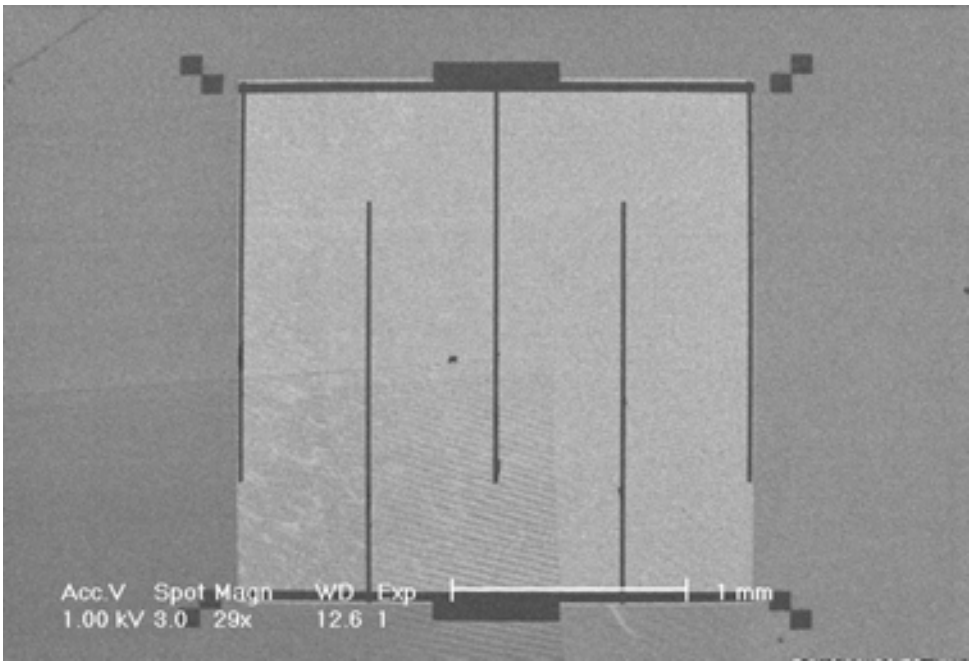

Figure 8-3. SEM micrograph of the CNT network device. The interdigitated electrode pairs form the source and drain contacts for conductance measurements. For capacitance measurements, both the electrode pairs and the CNT network form one plate of the parallel plate capacitor where the other electrode of the pair is formed by the degenerately doped Si underneath the SiO_2 dielectric.

After the device fabrication I glued my samples onto a sample holder using silver epoxy and placed them into a UHV chamber equipped with a leak detector and a mass spectrometer to calibrate the partial pressure of the analyte under measurement, i.e. see figure 8-4. I conducted my experiments as follows. I first pumped the UHV chamber containing the sample to pressure less than 10^{-10} Torr (including baking the chamber using heating tape to remove adsorbates from the inner walls of the UHV chamber). Later I attached the gas container or the vial containing the analyte to the leak valve that is attached to the UHV chamber. I purified the liquid analytes such as acetone using the well known cold freeze-pump-thaw cycle via the following procedure. I first solidified the liquid to be purified using a liquid cryogen bath such as liquid nitrogen. Once the analyte was frozen, I pumped the residual gases in the vial (that are not frozen) using a sorption pump. Following this I closed the valve that connects the vial to the sorption pump and thawed the frozen liquid in the vial using a water bath at room temperature. I repeated this cycle approximately four or five times. To check the purity of the analyte that I introduced into the chamber, and the partial pressure of the analyte in the chamber, I measured and calibrated the leak using a mass spectrometer (SRS RGA 200). After the calibration step I baked my sample in UHV above 200 ^{o}C to be sure that the adsorbed molecules and the water vapor were desorbed from the surface. After my sample was cooled down to room temperature again I turned off the pressure gauge and the filament of the mass spectrometer, and introduced the analyte using the pre-calibrated position of the leak valve. I took capacitance measurements using an Andeen Hagerling 2700A 50Hz-20 KHz Ultra-Precision Capacitance Bridge.

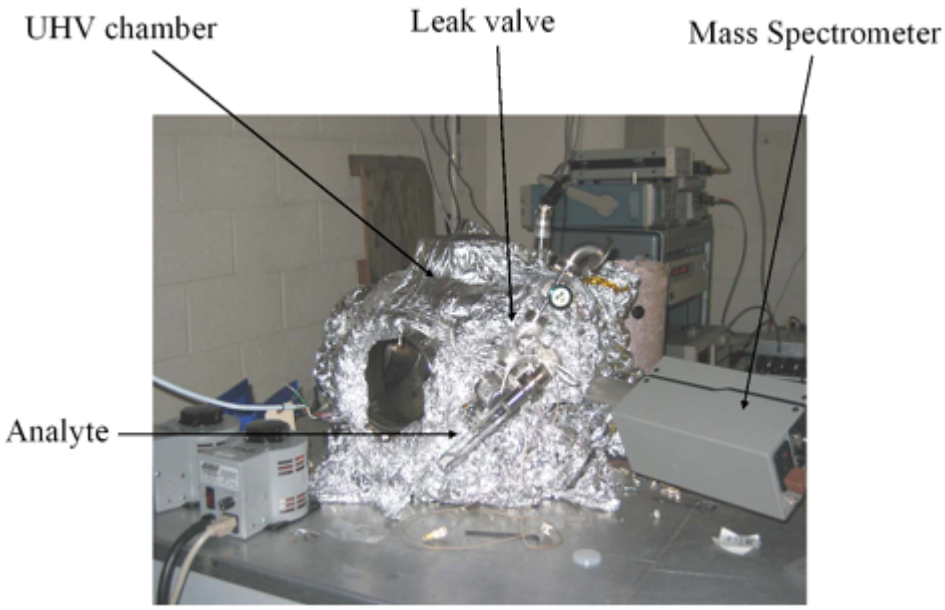

Figure 8-4. UHV system used in the experiment

Chapter 9: CNT Thin Films as Chemical Sensors-Results

9.1: Introduction

First I will discuss the qualitative behavior of the capacitance and conductance as a function of gate voltage and frequency. Figures 9-1 and 9-2 show the general behavior of the capacitance and conductance of the CNT thin film device as a function of gate voltage. The capacitance of the CNT network was measured using an AC signal applied between the source and the gate electrodes and using 0.1 V RMS amplitude of the drive frequency, and the conductance of the CNT network using DC voltage bias. Although capacitance and conductance are measured using two different techniques, the similar shape of the curves (including the hysteresis[145]) hints that the capacitance and conductance are possibly interrelated.

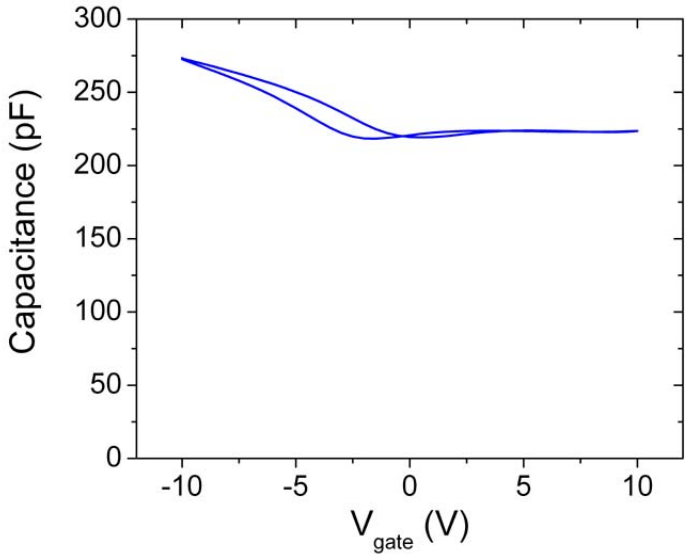

Figure 9-1. Capacitance of CNT network as a function of gate voltage. Capacitance is measured in UHV by applying 14 KHz sinusoidal drive voltage at 0.1 V RMS. The gate voltage is swept from 10 V to +10V and back to -10V; both the up sweep and down sweep are shown.

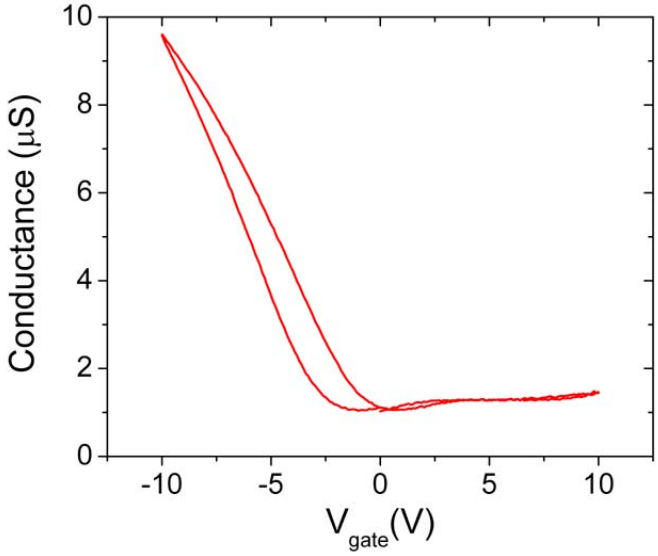

Figure 9-2. Conductance of CNT network as a function of gate voltage. Conductance is measured in UHV by applying 500 mV source-drain bias.

Figure 9-3 shows the measured capacitance as a function of frequency of the applied signal at zero gate voltage. In general we observed a decrease in the capacitance with increasing frequency. In order to understand and explain the results, we model the CNT film over the back gate electrode as an RC transmission line as discussed below.

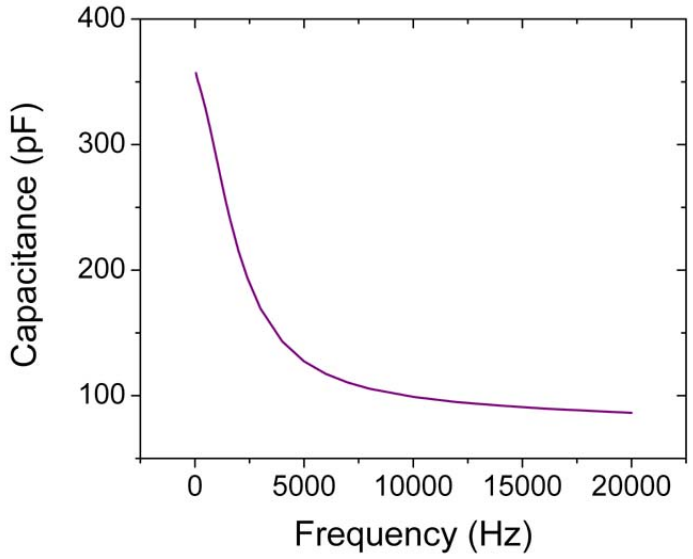

Figure 9-3. Capacitance as a function of frequency. The capacitance is measured at zero volt gate voltage in ambient conditions.

9.2: CNT networks modeled as an RC transmission line.

The CNT thin film is composed of individual CNTs that are well connected, with each CNT having resistance due to scattering centers such as defects and CNT-CNT connections, and having capacitance to the gate. Such network is very similar to an RC transmission line. Therefore before I discuss the experimental results, I first will discuss the analysis of such a transmission line. In my analysis I neglect the conductance to the gate due to high dielectric constant of the SiO_2. I also neglect the inductance of the CNTs which is reasonable at low frequencies, where the resistance dominates the inductive reactance. In the discrete case the analysis of such a transmission line can be made by using basic electrodynamics. In figure 9-4 I

schematically describe such a transmission line composed out of capacitors and resistors.

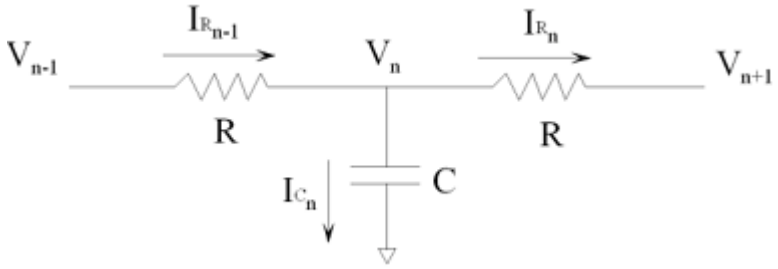

Figure 9-4. Schematic of an RC transmission line.

Using Kirchov`s current law, an equation for the currents at the branch point can be written as

$$I_{R_{n-1}} = I_{R_n} + I_{C_n} \qquad \text{Equation 9-1}$$

or

$$\frac{V_{n-1} - V_n}{R} = \frac{V_n - V_{n+1}}{R} + C\frac{dV_n}{dt} \qquad \text{Equation 9-2}$$

The above equation may be rewritten as

$$\frac{V_{n-1}-V_n}{R}-\frac{V_n-V_{n+1}}{R}=C\frac{dV_n}{dt}$$ Equation 9-3

Dividing by L^2 and define $r=\frac{R}{L}$ as the resistance per unit length and $c=\frac{C}{L}$ as the capacitance per unit length, one arrives at a diffusion equation for the voltage:

$$\frac{dV}{dt}=\frac{1}{rc}\frac{d^2V}{dx^2}$$ Equation 9-4

For a sinusoidal drive voltage $V(0,t)=V_o e^{i\omega t}$ one expects a decaying solution $V(x,t)=V_o e^{i\omega t}e^{-\lambda x}$. Inserting into the diffusion equation one finds the characteristic decay constant:

$$\lambda=\frac{(1+i)}{\sqrt{2}}\sqrt{rc\omega}$$ Equation 9-5

This indicates that signals will decay over a length

$$l_o=\sqrt{\frac{2}{r\omega c}}$$ Equation 9-6

To derive the continuous case from the discrete case the current may be written

$$I(0,t) = -\frac{1}{r}\frac{dV}{dx}\bigg|_{x=0}$$ Equation 9-7

Inserting the decaying solution into the equation one finds

$$I(0,t) = \frac{\lambda}{r}V_o e^{i\omega t}$$ Equation 9-8

The complex impedance of the transmission line may then be written as

$$Z = \frac{r}{\lambda} = \frac{(1-i)}{\sqrt{2}}\sqrt{\frac{r}{\omega c}}$$ Equation 9-9

Comparing the above result with the impedance of the circuit composed of a series capacitor and resistor, that is $Z = R_{Eff.} - \frac{i}{\omega C_{Eff.}}$, I define the effective resistance and capacitance of my device as:

$$R_{Eff.} = \sqrt{\frac{r}{2\omega c}} = \frac{1}{2}rl_o$$ Equation 9-10

and

$$C_{Eff.} = \sqrt{\frac{2c}{\omega r}} = cl_o$$ Equation 9-11

Note that R_{Eff} and C_{Eff} may be thought of as the resistance and capacitance of a section of the transmission line equal to the decay length l_0.

Figure 9-5 shows the change of the device capacitance as a function of the drive frequency. I measured the capacitance by using AH 2700 Ultra-Precision Capacitance Bridge that allows simultaneously application of both an AC voltage between gate and the device for capacitance measurement as well as a DC voltage between the device and the gate and hence allows changing the carrier concentration in the CNT mat. R_{Eff} and C_{Eff} correspond to the measured signals by the capacitance bridge, which interprets the circuit as a series capacitor and resistor. By looking at the effective capacitance, $C_{Eff.} = \sqrt{\frac{2c}{\omega r}}$ we expect the capacitance to decay with the inverse square root of the frequency. The solid line in Figure 9-5 is guide to eye and shows the slope of $-1/2$.

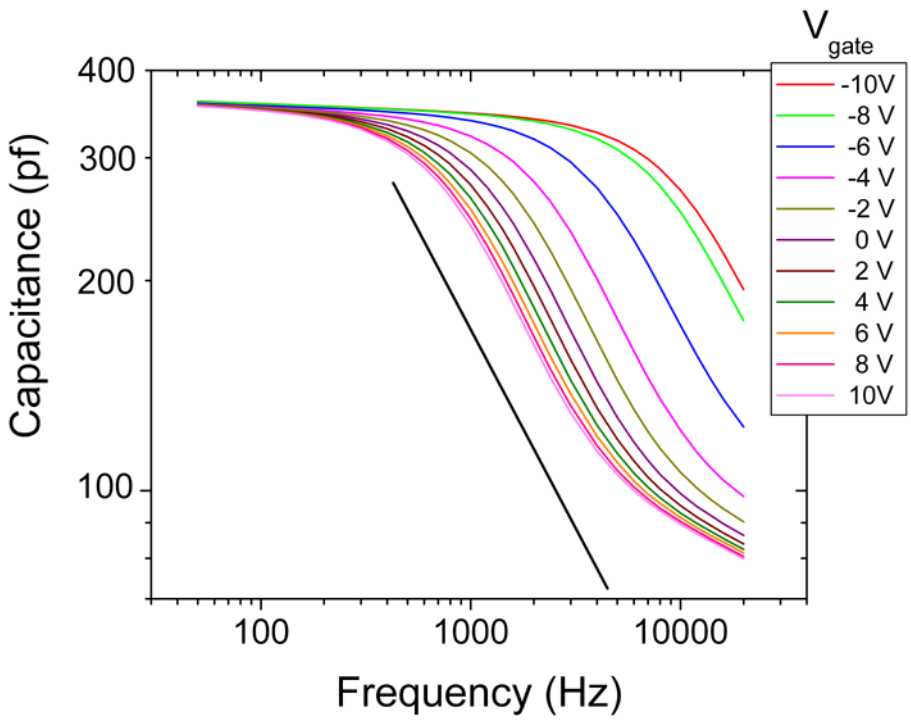

Figure 9-5. Device capacitance as a function of drive frequency at different gate voltages at ambient atmosphere. The RMS amplitude of applied voltage during measurement was 0.1 Volts. The solid line is a guide to eye showing -1/2 slope.

The capacitance of my device decays with increasing frequency where the roll-off of the decay starts at higher frequency values for higher carrier concentration (lower gate voltages). I explain this effect by considering all the capacitors in the device and the propagation of the applied AC signal (See figure 9-6). The device capacitance to the gate is composed of three capacitances: the capacitance of source to the gate which is independent of the frequency, the capacitance of CNT mat to the gate which depends on frequency, and the capacitance of drain contact to the gate which is independent of the frequency. The device capacitance is measured by applying AC voltage between source contact and the gate. For low frequency values

the measured capacitance includes all the three capacitances, but as the frequency increases, the contribution of CNT network to the capacitance decreases since the signal decays in the CNT network, and the contribution from the drain capacitance also decreases, since a smaller signal reaches the drain.

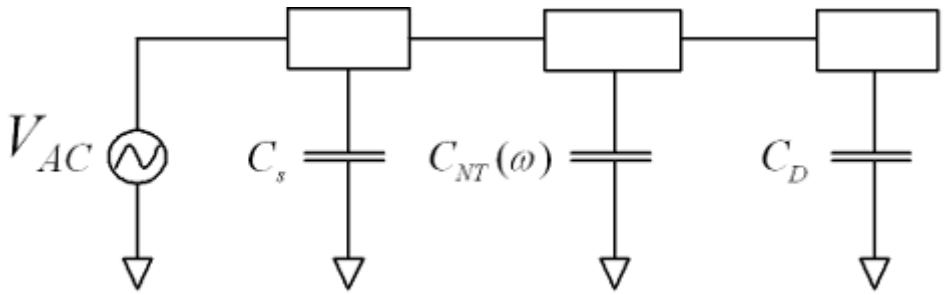

Figure 9-6. Schematics of source, drain and the gate capacitors. Capacitance measurements are taken by using Andeen-Hagerling 2700A Ultra-Precision Capacitance Bridge with 0.1 Volts AC voltage applied to source electrode.

At low frequencies, the capacitance of the nanotube film should be given by the capacitance per length c times the length L, i.e. $C_{NT} = cL$. At high frequencies, the capacitance is give by equation 9-11 $C_{NT} = cl_o$. Thus the crossover occurs roughly when $l_o = L$ or at a roll off frequency $\omega_o = \frac{2}{rcL^2}$. Thus the roll off frequency will change with gate voltage as the resistance per length changes; at high negative gate voltages, when the film is less resistive, the roll off frequency is higher. The DC device resistance per length r varies monotonically from 7.6×10^7 to 1×10^9 Ω/m for V_g = -10 V and +10 V respectively, which should correspond to a roll-off

frequency (using $l_0 = L$) of $\omega/2\pi$ = 3.5 – 50 kHz, which is approximately one order of magnitude higher than the observed roll-off. The source of this quantitative discrepancy is not clear, but likely reflects that the average resistance and capacitance per length of the film do not reflect the resistance per length and capacitance per length of the individual conducting paths that dominate the conduction.

From equation 9-11 we can see that the effective capacitance is proportional to the square root of conductance, and therefore the variation of the square root of conductance with gate voltage should produce a proportional change in the capacitance. Figure 9-7 below shows the capacitance and the square root of conductance as a function of gate voltage.

The change in the capacitance of similar CNT network devices as a function of gate voltage has been observed before [134], and attributed to the change of the quantum capacitance due to gate field induced doping as follows. The capacitance of the CNT is given by $C_{tot}^{-1} = C_{el}^{-1} + C_q^{-1}$ where C_{el} is the electrostatic capacitance, $C_q = e^2 D(E)$ is the quantum capacitance, e is the electronic charge and $D(E)$ is the density of states. Thus, in the off-state at positive gate voltage, the Fermi level presumably lies in the semiconducting CNT gap, and $D(E)$ is small so the quantum capacitance dominates and C_{tot} is small. However, in Figure 9-7 the proportionality of capacitance and the inverse square root of resistance indicate that the change in the capacitance is almost entirely explained by the change in the resistivity of the CNT network, with no need to resort to the quantum capacitance to explain the change. I do not understand completely the absence of a change in capacitance between on and

off state, but possible origins are a finite density of states in the semiconducting CNT gap, or on/off behavior occurring before the semiconducting CNTs are fully depleted.

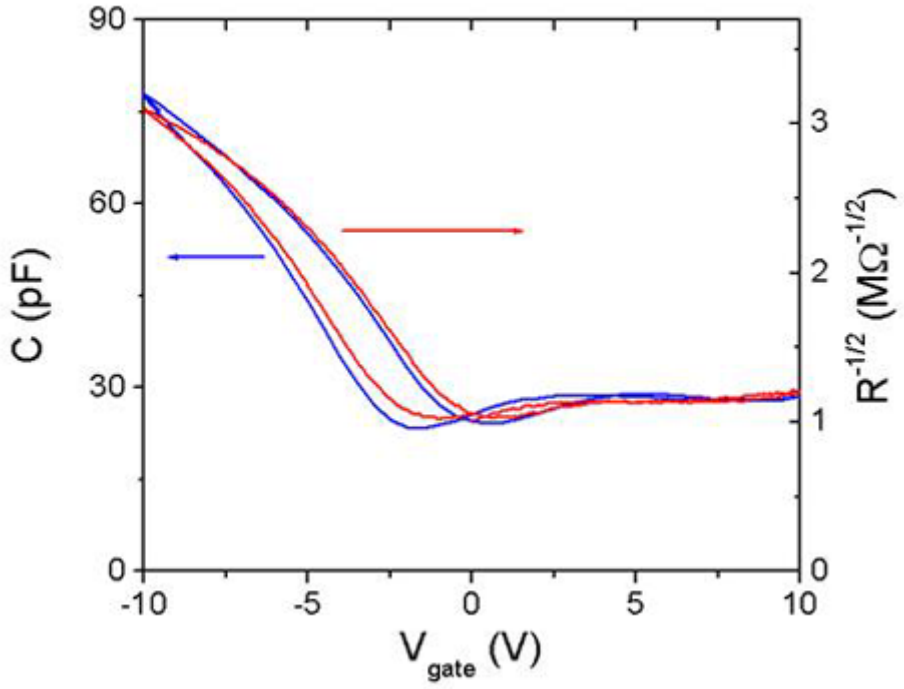

Figure 9-7. Capacitance and inverse square root of resistance of the CNT thin film device as a function of gate voltage. Both data are taken in UHV (< -10 Torr pressure). Capacitance is measured by applying 14 KHz sinusoidal drive voltage at 0.1 V RMS, and the resistance is measured by applying 500 mV source-drain bias. A constant 195 pf (approximately equal to the capacitance of the contacts) has been subtracted from the capacitance.

9.3: Effect of low pressure gas adsorption on the conductance and the capacitance of CNT films

The effect of gas adsorption on the electronic properties of CNT networks and individual CNT devices has been investigated both experimentally and theoretically [127-134]. The observed changes of the electronic properties are in general attributed to effects of charge transfer and doping in the CNTs. But careful explanations of the experimental results and the theoretical conclusions should take into account the effects of water vapor and the gases such as oxygen that are present in ambient atmosphere. So to investigate this point further we conducted our experiments in partial pressures of several analytes such as acetone and water.

Figures 9-8 and 9-9 show the effect of acetone on the capacitance (measured at 20 kHz) and resistance (measured at DC) respectively of the CNT network as a function of gate voltage. It is not immediately clear from Figures 9-8 and 9-9 that the resistance and capacitance changes are related in any way. However, we may look at the predictions of the RC transmission line model. From the effective capacitance, $C_{Eff.} = \sqrt{\frac{2c}{\omega r}}$, if we look at the effect of small changes of resistance, we can derive the relation between the change in the capacitance and the change in the resistance as $\frac{\Delta C}{C} = -\frac{1}{2}\frac{\Delta R}{R}$.

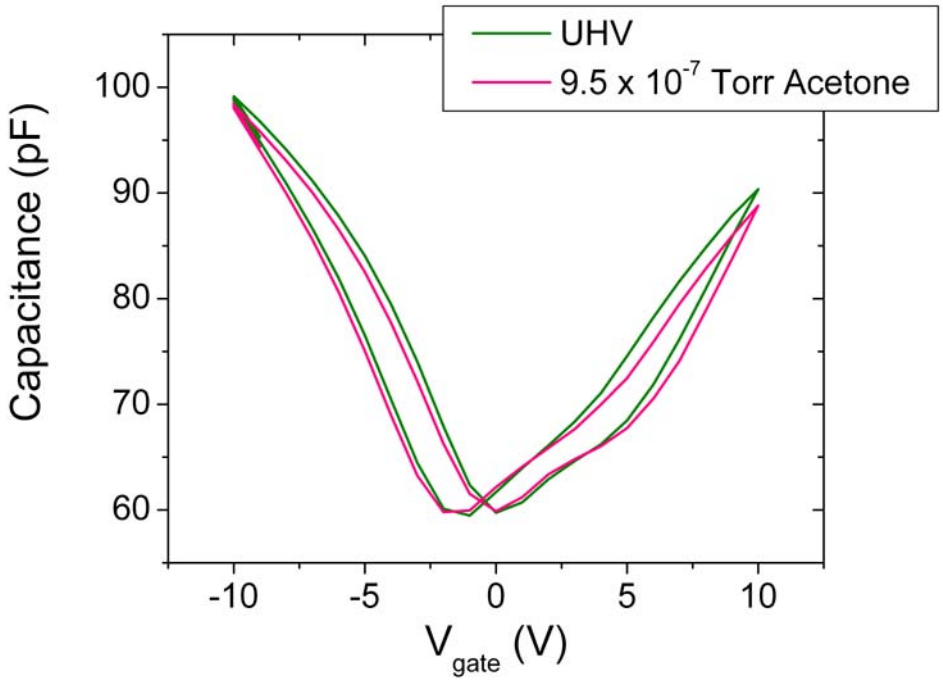

Figure 9-8. Capacitance of the CNT network in UHV and 9.5 10 $^{-7}$ Torr acetone pressure.

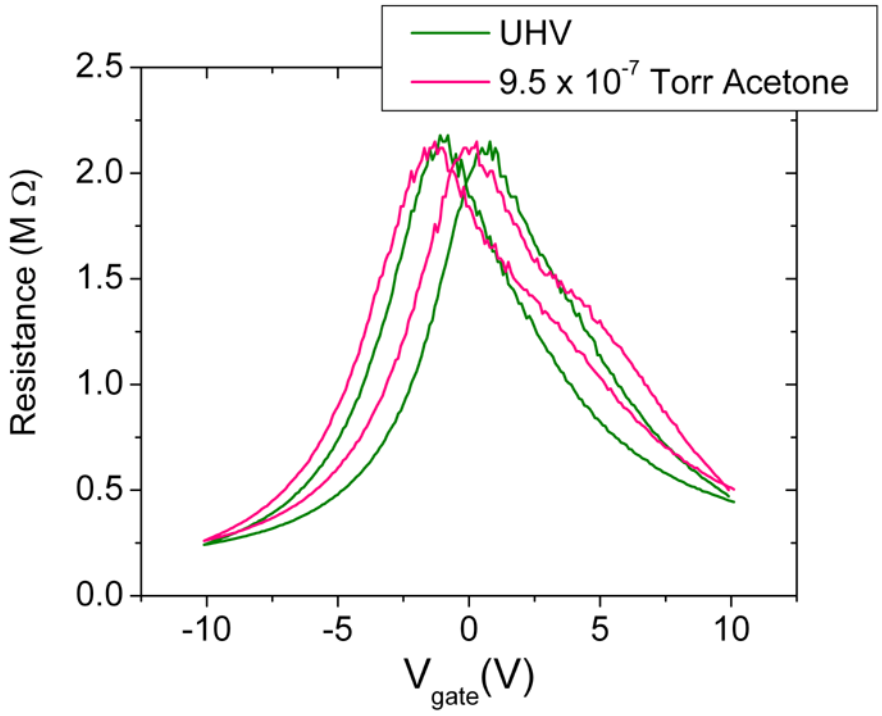

Figure 9-9. Resistance of the CNT network in UHV and 9.5 x 10 $^{-7}$ Torr acetone pressure.

In figure 9-10 we plot $\frac{\Delta C}{C}$ and $-\frac{1}{2}\frac{\Delta R}{R}$ (where we define the capacitance change as $\Delta C = C_{Analyte} - C_{UHV}$ and the resistance change as $\Delta R = R_{Analyte} - R_{UHV}$) due to acetone introduction in the chamber as a function of gate voltage. The vertical axis in the figure shows the changes of both capacitance and resistance. Note that the resistance is measured at DC, and therefore is a true probe of the film resistivity, and is not altered by the RC transmission line impedance. The resistance of the CNT network upon acetone introduction is presumably changing because of increased scattering due to physically adsorbed molecules on the CNT surface, or possibly through modification of the CNT-CNT junction resistance. From figure 9-10 we

conclude that the effect of acetone on the capacitance change of the CNT network is mainly through changing the resistivity of the film.

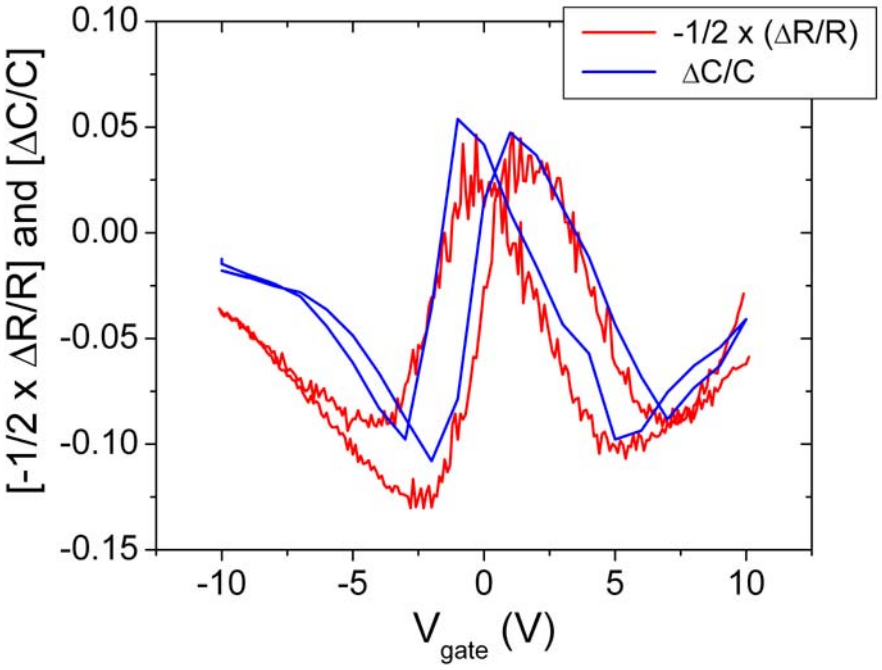

Figure 9-10. Change in the capacitance and resistance due to 9.5 x 10^{-7} Torr acetone pressure. Capacitance data is taken at 20 KHz using 0.1 V drive voltage.

Figures 9-11 and 9-12 show the effect of 2.8 x 10^{-8} Torr of water on capacitance and on resistance. Similar to the case of acetone, in figure 9-13 I plot $\frac{\Delta C}{C}$ and $-\frac{1}{2}\frac{\Delta R}{R}$ due to water introduction in the chamber as a function of gate voltage. The figure indicates that the capacitance and resistance changes are related to

each other and the capacitance change due to water introduction into the chamber is induced by the resistance change of the CNT network.

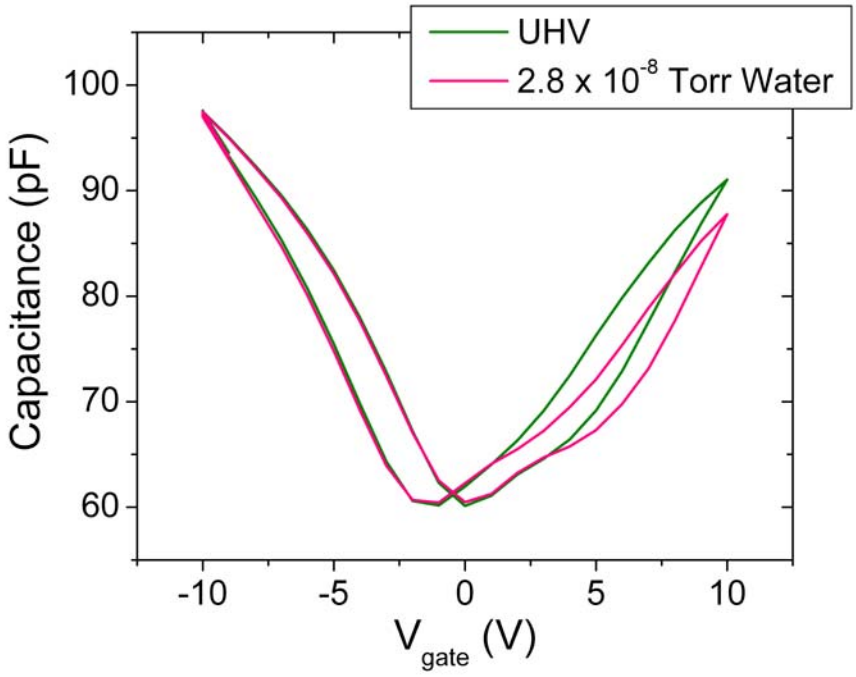

Figure 9-11. Capacitance of CNT network in UHV and 2.8 x 10^{-8} Torr water pressure.

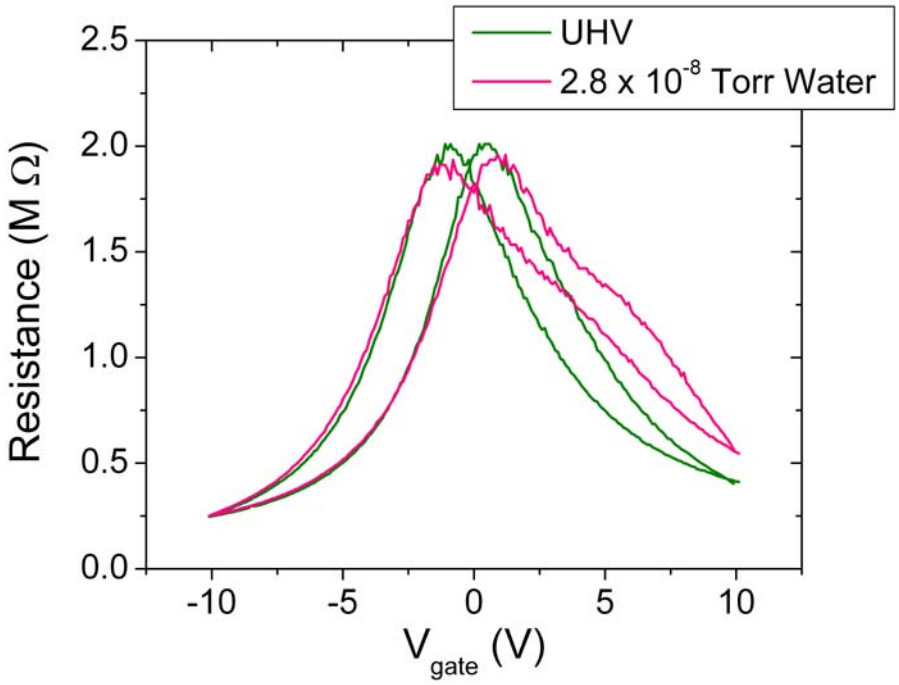

Figure 9-12. Resistance of CNT network in UHV and 2.8 x 10^{-8} Torr water pressure.

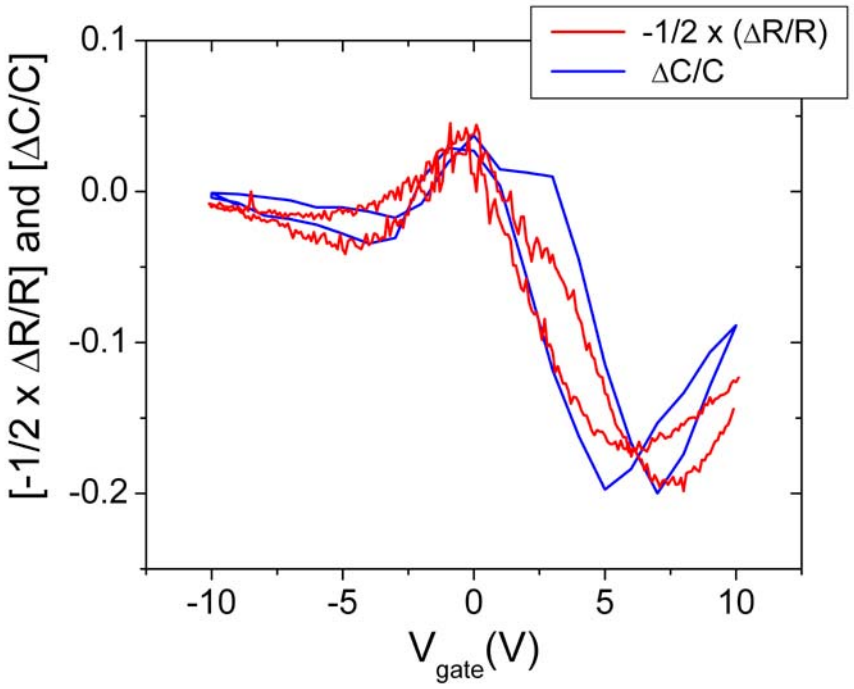

Figure 9-13. Change in the capacitance and resistance due to 2.8 x 10^{-8} Torr water pressure as a function of gate voltage.

Figures 9-14 and 9-15 below shows the result of the control experiments I performed with argon. Argon, being a nonpolar and noble gas, is not expected to have any effect on either the scattering or the polarization, therefore one expects to see no change in capacitance or resistance upon argon introduction to the chamber.

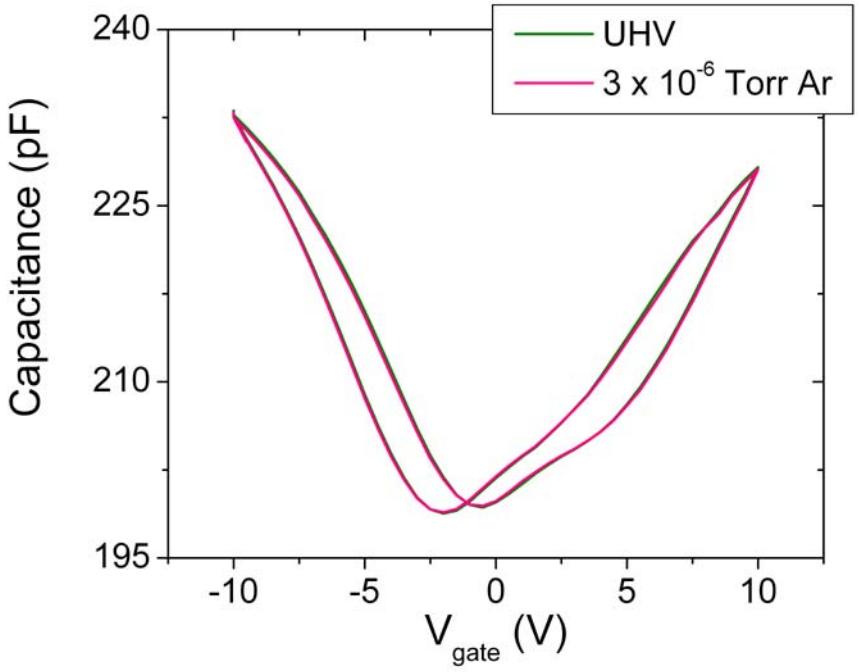

Figure 9-14. Capacitance of CNT network as a function of gate voltage in UHV and 3 x 10^{-6} Torr argon pressure. The capacitance data is taken at 20 KHz and by using 0.1 RMS amplitude of drive voltage.

I indeed observed no change in the capacitance of the CNT network in the presence of 3 x 10^{-6} Torr of argon pressure. By comparing figure 9-14 with figure 9-8 and figure 9-11, I conclude that the effects of acetone and water are not simply due to pressure alone, or to other gases that are introduced through the leak valve. The effects of acetone and water are also reproducible upon cycling; i.e. the different signatures of ΔC and ΔR vs. V_{gate} for acetone and water are reproducible (at least for this device) showing that the device is able to discriminate between acetone and water at pressures < 10^{-6} torr. Figure 9-15 shows the resistance as a function of gate voltage

in UHV and in 3 x 10^{-6} Torr argon pressure. Similar to the capacitance I observed no change in the resistance of CNT network in the presence of argon.

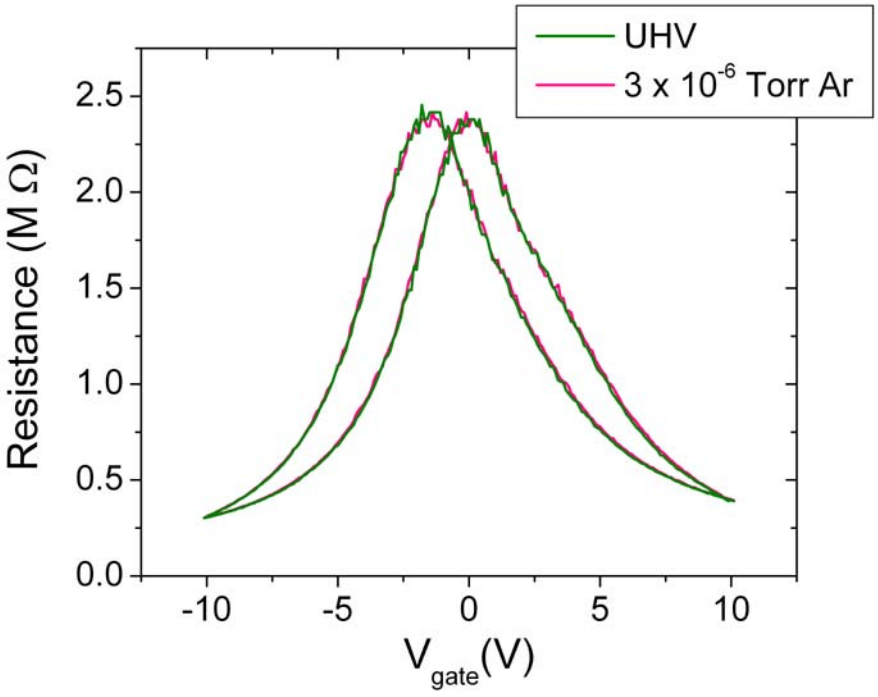

Figure 9-15. Resistance as a function of gate voltage in UHV and 3 x 10^{-6} Torr argon pressure.

9.4: Conclusion

In conclusion I have fabricated CNT network devices and measured the effect of several analytes on capacitance and conductance. I modeled my device as an RC transmission line and derived an effective capacitance for the device. I showed that the measured capacitance is frequency-dependent due to the decay of the applied AC signal in the CNT network. I also showed that the capacitance and the square root of conductance are proportional as predicted by the RC transmission line model. My results show that the resistance changes of the network is capable of producing a change in the capacitive part of the impedance at finite frequency, and that the measured capacitance change due to chemical analyte is due to this effect. My results also indicate that the resistance of the CNT networks is enormously sensitive to small partial pressure ($< 10^{-6}$ Torr) of analytes, and the gate voltage dependence of the response may be used to discriminate between analytes.

My results indicate the importance of the RC transmission line impedance in understanding chemicapacitive effects in highly resistive semiconducting films. A previous report[134] of chemicapacitive and chemiresistive effects in CNT films at ambient pressure also found that resistance and capacitance changes were proportional, though the constant of proportionality sometimes differed from -1/2. The authors of reference [134] did not take into account RC transmission line effects, though for the values of r and c which may be extracted from the paper, their devices are in the regime where $l_0 << L$ for their measurement frequency of 30 kHz, and hence the RC transmission line model is important.

Bibliography

1. Bardeen, J. and W.H. Brattain, *The Transistor, A Semi-Conductor Triode.* Physical Review, 1948. **74**(2): p. 230.
2. *International Technology Roadmap For Semiconductors, Lithography*. 2005.
3. Aviram, A. and M.A. Ratner, *Molecular rectifiers.* Chemical Physics Letters, 1974. **29**(2): p. 277-283.
4. Black, J.R., *Electromigration failure modes in aluminum metallization for semiconductor devices.* Proceedings of the IEEE, 1969. **57**(9): p. 1587-1594.
5. Park, H., A.K.L. Lim, A.P. Alivisatos, J. Park, and P.L. McEuen, *Fabrication of metallic electrodes with nanometer separation by electromigration.* Applied Physics Letters, 1999. **75**(2): p. 301-303.
6. Park, H., J. Park, A.K.L. Lim, E.H. Anderson, A.P. Alivisatos, and P.L. McEuen, *Nanomechanical oscillations in a single-C-60 transistor.* Nature, 2000. **407**(6800): p. 57-60.
7. Liang, W., M.P. Shores, M. Bockrath, J.R. Long, and H. Park, *Kondo resonance in a single-molecule transistor.* Nature, 2002. **417**(6890): p. 725-729.
8. Fiks, V.B., *Mechanism of ion mobility in metals.* Fizika Tverdogo Tela (Sankt-Peterburg), 1959. **1**: p. 16-30.
9. Huntington, H.B. and A.R. Grone, *Current-induced marker motion in gold wires.* Journal of Physics and Chemistry of Solids, 1961. **20**(1-2): p. 76-87.

10. Bosvieux, C. and J. Friedel, *Sur l'electrolyse des alliages metalliques.* Journal of Physics and Chemistry of Solids, 1962. **23**(1-2): p. 123-136.

11. Sorbello, R.S., *A pseudopotential based theory of the driving forces for electromigration in metals.* Journal of the Physics and Chemistry of Solids, 1973. **34**(6): p. 937-950.

12. Huntington, T.C.G.a.H.B., *Transport in nearly-free-electron metals. IV. Electromigration in zinc.* Phys. Rev. B, 1977. **16**: p. 1344–1352.

13. Liang Lou, W.L.S., and James C. Swihart, *Calculations of the driving force of electromigration in hcp metals: Zn, Cd, Mg.* Phys. Rev. B, 1986. **33**: p. 2170–2178.

14. Gupta, R., *Theory of electromigration in noble and transition metals.* Physical review, 1982. **25**(8): p. 5188.

15. Raju P. Gupta, Y.S., G. Brebec, and Y. Adda, Phys. Rev. B, 1983. **27**(2): p. 672–677.

16. Lodder, A., *Electromigration in Transition-Metal Hydrides: a Finite-Cluster-Model Study.* Journal de physique. I, 1984. **14**(12): p. 2955.

17. van Ek, J. and A. Lodder, *AB INITIO calculation of the electromigration wind valence of interstitial hydrogen in f.c.c metals.* Solid State Communications, 1990. **73**(5): p. 373-377.

18. Das, A.K. and R. Peierls, *The force on a moving charge in an electron gas.* Journal of Physics C: Solid State Physics, 1973. **6**(18): p. 2811.

19. Schaich, W.L., Phys. Rev. B, 1979. **19**: p. 630.

20. Sorbello, R.S., *Theory of the direct force in electromigration.* Phys. Rev. B, 1985. **31**(2): p. 798–804.

21. Landauer, R., *Spatial Variation of Currents and Fields Due to Localized Scatterers in Metallic Conduction.* IBM J. Res. Dev., 1957. **1**(3): p. 223.

22. Landauer, R., *Driving force in electromigration.* Physical review, 1974. **10**(4): p. 1266.

23. Landauer, R., *Spatial carrier density modulation effects in metallic conductivity.* Phys. Rev. B, 1976. **14**(4): p. 1474–1479.

24. Das, A.K. and R. Peierls, *The force of electromigration.* Journal of Physics C: Solid State Physics, 1975. **8**(20): p. 3348.

25. Landauer, R., *Geometry and boundary conditions in the Das-Peierls electromigration theorem.* Phys. Rev. B, 1977. **16**(10): p. 4698–4702.

26. Nowick, G.E.M.a.A.S., ed. *Diffusion in Crystalline Solids*. 1984, Academic Press: New York.

27. D. Young, A.C., *Failure Mechanism Models for Electromigration.* IEEE Transactions on Reliability, 1994. **43**(2): p. 186-192.

28. Shatzkes, M. and J.R. Lloyd, *A model for conductor failure considering diffusion concurrently with electromigration resulting in a current exponent of 2.* Journal of Applied Physics, 1986. **59**(11): p. 3890-3893.

29. Lloyd, J.R. in *Mater. Res. Soc. Symp. Proc.* 1991.

30. Blech, I.A. and E. Kinsbron, *Electromigration in Thin Gold-Films on Molybdenum Surfaces.* Thin Solid Films, 1975. **25**(2): p. 327-334.

31. Blech, I.A., *Electromigration in thin aluminum films on titanium nitride.* Journal of Applied Physics, 1976. **47**(4): p. 1203-1208.

32. Blech, I.A. and K.L. Tai, *Measurement of stress gradients generated by electromigration.* Applied Physics Letters, 1977. **30**(8): p. 387-389.

33. Saraswat, K.C. *Stanford University, EE 331 Lecture Notes,* *www.stanford.edu/class/ee311/NOTES/Interconnect_Al.pdf*.

34. Sharvin, Y.V., *A Possible Method For Studying Fermi Surfaces.* Sov. Phys. JEPT, 1965(21): p. 655-656.

35. David K. Ferry, S.M.G., *Transport in Nanostructures*. 1 ed. Cambridge Studies in Semiconductor Physics and Microelectronics Engineering, ed. M.P. Haroon Ahmed , Alec Broers. Vol. 6. 1997, Melbourne: Cambridge University Press.

36. van Wees, B.J., H. van Houten, C.W.J. Beenakker, J.G. Williamson, L.P. Kouwenhoven, D. van der Marel, and C.T. Foxon, *Quantized conductance of point contacts in a two-dimensional electron gas.* Physical Review Letters, 1988. **60**(9): p. 848.

37. Wharam, D.A., T.J. Thornton, R. Newbury, M. Pepper, H. Ahmed, J.E.F. Frost, D.G. Hasko, D.C. Peacock, D.A. Ritchie, and G.A.C. Jones, *One-dimensional transport and the quantisation of the ballistic resistance.* Journal of Physics C: Solid State Physics, 1988. **21**(8): p. L209-L214.

38. Yanson, I.K., *Nonlinear effects in the electric conductivity of point junctions and electron-phonon interaction in metals.* Zh. Eksp. Teor. Fiz., 1974(66): p. 1035–1050.

39. A.G.M. Jansen, A.P.v.G., P. Wyder, *Point contact spectroscopy in metals.* J. Phys. C. , 1980(13): p. 6073–6118.

40. Binning, G., H. Rohrer, C. Gerber, and E. Weibel, *Surface Studies by Scanning Tunneling Microscopy.* Physical Review Letters, 1982. **49**(1): p. 57.

41. Agrait, N., A.L. Yeyati, and J.M. van Ruitenbeek, *Quantum properties of atomic-sized conductors.* Physics Reports, 2003. **377**(2-3): p. 81-279.

42. Ohnishi, H., Y. Kondo, and K. Takayanagi, *Quantized conductance through individual rows of suspended gold atoms.* Nature, 1998. **395**(6704): p. 780-783.

43. Moreland, J. and J.W. Ekin, *Electron tunneling experiments using Nb-Sn ``break'' junctions.* Journal of Applied Physics, 1985. **58**(10): p. 3888-3895.

44. Costa-Kramer, J.L., *Conductance quantization at room temperature in magnetic and nonmagnetic metallic nanowires.* Physical Review B, 1997. **55**(8): p. R4875.

45. Joachim, C., J.K. Gimzewski, R.R. Schlittler, and C. Chavy, *Electronic Transparence of a Single C_{60} Molecule.* Physical Review Letters, 1995. **74**(11): p. 2102.

46. Stipe, B.C., M.A. Rezaei, and W. Ho, *Single-Molecule Vibrational Spectroscopy and Microscopy.* Science, 1998. **280**(5370): p. 1732-1735.

47. Moresco, F., G. Meyer, K.-H. Rieder, H. Tang, A. Gourdon, and C. Joachim, *Conformational Changes of Single Molecules Induced by Scanning Tunneling Microscopy Manipulation: A Route to Molecular Switching.* Physical Review Letters, 2001. **86**(4): p. 672.

48. Xu, B. and N.J. Tao, *Measurement of Single-Molecule Resistance by Repeated Formation of Molecular Junctions.* Science, 2003. **301**(5637): p. 1221-1223.

49. Gaudioso, J., L.J. Lauhon, and W. Ho, *Vibrationally Mediated Negative Differential Resistance in a Single Molecule.* Physical Review Letters, 2000. **85**(9): p. 1918.

50. Reichert, J., R. Ochs, D. Beckmann, H.B. Weber, M. Mayor, and H.v. LÃhneysen, *Driving Current through Single Organic Molecules.* Physical Review Letters, 2002. **88**(17): p. 176804.

51. Reichert, J., H.B. Weber, M. Mayor, and H. v. Lohneysen, *Low-temperature conductance measurements on single molecules.* Applied Physics Letters, 2003. **82**(23): p. 4137-4139.

52. Champagne, A.R., A.N. Pasupathy, and D.C. Ralph, *Mechanically Adjustable and Electrically Gated Single-Molecule Transistors.* Nano Lett., 2005. **5**(2): p. 305-308.

53. Lambert, M.F., M.F. Goffman, J.P. Bourgoin, and P. Hesto, *Fabrication and characterization of sub-3 nm gaps for single-cluster and single-molecule experiments.* Nanotechnology, 2003. **14**(7): p. 772.

54. Strachan, D.R., D.E. Smith, D.E. Johnston, T.-H. Park, M.J. Therien, D.A. Bonnell, and A.T. Johnson, *Controlled fabrication of nanogaps in ambient environment for molecular electronics.* Applied Physics Letters, 2005. **86**(4): p. 043109.

55. Houck, A.A., J. Labaziewicz, E.K. Chan, J.A. Folk, and I.L. Chuang, *Kondo effect in electromigrated gold break junctions.* Nano Letters, 2005. **5**(9): p. 1685-1688.

56. M.G. Burzo, P.L.K., P.E. Raad. *Thermal Transport Properties of Gold-Covered Thin-Film Silicon Dioxide*. in *IEEE 2002 Inter Society Conference on Thermal Phenomena*. 2002.

57. F. P. Incorpera, D.P.D., *Introduction to Heat Transfer*. 4 ed. 2002, New York: Wiley.

58. Lu, L., W. Yi, and D.L. Zhang, *3 omega method for specific heat and thermal conductivity measurements.* Review of Scientific Instruments, 2001. **72**(7): p. 2996-3003.

59. Scheer, E., W. Belzig, Y. Naveh, M.H. Devoret, D. Esteve, and C. Urbina, *Proximity Effect and Multiple Andreev Reflections in Gold Atomic Contacts.* Physical Review Letters, 2001. **86**(2): p. 284.

60. Yanson, A.I., G.R. Bollinger, H.E. van den Brom, N. Agrait, and J.M. van Ruitenbeek, *Formation and manipulation of a metallic wire of single gold atoms.* Nature, 1998. **395**(6704): p. 783-785.

61. Hansen, K. and M. Brandbyge, *Current-voltage relation for thin tunnel barriers: Parabolic barrier model.* Journal of Applied Physics, 2004. **95**(7): p. 3582-3586.

62. Sordan, R., K. Balasubramanian, M. Burghard, and K. Kern, *Coulomb blockade phenomena in electromigration break junctions.* Applied Physics Letters, 2005. **87**(1).

63. Meissner, H., *Superconductivity of Contacts with Interposed Barriers.* Physical Review, 1960. **117**(3): p. 672.

64. Onnes, H.K., Commun. Phys. Lab. Univ. Leiden, 1911(124c).

65. Meissner, R.O.a.W., Naturwissenschaften, 1933. **21**: p. 787.

66. Corak, W.S., B.B. Goodman, C.B. Satterthwaite, and A. Wexler, *Exponential Temperature Dependence of the Electronic Specific Heat of Superconducting Vanadium.* Physical Review, 1954. **96**(5): p. 1442.

67. Corak, W.S., B.B. Goodman, C.B. Satterthwaite, and A. Wexler, *Atomic Heats of Normal and Superconducting Vanadium.* Physical Review, 1956. **102**(3): p. 656.

68. Glover, R.E. and M. Tinkham, *Transmission of Superconducting Films at Millimeter-Microwave and Far Infrared Frequencies.* Physical Review, 1956. **104**(3): p. 844.

69. Glover, R.E. and M. Tinkham, *Conductivity of Superconducting Films for Photon Energies between 0.3 and 40kT_{c}.* Physical Review, 1957. **108**(2): p. 243.

70. Giaever, I., *Energy Gap in Superconductors Measured by Electron Tunneling.* Physical Review Letters, 1960. **5**(4): p. 147.

71. Bardeen, J., L.N. Cooper, and J.R. Schrieffer, *Theory of Superconductivity.* Physical Review, 1957. **108**(5): p. 1175.

72. Landau, V.L.G.a.L.D., Zh. Eksp Teor. Fiz., 1950. **20** p. 1064.

73. Waldram, J.R., *Superconductivity of Metals and Cuprates*. 1996, Bristol and Philadelphia: Institute of Physics Publishing.

74. Josephson, B.D., Phys. Lett., 1962(1): p. 251.

75. Likharev, K.K., *Superconducting weak links.* Reviews of Modern Physics, 1979. **51**(1): p. 101.

76. Gennes, P.G., *Superconductivity of Metals and Alloys*, ed. W.A. Benjamin. 1966, New York.

77. Andreev, A.F., *The thermal conductivity of the intermediate state in superconductors.* Sov. Phys. JEPT, 1964(19): p. 1228-1231.

78. Blonder, G.E., M. Tinkham, and T.M. Klapwijk, *Transition from metallic to tunneling regimes in superconducting microconstrictions: Excess current, charge imbalance, and supercurrent conversion.* Physical Review B, 1982. **25**(7): p. 4515.

79. Beenakker, C.W.J. *Three Universal Mesoscopic Josephson Effects*. in *Proceedings of the 14th Taniguchi International Symposium on Transport Phenomena in Mesoscopic Systems*. 1992. Berlin: Springer.

80. I.O.Kulik, *Macroscopic quantization and the proximity effect in S-N-S junctions.* Sov. Phys. JEPT 1970(30): p. 944-950.

81. A. Furusaki, M.T., *A unified theory of clean Josephson Junctions.* Physica B, 1990(165 & 166): p. 967-968.

82. MartÃ-n-Rodero, A., F.J. GarcÃ-a-Vidal, and A. Levy Yeyati, *Microscopic theory of Josephson mesoscopic constrictions.* Physical Review Letters, 1994. **72**(4): p. 554.

83. Averin, D. and A. Bardas, *ac Josephson Effect in a Single Quantum Channel.* Physical Review Letters, 1995. **75**(9): p. 1831.

84. Cuevas, J.C., A. MartÃ-n-Rodero, and A.L. Yeyati, *Hamiltonian approach to the transport properties of superconducting quantum point contacts.* Physical Review B, 1996. **54**(10): p. 7366.

85. Flensberg, K. and J.B. Hansen, *Subharmonic energy-gap structure and heating effects in superconducting niobium point contacts.* Physical Review B, 1989. **40**(13): p. 8693.

86. Kleinsasser, A.W., R.E. Miller, W.H. Mallison, and G.B. Arnold, *Observation of multiple Andreev reflections in superconducting tunnel junctions.* Physical Review Letters, 1994. **72**(11): p. 1738.

87. Bratus, E.N., V.S. Shumeiko, and G. Wendin, *Theory of Subharmonic Gap Structure in Superconducting Mesoscopic Tunnel Contacts.* Physical Review Letters, 1995. **74**(11): p. 2110.

88. Kondo, J., Prog. Theor. Phys., 1964. **32**: p. 37-49.

89. Weast, R.C., *Handbook of Chemistry and Physics*. 1976, Cleveland: CRC.

90. Lewis, F.A., *The Palladium Hydrogen System*. 1967, New York: Academic Press.

91. Wolf, R.J., M.W. Lee, R.C. Davis, P.J. Fay, and J.R. Ray, *Pressure-composition isotherms for palladium hydride.* Physical Review B, 1993. **48**(17): p. 12415.

92. Oates, T.B.F.a.W.A., Annu. Rev. Mater. Sci., 1991(21): p. 269

93. Favier, F., E.C. Walter, M.P. Zach, T. Benter, and R.M. Penner, *Hydrogen Sensors and Switches from Electrodeposited Palladium Mesowire Arrays.* Science, 2001. **293**(5538): p. 2227-2231.

94. Xu, T., M.P. Zach, Z.L. Xiao, D. Rosenmann, U. Welp, W.K. Kwok, and G.W. Crabtree, *Self-assembled monolayer-enhanced hydrogen sensing with ultrathin palladium films.* Applied Physics Letters, 2005. **86**(20): p. 203104-3.

95. Dankert, O. and A. Pundt, *Hydrogen-induced percolation in discontinuous films.* Applied Physics Letters, 2002. **81**(9): p. 1618-1620.

96. Fan, W. and J.E. Morris, *The effects of hydrogen absorption on the electrical conduction in discontinuous palladium films.* Thin Solid Films, 1994. **246**(1-2): p. 17-23.

97. James E, M., *Effects of hydrogen absorption on the electrical conduction of discontinuous palladium thin films.* International Journal of Electronics, 1996. **81**(4): p. 441-447.

98. U. Laudahn, S.F., H.U. Krebs, A. Pundt, M. Bicker, U.v. Hulsen, U. Geyer, T. Wagner, R. Kirchheim, J. Alloys Compound, 1999. **293**(490).

99. Laudahn, U., S. Fahler, H.U. Krebs, A. Pundt, M. Bicker, U. v. Hulsen, U. Geyer, and R. Kirchheim, *Determination of elastic constants in thin films using hydrogen loading.* Applied Physics Letters, 1999. **74**(5): p. 647-649.

100. Stillesjo, F., B. Hjorvarsson, and H. Zabel, *Hydrogen-induced lattice expansion in a (001)-oriented Mo/V superlattice.* Physical Review B, 1996. **54**(5): p. 3079.

101. Reisfeld, G., N.M. Jisrawi, M.W. Ruckman, and M. Strongin, *Hydrogen absorption by thin Pd/Nb films deposited on glass.* Physical Review B, 1996. **53**(8): p. 4974.

102. Yang, Q.M., G. Schmitz, S. FÃ¤hler, H.U. Krebs, and R. Kirchheim, *Hydrogen in Pd/Nb multilayers.* Physical Review B, 1996. **54**(13): p. 9131.

103. Iijima, S., *Helical microtubules of graphitic carbon.* Nature, 1991. **354**(6348): p. 56-58.

104. P. L. McEuen, M.S.F., and H. K. Park., *Single-walled carbon nanotube electronics.* IEEE Transactions on Nanotechnology, 2002. **1**: p. 78-85.

105. Dekker, C., *Carbon nanotubes as molecular quantum wires.* Physics Today 1999. **52**: p. 22-28.

106. Hamada, N., S.-i. Sawada, and A. Oshiyama, *New one-dimensional conductors: Graphitic microtubules.* Physical Review Letters, 1992. **68**(10): p. 1579.

107. Kane, C.L. and M.P.A. Fisher, *Transport in a one-channel Luttinger liquid.* Physical Review Letters, 1992. **68**(8): p. 1220.

108. Mintmire, J.W., B.I. Dunlap, and C.T. White, *Are fullerene tubules metallic?* Physical Review Letters, 1992. **68**(5): p. 631.

109. Wilder, J.W.G., L.C. Venema, A.G. Rinzler, R.E. Smalley, and C. Dekker, *Electronic structure of atomically resolved carbon nanotubes.* Nature, 1998. **391**(6662): p. 59-62.

110. Tans, S.J., A.R.M. Verschueren, and C. Dekker, *Room-temperature transistor based on a single carbon nanotube.* Nature, 1998. **393**(6680): p. 49-52.

111. Martel, R., T. Schmidt, H.R. Shea, T. Hertel, and P. Avouris, *Single- and multi-wall carbon nanotube field-effect transistors.* Applied Physics Letters, 1998. **73**(17): p. 2447-2449.

112. Mintmire, J.W. and C.T. White, *Universal Density of States for Carbon Nanotubes.* Physical Review Letters, 1998. **81**(12): p. 2506.

113. Durkop, T., S.A. Getty, E. Cobas, and M.S. Fuhrer, *Extraordinary Mobility in Semiconducting Carbon Nanotubes.* Nano Letters, 2004. **4**(1): p. 35-39.

114. Treacy, M.M.J., T.W. Ebbesen, and J.M. Gibson, *Exceptionally high Young's modulus observed for individual carbon nanotubes.* Nature, 1996. **381**(6584): p. 678-680.

115. Wong, E.W., P.E. Sheehan, and C.M. Lieber, *Nanobeam Mechanics: Elasticity, Strength, and Toughness of Nanorods and Nanotubes.* Science, 1997. **277**(5334): p. 1971-1975.

116. Kong, J., N.R. Franklin, C. Zhou, M.G. Chapline, S. Peng, K. Cho, and H. Dai, *Nanotube Molecular Wires as Chemical Sensors.* Science, 2000. **287**(5453): p. 622-625.

117. Collins, P.G., K. Bradley, M. Ishigami, and A. Zettl, *Extreme Oxygen Sensitivity of Electronic Properties of Carbon Nanotubes.* Science, 2000. **287**(5459): p. 1801-1804.

118. Chopra, S., K. McGuire, N. Gothard, A.M. Rao, and A. Pham, *Selective gas detection using a carbon nanotube sensor.* Applied Physics Letters, 2003. **83**(11): p. 2280-2282.

119. Bockrath, M., D.H. Cobden, J. Lu, A.G. Rinzler, R.E. Smalley, L. Balents, and P.L. McEuen, *Luttinger-liquid behaviour in carbon nanotubes.* Nature, 1999. **397**(6720): p. 598-601.

120. Odom, T.W., J.-L. Huang, P. Kim, and C.M. Lieber, *Atomic structure and electronic properties of single-walled carbon nanotubes.* Nature, 1998. **391**(6662): p. 62-64.

121. Meitl, M.A., Y. Zhou, A. Gaur, S. Jeon, M.L. Usrey, M.S. Strano, and J.A. Rogers, *Solution Casting and Transfer Printing Single-Walled Carbon Nanotube Films.* Nano Letters, 2004. **4**(9): p. 1643-1647.

122. Hines, D.R., S. Mezhenny, M. Breban, E.D. Williams, V.W. Ballarotto, G. Esen, A. Southard, and M.S. Fuhrer, *Nanotransfer printing of organic and carbon nanotube thin-film transistors on plastic substrates.* Applied Physics Letters, 2005. **86**(16): p. 163101-3.

123. Snow, E.S., J.P. Novak, P.M. Campbell, and D. Park, *Random networks of carbon nanotubes as an electronic material.* Applied Physics Letters, 2003. **82**(13): p. 2145-2147.

124. Zhou, Y., A. Gaur, S.H. Hur, C. Kocabas, M.A. Meitl, M. Shim, and J.A. Rogers, *p-Channel, n-Channel Thin Film Transistors and p-n Diodes Based on Single Wall Carbon Nanotube Networks.* Nano Letters, 2004. **4**(10): p. 2031-2035.

125. Wu, Z., Z. Chen, X. Du, J.M. Logan, J. Sippel, M. Nikolou, K. Kamaras, J.R. Reynolds, D.B. Tanner, A.F. Hebard, and A.G. Rinzler, *Transparent, Conductive Carbon Nanotube Films.* Science, 2004. **305**(5688): p. 1273-1276.

126. Kumar, S., J.Y. Murthy, and M.A. Alam, *Percolating Conduction in Finite Nanotube Networks.* Physical Review Letters, 2005. **95**(6): p. 066802-4.

127. Sumanasekera, G.U., C.K.W. Adu, S. Fang, and P.C. Eklund, *Effects of Gas Adsorption and Collisions on Electrical Transport in Single-Walled Carbon Nanotubes.* Physical Review Letters, 2000. **85**(5): p. 1096.

128. Zahab, A., L. Spina, P. Poncharal, and C. MarliÃ¨re, *Water-vapor effect on the electrical conductivity of a single-walled carbon nanotube mat.* Physical Review B, 2000. **62**(15): p. 10000.

129. Valentini, L., I. Armentano, J.M. Kenny, C. Cantalini, L. Lozzi, and S. Santucci, *Sensors for sub-ppm NO[sub 2] gas detection based on carbon nanotube thin films.* Applied Physics Letters, 2003. **82**(6): p. 961-963.

130. Chang, H., J.D. Lee, S.M. Lee, and Y.H. Lee, *Adsorption of NH[sub 3] and NO[sub 2] molecules on carbon nanotubes.* Applied Physics Letters, 2001. **79**(23): p. 3863-3865.

131. Zhao, J., A. Buldum, J. Han, and J.P. Lu, *Gas molecule adsorption in carbon nanotubes and nanotube bundles.* Nanotechnology, 2002. **13**(2): p. 195-200.

132. Snow, E.S., F.K. Perkins, E.J. Houser, S.C. Badescu, and T.L. Reinecke, *Chemical Detection with a Single-Walled Carbon Nanotube Capacitor.* Science, 2005. **307**(5717): p. 1942-1945.

133. Robinson, J.A., E.S. Snow, S.C. Badescu, T.L. Reinecke, and F.K. Perkins, *Role of Defects in Single-Walled Carbon Nanotube Chemical Sensors.* Nano Letters, 2006. **6**(8): p. 1747-1751.

134. Snow, E.S. and F.K. Perkins, *Capacitance and Conductance of Single-Walled Carbon Nanotubes in the Presence of Chemical Vapors.* Nano Letters, 2005. **5**(12): p. 2414-2417.

135. Bradley, K., J.-C.P. Gabriel, M. Briman, A. Star, and G. Gruner, *Charge Transfer from Ammonia Physisorbed on Nanotubes.* Physical Review Letters, 2003. **91**(21): p. 218301-4.

136. Thess, A., R. Lee, P. Nikolaev, H. Dai, P. Petit, J. Robert, C. Xu, Y.H. Lee, S.G. Kim, A.G. Rinzler, D.T. Colbert, G.E. Scuseria, D. Tomanek, J.E. Fischer, and R.E. Smalley, *Crystalline Ropes of Metallic Carbon Nanotubes.* Science, 1996. **273**(5274): p. 483-487.

137. Bronikowski, M.J., P.A. Willis, D.T. Colbert, K.A. Smith, and R.E. Smalley. *Gas-phase production of carbon single-walled nanotubes from carbon monoxide via the HiPco process: A parametric study*. in *The 47th international symposium: Vacuum, thin films, surfaces/interfaces, and processing NAN06*. 2001. Boston, Massachusetts (USA): AVS.

138. Nikolaev, P., M.J. Bronikowski, R.K. Bradley, F. Rohmund, D.T. Colbert, K.A. Smith, and R.E. Smalley, *Gas-phase catalytic growth of single-walled carbon nanotubes from carbon monoxide.* Chemical Physics Letters, 1999. **313**(1-2): p. 91-97.

139. Kong, J., A.M. Cassell, and H. Dai, *Chemical vapor deposition of methane for single-walled carbon nanotubes.* Chemical Physics Letters, 1998. **292**(4-6): p. 567-574.

140. Kong, J., H.T. Soh, A.M. Cassell, C.F. Quate, and H. Dai, *Synthesis of individual single-walled carbon nanotubes on patterned silicon wafers.* Nature, 1998. **395**(6705): p. 878-881.

141. Hafner, J.H., C.L. Cheung, T.H. Oosterkamp, and C.M. Lieber, *High-Yield Assembly of Individual Single-Walled Carbon Nanotube Tips for Scanning Probe Microscopies.* Journal of Physical Chemistry B, 2001. **105**(4): p. 743-746.

142. Dai, H., A.G. Rinzler, P. Nikolaev, A. Thess, D.T. Colbert, and R.E. Smalley, *Single-wall nanotubes produced by metal-catalyzed disproportionation of carbon monoxide.* Chemical Physics Letters, 1996. **260**(3-4): p. 471-475.

143. Hafner, J.H., C.L. Cheung, and C.M. Lieber, *Growth of nanotubes for probe microscopy tips.* Nature, 1999. **398**(6730): p. 761-762.

144. Brintlinger, T., Y.-F. Chen, T. Durkop, E. Cobas, M.S. Fuhrer, J.D. Barry, and J. Melngailis, *Rapid imaging of nanotubes on insulating substrates.* Applied Physics Letters, 2002. **81**(13): p. 2454-2456.

145. Fuhrer, M.S., B.M. Kim, T. Durkop, and T. Brintlinger, *High-Mobility Nanotube Transistor Memory.* Nano Letters, 2002. **2**(7): p. 755-759.